# Biological Agent Sensing Integrated Circuit (BASIC): A New Complementary Metal-oxide-semiconductor (CMOS) Magnetic Biosensor System

Yi Zheng

Dissertation submitted to the faculty of the Virginia Polytechnic Institute and State University in partial fulfillment of the requirements for the degree of

Doctor of Philosophy
In
Computer Engineering

Joseph G. Tront
Dong S. Ha
Nammalwar Sriranganathan
Patrick Schaumont
Wayne A. Scales

May 5, 2014
Blacksburg, VA

Keywords: Biohazard, Antibody and antigen, Pathogen, Iron nanoparticle, CMOS, Integrated circuit, Conical-shaped inductor, Uniform magnetic field, Magnetic sensor, LC oscillator, Frequency counter, Prototype, Antenna effect

# Biological Agent Sensing Integrated Circuit (BASIC): A New Complementary Metal-oxide-semiconductor (CMOS) Magnetic Biosensor System

Yi Zheng


# Abstract

Fast and accurate diagnosis is always in demand by modern medical professionals and in the area of national defense. At present, limitations of testing speed, sample conditions, and levels of precision exist under current technologies, which are usually slow and involve testing the specimen under laboratory conditions. Typically, these methods also involve several biochemical processing steps and subsequent detection of low energy luminescence or electrical changes, all of which reduce the speed of the test as well as limit the precision. In order to solve these problems and improve the sensing performance, this project proposes an innovative CMOS magnetic biological sensor system for rapidly testing the presence of potential pathogens and bioterrorism agents (zoonotic microorganisms) both in specimens and especially in the environment. The sensor uses an electromagnetic detection mechanism to measure changes in the number of microorganisms--tagged by iron nanoparticles--that are placed on the surface of an integrated circuit (IC) chip. Measured magnetic effects are transformed into electronic signals that count the number and type of organisms present. This biosensor introduces a novel design of a conical-shaped inductor, which achieves ultra-accuracy of sensing biological pathogens. The whole system is integrated on a single chip based on the fabrication process of IBM 180 nm (CMOS_IBM_7RF), which makes the sensor small-sized, portable, high speed, and low cost. The results of designing, simulating, and fabricating the sensor are reported in this dissertation.

# Acknowledgments

First and foremost, I thank my dissertation advisor Dr. Joseph Tront for the incredible amount of assistance he has given me throughout my graduate course work and dissertation research. I also thank my committee members Dr. Dong Ha, Dr. Patrick Schaumont, Dr. Wayne Scales and Dr. Nammalwar Sriranganathan as they have provided needed input and guidance on this research. I would also like to thank Mr. Bob Lineberry for his great help on the prototyping project. In addition, I thank the entire Bradley Electrical and Computer Engineering faculty and staff for all the help they have given me throughout my graduate program. Finally, I would like to thank my friends and family for their continuous support in all aspects of life.

All photos by author.

# Table of Contents

# List of Figures

# List of Tables

# Chapter 1: Introduction, Previous Work and Motivation

## 1.1 Introduction

A biological sensor is an analytical device used to detect micro-objects, such as molecules and microorganisms. Because of the extremely small sizes**,** they are invisible to the human eye. This advanced detecting and monitoring method has diverse uses. In the recent past, biosensor technologies have been widely applied in areas such as clinical diagnosis, industrial control, food and drug analysis/development, environmental protection, biochips and national defense. Development of biotechnology in the 21st century will provide broad application possibilities for businesses.

A biosensor system generally combines a sensitive biological element with a electrochemical detector [1]. The specific element is a biologically derived material used to bind or recognize the target analyte under sensing; for example, tissues, organelles, cell receptors, enzymes, antibodies, antigens, and nucleic acids. The electrochemical detector transforms the variation caused by the interaction of the analyte and the biological element into an electric signal that can be recorded and analyzed. For a biosensor application to be valuable in research and commercial purposes, it must contain a precise identification of a target analyte, availability of a biological recognition element, and the ability to function under various situations or environmental conditions beyond the commonly used sensitive laboratory-based techniques.

The global biomedical electronics market is growing rapidly to promote human health, a major goal in enhancing the quality of life worldwide. Fast and accurate

pathogen analysis is always in demand by modern medical professionals, as well as in the area of national defense. However, limitations of testing speed, sample conditions, and lack of precision exist under current biosensor technologies. To overcome these challenges, this project focuses on the design of a new biological sensor system for rapid detection of the presence of potential pathogens and bioterrorism agents (zoonotic microorganisms) both in specimens and in the environment. The sensor uses an electromagnetic detection mechanism to measure changes in the number of microorganisms--tagged by iron nanoparticles--that are placed on the surface of an IC chip. Measured magnetic effects are transformed into electronic signals used to analyze the density of organisms present. A wide variety of organisms can be detected in the same integrated circuit by using pathogen specific antibodies. Current design specifications call for a chip that has the ability to detect pathogens (organisms) in both a liquid and/or gaseous state. The reusability of the detector is also a basic design goal. The whole system is integrated on a single chip, which makes the sensor small-sized, portable, high speed, and low cost. In order to improve the sensing accuracy, an innovative design of a conical-shaped inductor that achieves high-uniformity of the magnetic field magnitude in the sensing region is introduced. This novel design of the sensor head achieves ultra-accuracy; simulation results indicate a maximum error of 7%. This sensor is designed such that no chemical processing is required once the chip is deployed; it will be a stand-alone sensor that can be operational with no human intervention. This device has the potential for use in laboratory diagnostic applications, in arrays of sensors distributed throughout an urban or battlefield environment, or as a personal detector worn by individuals.

## 1.2 Previous Work

In current biotechnologies, many different types of biosensor applications are available. One example of a commercial biosensor is the blood glucose biosensor, which uses the enzyme glucose oxidase to break blood glucose down [2][3]. At first, glucose is oxidized and its Flavin Adenine Dinucleotide (FAD) is reduced to $FADH_2$ by accepting two

hydrogen atoms from two electrons. Then $FADH_2$, in turn, is oxidized by the electrode and returned to its initial quinone form of FAD. Thus, the current for oxidation is a measure of glucose concentration. Another example of a biosensor involves the detection of DNA hybridization. One design is based on the magnetic inductive property [4], and another one uses electric capacitive property [5]. Other successful methods include Polymerase Chain Reactions (PCR) used for detecting if a nucleic acid polymer (DNA/RNA) is present in a sample, using engineered specific primers to ascertain whether the organism in question is in the sample [6]. In addition, special fluorescent labeled monoclonal and monovalent antibodies acceptors (receptors) similar to DNA/RNA strands have been used to bind to microorganisms, which then allows for their detection by typically using photoluminescence. These and other earlier methods are usually slow and involve testing the specimen under laboratory conditions. Typically, these methods also involve several biochemical processing steps and subsequent detection of low energy luminescence or electrical changes, all of which reduce the speed of the test and limit the precision. Moreover, some biosensor devices, such as the electronic nose, apply sensor arrays and pattern recognition systems to detect molecules, where the pattern of response from the detectors is used to recognize odors and flavors [7][8]. Their sensing principle is similar to human olfaction, where receptor proteins that respond to specific odor molecules are used. The sensor head arrays containing various proteins react to volatile compounds in the target odor or flavor. Then the response pattern on the arrays is compared to similar patterns in data storage for recognition. The advantage of the electronic nose is the fast and portable detection of the target analyte without complex laboratory based processes. However, this device cannot measure the accurate density of the analyte, but it only reports its presence, which limits its use.

Within a variety of applications in different fields, current biosensors used to detect pathogenic microorganisms are attracting more and more interest because of the increasing demand for timely and accurate diagnosis. For example, the phenomenon of surface plasmon resonance (SPR) techniques is used in many optical biosensors to detect micro-compounds and microorganisms [9][10][11]. The design involves a thin

layer of metal (typically gold) on a high refractive index glass surface under the stimulation of the laser light that causes a resonance of the plasmons on the metal surface to absorb the light energy. This light absorbance strongly depends on the angle and the wavelength of the incident light, as well as the surface property. Hence, implementation of SPR sensors introduces the target analyte to the metal surface. The change in the surface property yields a variation of the SPR angle that can be detected. Similarly, another optical mechanism, Surface-Enhanced Raman Scattering (SERS), is utilized in the detection of bacteria [12][13]. Raman scattering of light is enhanced by the presence of the analyte on a rough metal surface, which acts as a difference in the wavelength of the scattering light. The advantage of this technology over SPR is that it achieves greater sensitivity since the enhancement factor can be large. However, in SERS technology, preparation of the substrate is critical and reproducibility of the spectral measurement requires good laboratory skills. In addition, excitation of the mechanism requires a powerful and costly laser source; consequently, the capability of portable use is limited. Another typical optical biosensor, Laser-Induced Fluorescence (LIF), shoots an excitation laser across the analyte species [14]. The excited species will de-excite and emit light at a wavelength longer than the excitation wavelength. This fluorescent light is recorded with a photomultiplier tube or filtered photodiodes for 2D/3D imaging. The visualized analysis can be used in the detection and measurements of the analyte. Another type of bacteria biosensor is based on microcantilever technology [15][16]. The concept is that the surface of the cantilever beam is the platform of the target bacteria. With the pressure from the analyte, a deflection occurs at the free end of the beam and can be detected by a laser beam. An alternative sensing method uses a microactuator to drive the cantilever into a resonance, and the change of its resonance frequency caused by the analyte is measured. The drawback of this system is that the pressure distributed by each molecule depends on its position on the one end structure. Hence, non-uniformity of the analyte concentration on the surface will reduce sensing accuracy. These biosensors are detecting bacteria by their own characteristics. Nevertheless, some technologies induce the sensed changes from markers tagged to the targets other than the analytes themselves. A

common application is the Enzyme-Linked Immunosorbent Assay (ELISA) [17]. In this application, a secondary specific antibody is added to the target analyte after the specific analyte is binded to the antibody attached to the platform surface. This antibody is conjugated with enzyme that catalyzes the dye, which causes a color change in the liquid. A spectrophotometer is used to measure the amount of color change (a function of the amount of enzyme present) and, hence, quantifies the analyte concentration. As an advanced application of ELISA, magnetic biosensors apply magnetic mechanisms in the detection of microorganisms by replacing the enzyme with a magnetic bead as the marker [18]. With the improved development of magnetic sensor technology, these sensors have high sensitivity and low noise. However, they share the same disadvantage with ELISA. The post processes after depositing the analyte, including adding the markers and washing afterwards, require additional professional instruments, which increases cost and time of point-of-care and field diagnostics. To mitigate this shortcoming, Wang [19] has presented a magnetic biosensing scheme based upon on-chip LC resonance for fast point-of-care molecular level detection, which is similar to the system in this project. Unfortunately, error rate is up to 25% even with large-sized magnetic beads, and especially while detecting a low density of the targeted organism. Hence, the common shortcoming of magnetic sensors is that sensing accuracy is usually limited by the nonlinear factor of the magnetic field. This drawback is the main challenge for the present research.

## 1.3 Motivation

The health of a nation's citizenry, along with that of the military personnel who protect the public, is always of top concern in maintaining a sound national defense. Biological hazards (biohazards), organisms and their related bi-products, present a health hazard to humans, and they can be encountered anywhere in the environment. The two most common categories of biohazards are bacteria and viruses, which are both microorganisms. They can easily enter the body through inhalation and absorption when humans are exposed to them and may result in a catastrophic disease. Because the

microorganisms are invisible to humans, generally odorless, and easily and rapidly dispersed, these biohazards have become one of the greatest threats to human health.

Some biohazards arise from natural disasters, such as SARS and the flu viruses of past years. In a short time, they spread throughout the world and cause thousands of deaths. Even worse, biohazards are particularly pernicious when they purposely are introduced into the surroundings as a tactic of terrorism or biological warfare. Much evidence reveals that a huge number of casualties occurred from the use of biological weapons in World War II. A bomb carrying biological toxins or infectious agents could infect people in a range as large as an entire town quickly. Due to the amount of area affected and the severity of the exposure, bio-weapons are defined as weapons of mass destruction (WMD) and are prohibited by the mandate of the Biological Weapons Convention (BWC) that was signed by most countries after WWII. In addition to massive use of bio-weapons in warfare, terrorism has become another form of spreading biohazards when terrorists carry and release pathogenic agents in public. This type of attack with biohazards is difficult to predict, detect and prevent, especially when the target is civilians in high concentration areas. Bio-terror attacks in the past several decades have revealed a lack of timely alarm in many national security systems.

Out of the hope of developing a system capable of a timely response to the presence of biohazards, the researcher is motivated to develop a biosensor project capable of being used for fast and accurate pathogen detection and analysis in civilian medical situations as well as in national defense situations. Thus, prior deployment and prompt delivery of appropriate sensor devices to the scene are required. Modern CMOS technology provides a great opportunity for integrating entire biological sensor systems into a single IC chip, which has the advantages of being small-sized, portable, high speed, low power, and low cost [20][21]. Under the assumption of large number production runs, the commercial retail price of this stand-alone sensor could be less than $100. An alternative for further reducing the cost is integrating this biosensor system into a multi-functional system based on integrated circuits. Current electronic devices encompass as many functions as possible in one operational system. For example, battlefield

information collection gear on an individual soldier could collect GPS coordinates, vital sign information, temperature, directional acceleration, etc., as a single integrated entity. Moreover, multiple sensor units connecting to a central processor can build up a wireless sensing network that covers a large area for strategic planning. For national defense, this innovative biological sensor system might be distributed to military units and government agents in all countries for rapid reactions to any situations with potential biohazards. In civilian usage, this biosensor would have a large market in hospital and laboratory based biomedical equipment, as it significantly simplifies the patient assessment process and shortens the time of pathogen detection and analysis. In addition, it could be integrated into an in-home medical system that allows patients or healthy individuals to measure their daily condition at home as a provisional self-diagnosis [22].

## 1.4 Summary

This chapter contains a brief review of previous work on biological sensor systems and their limitations. With the motivation of countering harmful biohazards, a new CMOS magnetic biosensor system, named the Biological Agent Sensing Integrated Circuit (BASIC), is proposed that would improve the speed and accuracy in the detection of pathogenic microorganisms.

Chapter 2 of this dissertation is an overview of the proposed BASIC system, including the sensing concept and mechanism; Chapter 3 introduces the design details of the sensor head that consists of an on-chip conical-shaped inductor; Chapter 4 illustrates the simulations of the sensor head in the electromagnetic simulation software; Chapter 5 describes the design of the LC oscillator circuit that performs as a signal transformer; Chapter 6 introduces the signal processing circuits, frequency counter and timing controller; Chapter 7 presents the means for constructing the prototype system for the test bench of the BASIC system; the conclusion and future work are given in Chapter 8.

# Chapter 2: Overview of BASIC System

## 2.1 Introduction

This chapter discusses the overall processing flow of the biological agent sensing integrated circuit (BASIC) system and introduces it by steps. Its system sensing concept is based on the magnetic inductance change from iron nanoparticles inside of the microbes. The biological mechanism explains how this concept is implemented in the detection of target analytes.

## 2.2 System Architecture

The architecture of the BASIC system is explained below and its diagram is shown in Figure 2-1.

- Step 1: an on-chip inductor constitutes the sensor head, while the sample container, containing the specimen of biological agents, is located above it. The biologicals are tagged by iron nanoparticles and, hence, change the magnetic properties of the sample container. This set-up, in turn, changes the coil's electrical inductance and sets up the sensing capability.
- Step 2: the inductor is the core component of the LC oscillator circuit. The oscillator generates a voltage signal whose frequency is based on the coil's inductance. Consequently, the sensing change of the inductance caused by iron nanoparticles is transformed to a frequency shift.

• Step 3: the oscillating voltage signal from the LC oscillator is transmitted to the next stage by passing through a digital frequency counter whose output will be a 32-bit binary value.

• Step 4: in this final step, the counted frequency value of the current period is stored and analyzed in a data processor, i.e., a computer terminal. After collecting data from a certain number of periods, the accurate frequency shift is determined and the sensing result of the biological density is calculated.

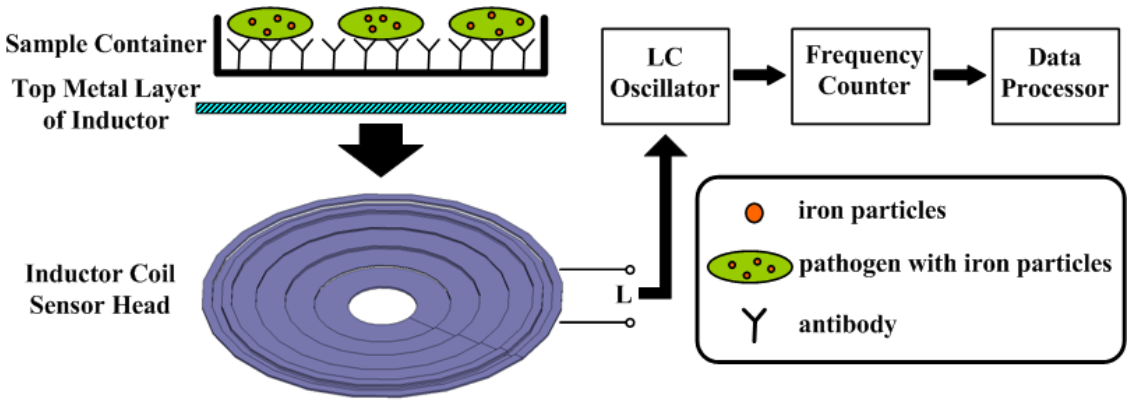


Figure 2-1: System diagram of the BASIC system

For the proposed sensor system, Steps 1-3 are integrated in a CMOS hardware processor, whereas the implementation of the final step is flexible. The data processor can be either integrated in the same CMOS chip or implemented in a separate processor; the decision depends on the tradeoff between the application requirement and development cost. Although a fully integrated system profits from saving space and power, its development cost and design complexity could be huge, especially since the last step is post-processing calculations after the data collection, which does not require real time logic. Therefore, in the prototype system, the data processor is suitable for being implemented in the software. In addition to the above circuits, an extra function block, called a timing controller, provides timing control signals for coordinating these logic steps in any processing periods. In the prototype system, a commercial function signal generator substitutes for this function block, which reduces the design complexity and

saves the budget. However, in future plans, this function shall be incorporated into the chip as a highly integrated product.

## 2.3 Inductive Sensing Concept

The basic system principle of this magnetic biosensor is the rapid detection of electrical changes occurring at the surface of an integrated circuit based on the presence or absence of biological agents that are embedded with iron nanoparticles [23]. As depicted in Figure 2-1, a chip is constructed with inductive coils in place, then the coil area (sample container) is selectively loaded with biological agents specifically set up to cause detectable changes from iron nanoparticles. A baseline measurement of the electrical characteristics is taken. A fluid sample containing pathogens tagged with iron nanoparticles is then introduced into the sample container. Pathogens bonded to antibodies change the magnetic properties of the sample container and, in turn, the coil's electrical inductance is sensed by the combined oscillator, the frequency counter, and the data processor. The sensing results are used for measuring the amount of change of inductance, calculating the number of pathogens bonded, and thus determining the number/density of wild pathogens in the sample environment.

The measurement of the coil's inductance change is based on an on-chip LC oscillator that shifts the oscillation frequency in direct relation to the number of iron particles introduced into the sample container. According to the below expression (2-1), the relative frequency-shift is proportional to the total amount of inductance change [19].

$$f_0 = \frac{1}{2\pi\sqrt{L_0 C_0}} \qquad f = f_0 - \Delta f \approx f_0\left(1 - \frac{\Delta L}{2L_0}\right) \qquad \frac{\Delta f}{\Delta L} \approx \frac{f_0}{2L_0} \tag{2-1}$$

where $L_0$ is the self-inductance of the coil, and $\Delta L$ denotes the total inductance change with the introduction of iron nanoparticles. Assuming a current $I$ generates magnetic field $H$ by passing through the coil, placing a single iron particle in the coil changes the field to $H'$ corresponding to the iron volume $Vp$. Hence, $\Delta L$ can be modeled by analyzing the magnetic energy as follows,

$$\Delta L = \frac{2\Delta E}{I^2} = \frac{1}{I^2}\iiint_{Vp}(\vec{H'}\cdot\vec{B'} - \vec{H}\cdot\vec{B})d_V \approx \frac{1}{I^2}\iiint_{Vp}(\left\|\vec{H}\right\|^2 f^2(c,\mu_r)\mu_r\mu_0 - \left\|\vec{H}\right\|^2 \mu_0)d_V \tag{2-2}$$

$$\approx \frac{\mu_0}{I^2}\left\|\vec{H}\right\|^2 \iiint_{Vp}(f^2(c,\mu_r)\mu_r - 1)d_V \qquad \because \vec{H'} = \vec{H} + \vec{H_M} \approx \vec{H}f(c,\mu_r) \tag{2-3}$$

where $\mu_r$ is the relative permeability of the particle material, and $c$ is a coefficient to evaluate the field by the effect of magnetic materials [24]. Note that $H_M$ is the field change by the magnetization, which is proportional to the original field $H$, and hence $H'$ can be expressed as $H$ with the factor $f$. The variables $c$ and $\mu_r$ are related to $Vp$, while $H$ is independent. As the nanometer sized particle is tiny enough, the approximation of uniform vector field across its volume holds. Moreover, its field quantity square has a linear relationship with the inductance change since the coefficient $c$ is only determined from the shape of the particle. Therefore, as long as $||H||$ is location-independent in the sensing zone, as is $\Delta L$ for every single identical particle, then the total amount of inductance change will be proportional to the amount of particles in the case of the multiple particles presented. This analysis guides the design of the inductive coil to constitute uniform field magnitude in the sensing zone.

## 2.4 Sensing Mechanism Based on Biological Position Exchange

Most microorganisms like bacteria need iron for diverse functions, for instance, cell composition, intermediary metabolism, enzyme activity, and host cell interactions [25]. Generally, bacteria absorb iron in the form of $Fe_3O_4$. Consequently, $Fe_3O_4$ nanoparticles are used in this design as tags of target pathogens. Since much of the environment is deficient in iron, the average level of iron content in many species of microorganisms is about 0.01% dry weight, or 0.1 mg/gm [26]. It could be difficult to detect the presence of change in this small amount of iron. Hence, for better sensitivity, instead of directly sensing the iron in the wild pathogens, the pre-setup units in the sensor containing high iron content are used for a larger amount of change. After feeding sufficient iron to the microbes, the iron content level could reach 24 mg/gm, or over 2% dry weight of cells [26]. The difference from 0.01% to 2% compared to from 0% to 0.01% makes detection

easier. The pre-setup process of the sensor system entails growing pathogens in broth with high concentrations of iron nanoparticles. Then these pathogens are killed by chemicals to stop their living functions.

An antibody, or immunoglobulin, is a protein produced by B cells. The immune system uses antibodies to identify and neutralize foreign objects such as viruses and bacteria. Different foreign invaders have their unique substances, called antigens, that can be recognized by specific antibodies [27][28]. As depicted in Figure 2-1, each antibody is a Y-shaped molecule. Each tip of the "Y" of an antibody has a paratope specific for one particular epitope on an antigen, allowing both of them to bind together with precision, which allows one-to-one matching, such as a key and lock. This binding mechanism is illustrated in Figure 2-2. By utilizing this mechanism, the antibody with a specific paratope can capture the targeted biological pathogen for detection.

The on-chip sample container bottom is coated with corresponding epitope specific antibodies. They must be well bonded to the integrated surface and must remain in place to produce reliable processes. The sample container's silica-silanol surface can be charged for biological agent attachment with a variety of functional groups reacting silane coupling agents directly onto the surface. For example, aminopropyltrimethoxysilane can be reacted with silanol surface groups under either anhydrous condition in toluene at elevated temperatures or in the vapor phase or in water. This reaction yields a surface with primary amine reactive groups that are positioned for subsequent reaction with appropriate biological agents that are necessary for pathogen capture and detection. The surface amino groups can be quantified by reaction in anhydrous media with an excess of triflouroacetic anhydride; then the excess reagent can be hydrolyzed and removed, and the remaining trifluoroacetic acid can be titrated quantitatively with a standardized base. The reaction produces a very strong bond between the chip surface and the biological antibodies, which can be sustained throughout the typical environment being used and lifetime of the chip.

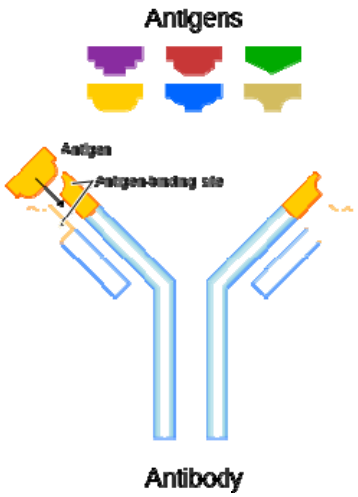


Figure 2-2: Matching antibody's paratope to antigen's epitope. [29] “Antibody”, *http://en.wikipedia.org/wiki/Antibody*, used under fair use, 2014.

When the sufficient amount of dead pathogens tagged with iron nanoparticles are placed into the sample container, the antibodies at the container bottom capture them and array them in the same flat (defined as a “sensing plane” in a later chapter). Then the rest of the unbound units are washed away. At this point, pre-setup is accomplished, and a measurement baseline is possible from the sensor output. In the detection process, the prepared sensor chip surface is exposed to the environment or the samples with the wild type target pathogens not tagged with iron nanoparticles (shown in Figure 2-3). The strength of the antibody-antigen connection depends on their paratope-epitope binding energy [30]. Consequently, the wild type pathogens in the environment with the same epitope as the dead ones have the same potential binding energy. This situation results in competition for the binding paratope-epitope between wild and dead pathogens with the fixed antibodies, and some displacements occur when the wild type ones are winners. Generally, the amount of dead pathogens losing space is proportional to the relative amount of wild type pathogens present. This principle is commonly used in Complement ELISA (CELISA) and is called competitive immunoassay [31]. Overall, when wild pathogens flow through the container bottom, they exchange binding positions with dead pathogens and cause a reduction in the total amount of iron in the container. During this

process, the time of exposure, the amount of exchanged pathogens, or the weight change of iron varies with the total amount of wild type pathogen present. Therefore, the sensor output based on the timeline enables evaluation of the density of the targeted pathogens.

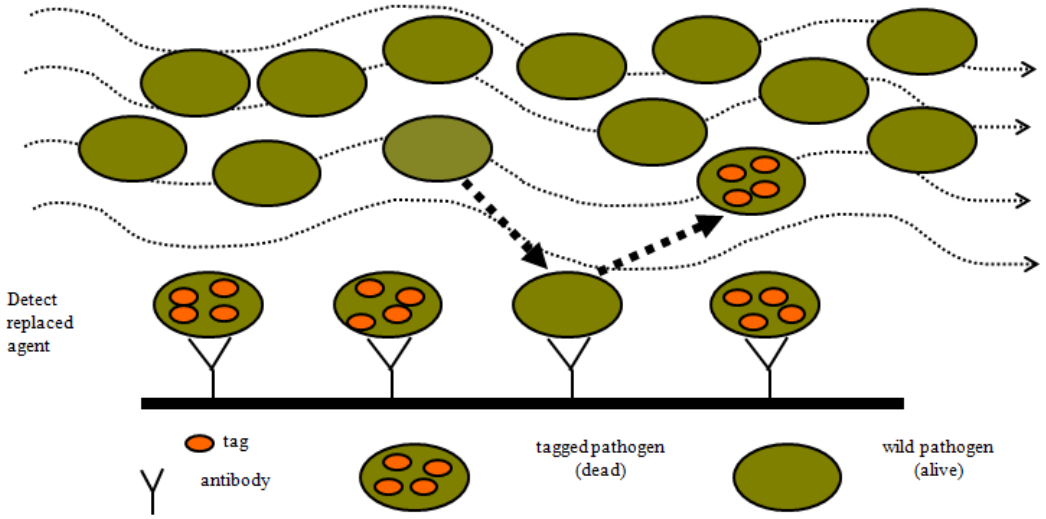


Figure 2-3: Pathogen exchanging mechanism.

## 2.5 Summary

This chapter gives an overview of the processing flow of the BASIC system. The whole system circuit consists of 5 components: the sensor head, the LC oscillator, the frequency counter, the timing controller, and the data processor. The design budget necessitated that the first three components be integrated into an IC chip for the prototype system. The sensing concept explains how to transform the variation caused by the analyte into the frequency shift of the electro-signal that can be recorded and analyzed. Moreover, the sensing mechanism, based on biological position exchange, describes the application of the pathogen exchanging phenomenon in the pre-setup process of the biosensor.

# Chapter 3: Sensor Head: The Conical-Shaped Inductor

## 3.1 Introduction

This chapter presents the design details of the sensor head to produce high sensing accuracy, which is the core challenge of this biosensor system. The key to the success of the senor head is designing an inductor with uniform field quantity in the sensing plane (previously discussed in Section 2.3).

## 3.2 Conventional On-chip Spiral Inductor

The typical spiral inductor widely used in ICs is square shaped with single or double metal layers. For design simplification, it applies constant trace width and spacing for wiring. However, this geometry generates non-uniform magnetic field strength on its surface. Figure 3-1 is a plot of the field magnitude $||H||$ in a plane just above the inductor. The magnitude increases exponentially from the center to the edge of the metal trace. The peak indicated by the warmest color appears near the four 90-degree-angle areas of the square coil. This field distribution is not efficient in this application since the relatively uniform field only occurs in the very small center area. Moreover, the H-field magnitude in the center is the weakest. Recalling the expressions (2-2) and (2-3), the inductance change is proportional to the square of the field magnitude; that is, the sensitivity to an iron nanoparticle located in the center is worse than in any other positions. Due to the

extremely low sensing efficiency, the conventional square shaped inductors cannot fit the design requirements of this project.

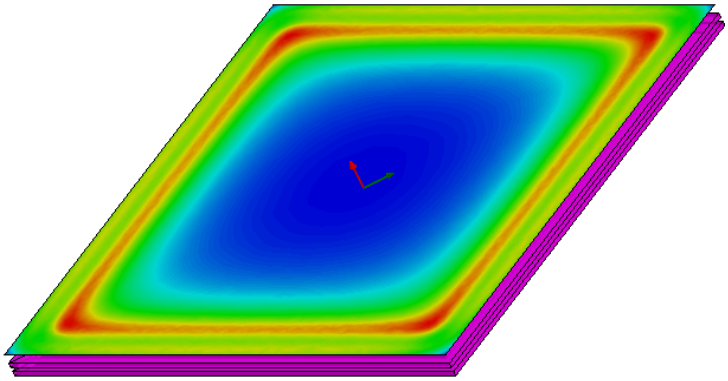

Figure 3-1: Field distribution of the conventional square inductor.

## 3.3 Proposed Conical-shaped Design

According to the Biot-Savart law in the equation below (3-1), the magnetic field intensity at arbitrary locations strongly depends on the combination of the current direction and the distance between the current and the location point.

$$B = \frac{\mu_0}{4\pi}\int_C \frac{Idl \times \vec{r}}{|r|^2} \tag{3-1}$$

where $r$ is the full displacement vector from the current to the location point, and the integral of $C$ means a closed curve. Some traditional designs, like Helmholtz coils [32] and spherical coils [33], generate uniform field at the center area by the symmetric structure in the vertical axis. However, due to the limitations of on-chip design technology, including layout geometry, the number of metal layers, and the layer thickness and spacing, these schemes are not feasible in the design of the integrated inductor. Wang [19] provides an option of a bowl-shaped, dual-layer stacked inductor with on-chip purpose. This design shows the proto-idea of arranging multi-leveled current distribution to balance the field intensity, though its uniformity is still not sufficient to meet the demand of high accuracy measurements. The following sub-

sections introduce details on the design issues of achieving uniform field quantity and propose a solution called the conical-shaped inductor.

### 3.3.1 Solutions to Improve Uniformity on Field Quantity

With the purpose of improving field quantity uniformity, design methodology in three dimensions ($r$, $\theta$, $z$) of the cylindrical coordinate system corresponding to the spiral inductor coil is introduced as follows.

In the dimension "$\theta$," the peak of the field magnitude depends on the geometric angle at a vertex, with the field intensity being reduced as the angle is changed towards 180 degrees. Therefore, applying a quasi-circular shaped coil will minimize the angle peaks. As the field plots in Figure 3-2 indicate, an octagon coil generates a nearly circular radial field in the center area, while the polygon with more sides further extends this achievement.

In the dimension "$z$" (out of the paper plane), the idea is to reduce the deviation range of the field magnitude from the center area to the coil's bound. Customizing the metal layer thickness and z-direction spacing are prohibited by the fabrication process, but the location of the sensing surface can be positioned appropriately. By increasing its altitude above the top trace layer, as shown in Figure 3-3, the field magnitude at minor peaks drops exponentially faster than at valleys due to the shorter distance to the conductor. This adjustment gains a relatively larger area of uniformity in the center. However, a long distance between the sensing platform and the inductor coil will decrease the field quantity significantly and, hence, adversely affect system sensitivity.

With the last dimension "$r$," the design considers how to compensate for the low field quantity in the center area. In conventional multi-layer inductors, the geometry of the coil turns in every metal layer is identical, causing the effect that, on any transverse plane, the center always stays farther away from the conductor than the boundary. Thus, the basic idea in the solution is moving the current closer to where the field strength is poor, or vise versa. This revision could be accomplished by applying coils with unequal diameters and trace widths. The effect of balancing current distribution by using a dual-

layer, four-turn inductor model is shown in Figure 3-4. Since the coil's longitudinal dimension is short compared to the transverse dimension, the internal turns are generally wider in order to spread out the current distribution. Deep valleys in plot (a) (Figure 3-4) caused by the vertical gaps between adjacent turns should be avoided. Plot (b) (Figure 3-4) presents more potential for uniformity from the version without such gaps. Note that a large width of conductor causes the field magnitude to drop from the inner to the outer edge. To eliminate this limitation, a larger number of coil turns involving more metal layers is required, which leads to the innovative design that is introduced next.

By incorporating the above analysis into the inductor design, whose cross-section is depicted at the bottom of Figure 3-5, the ten-turn structure uses five metal layers. The quasi-circular shaped coils with different diameters and trace widths are staggered between adjacent layers to avoid vertical gaps and overlapping. The vertical geometry parameters of the inductor are based on the fabrication process of IBM 180 nm (CMOS_IBM_7RF). The transverse distances of ring conductors are marked in Figure 3-5. The middle blue curve in the 2D plot of Figure 3-5 presents an ultra-uniform field strength area with a diameter of 50 um that is located 3 um above the top metal layer. The sensing plane is defined as the area inside the sensor container that passes through the region of highest field uniformity as described by the blue curve. The plot in Figure 3-6 illustrates that, in this sensing plane, the conical-shaped design generates the required uniform and relatively high intensity magnetic field. According to the equation (2-3), a 1.29% deviation of the magnetic field strength is expected to generate 2.6% maximum deviation of the inductance change by a single particle.

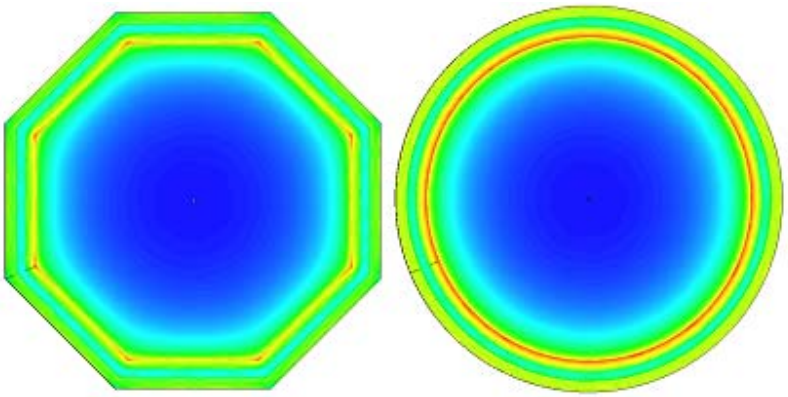

Figure 3-2: Field distributions of the octagon and circular inductors.

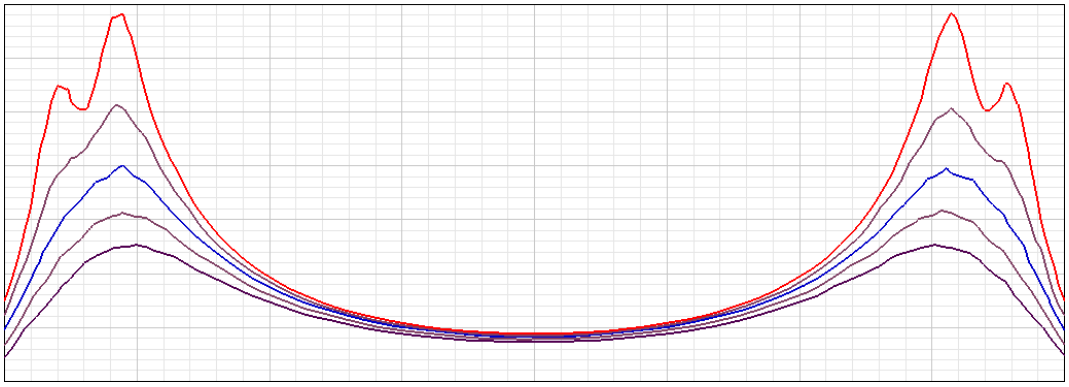

Figure 3-3: Field plots of different altitudes of the sensing surface.

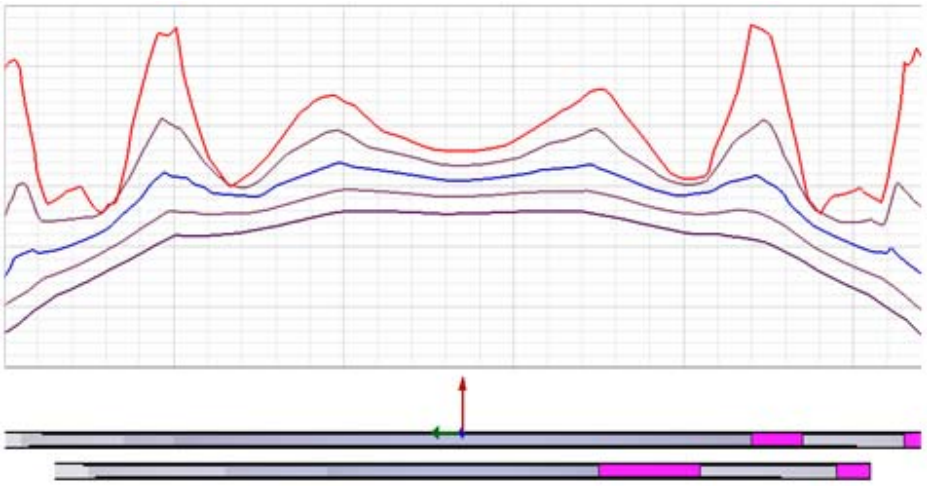

(a) With vertical gaps

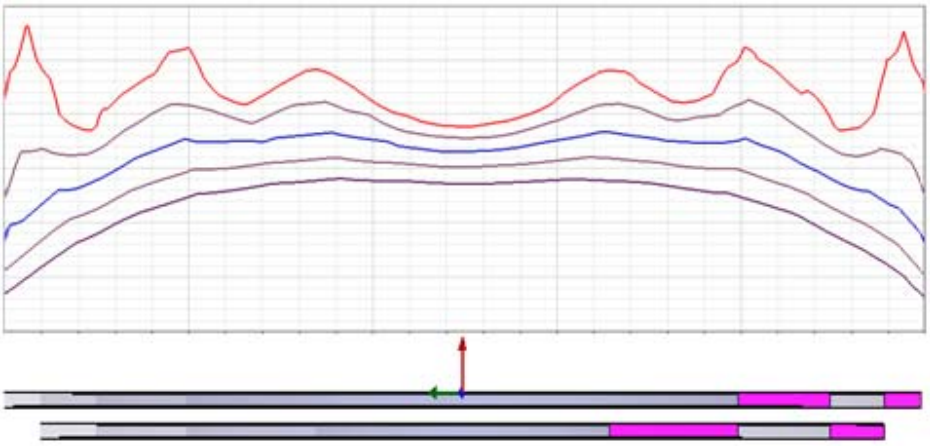

(b) Without vertical gaps

Figure 3-4: Field plots of the current distribution balanced model w/o vertical gaps.

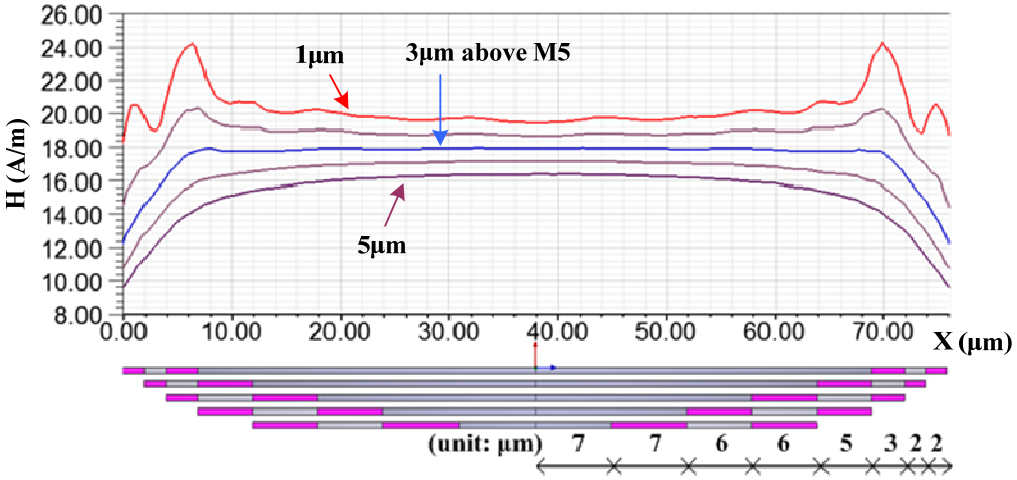


Figure 3-5: The conical-shaped coil and its geometry parameters.

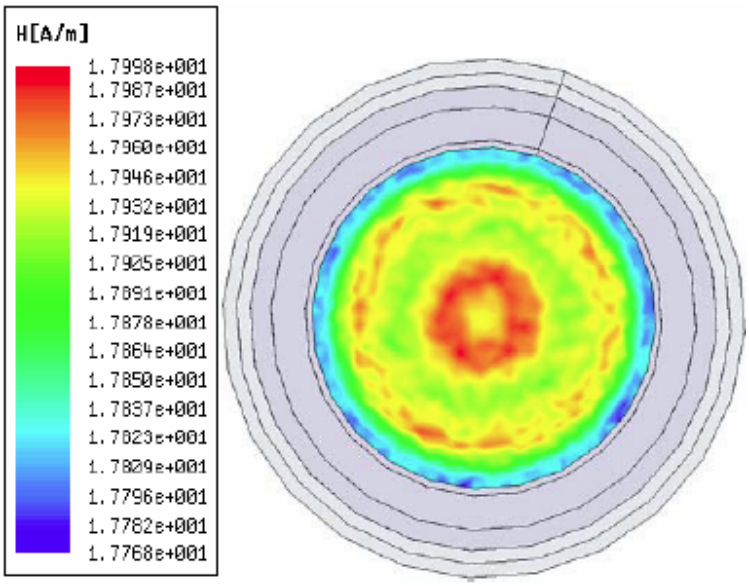


Figure 3-6: Field distribution of the conical-shaped coil.

### 3.3.2 Defect of the Preliminary Design

The sensor system uses an LC oscillator to transform measured magnetic effects into electronic signals. Proper oscillation of the LC tank requires a relatively high quality ($Q$) factor from the inductor design. The $Q$ factor of a physical inductor with a series loss resistance at the resonance is defined in the following expression.

$$Q_L = \frac{\omega_0 L}{R_L} \qquad \because \omega_0 = \sqrt{\frac{L - CR_L^2}{L^2 C}} \tag{3-2}$$

where $\omega_0$ is the resonant frequency of the LC tank in radians per second, and $R_L$ is the parasitic resistance of the inductor. The LC tank model is shown in the Figure 3-7. The previously designed conical-shaped inductor uses different diameters and metal trace widths on various wiring layers to balance the current density in its coils, while the outer turns are built with larger diameters and are narrower than the inner ones [34]. This geometry generates not just a self-inductance of 5.4 nH, but also a large loss resistance of 50 Ω that yields a very poor $Q$ factor of 0.68 at 1 GHz and fails to oscillate reliably when used in an LC oscillator built with the technology of IBM 180 nm (IBM_CMOS_7RF). According to the expression below (3-3), by assuming that the parasitic resistance in the

LC tank is the only noise source and it generates thermal noise, the noise power will be inversely proportional to the $Q$ factor. Hence, a low $Q$ factor reflects large phase noise to the oscillation.

$$P_n = \frac{\overline{v_n^2}}{R_L} = 4kT\Delta f = 4kT\frac{f_0}{Q_L} \qquad \because Q_L = \frac{f_0}{\Delta f} \tag{3-3}$$

where $k$ is Boltzmann's constant, $T$ is the absolute temperature of the resistance, and $\Delta f$ is the half-power bandwidth. The instability of the LC oscillator will definitely harm the sensing accuracy based on the frequency shift. Moreover, for a constant oscillation, compensating the great power loss from the parasitic resistance could become a problem in the design of the LC oscillator, since a low $Q$ factor essentially restricts the voltage gain of the compensating circuits. Further analysis of this situation is discussed in Chapter 5. Therefore, the focus on improving the inductor design centers on enhancing the $Q$ factor.

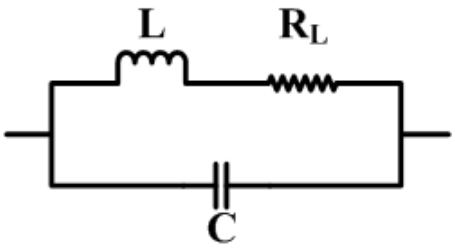


Figure 3-7: LC tank model

### 3.3.3 Improved Conical-shaped Design

The $Q$ factor of an inductor can be improved by either increasing the inductance $L$ or reducing the parasitic loss resistance $R_L$. In general, enhancing $L$ is achieved by applying more coil turns or enlarging the area enclosed by a turn. However, due to the incremental increase of the total metal trace length, $R_L$ also increases, which results in a negative effort. Another approach is to decrease $R_L$ and maintain $L$. Since the thicknesses of metal layers are fixed in IC technology, the resistance per length is inversely proportional to the metal width. Thus, keeping the wire length fixed and broadening its width can effectively

decrease $R_L$ and improve the $Q$ factor. In the previously proposed geometry, the outer turns contribute most to $R_L$, and their widths should be redesigned for the improved geometry. Meanwhile, the top metal layer of many IC processes is fabricated to be much thicker than other layers that can be used for the inductor's wiring, due to its lower sheet resistance. Skin effect and conductor-to-conductor proximity effects at high frequency increase $R_L$ of the wires, as well as the noise introduced by the capacitive coupling between adjacent coils. Because of this, the target for the LC oscillation frequency is below 1 GHz, which requires either relatively large $L$ or $C$. The previous expression (3-2) indicates that simply using a large capacitor harms the $Q$ factor. Conversely, adding extra coils with low resistance could complement $L$ without trading off the $Q$ factor. However, note that these extra coils are added outside of original design, and hence they distribute little magnetic field in the sensing region that is located in the center. This causes a loss of system sensitivity, which is defined as

$$Sensitivity = \frac{\Delta L_{single}}{L} \tag{3-4}$$

where $\Delta L_{single}$ is the average inductance change caused by a single iron nanoparticle in the sensing container. Therefore, the number and position of extra coils must be carefully considered.

After considering all these factors, the improved conical-shaped inductor is represented in Figure 3-8, along with the plot of its magnetic field magnitude at the frequency of 800 MHz. A 2% deviation of the field uniformity from the middle blue curve is observed in the sensing region located 2 μm above the second from the top metal layer. The diameter of the sensing area is 50 μm, based on the size of pathogens expected to be placed in the sample holder. Table 3-1 lists the dimensions for every coil layer. Simulation of this design, which includes 15 turns in the inductor, has a self-inductance as 11.9 nH and parasitic resistance as 24 Ω. This represents a significant improvement in the $Q$ factor, which is over 3 compared to the previous design.

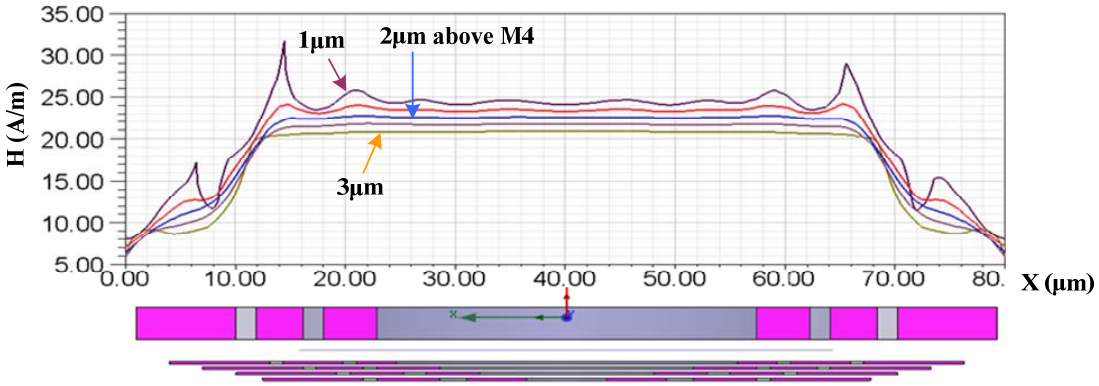


Figure 3-8: Field plots of the improved conical-shaped inductor.

| Layer | 1st inner coil | | 2nd inner coil | | 3rd inner coil | |
|---|---|---|---|---|---|---|
| | Inner edge radius (µm) | Width (µm) | Inner edge radius (µm) | Width (µm) | Inner edge radius (µm) | Width (µm) |
| Metal1 | 6 | 9 | 19 | 9.5 | 30.5 | 15 |
| Metal2 | 13 | 8 | 24.5 | 8 | 34.5 | 15 |
| Metal3 | 19 | 9.5 | 30.5 | 7 | 39.5 | 15 |
| Metal4 | 25.5 | 6 | 33.5 | 9 | 44.5 | 15 |
| Metal5 | 28.5 | 8 | 39.5 | 7 | 49.5 | 15 |

Table 3-1: Geometry of every inductor coil.

### 3.3.4 Design Consideration Regarding Oscillation Frequency

Improvement of the project design includes having the oscillation frequency under 1 GHz to avoid the increment of resistance and coupling effects. To overcome the drawback of skin effect, the on-chip IC technology uses very thin wires (thickness less than 1 µm) for conduction, which restrains the resistance increment at a high frequency. However, the top metal layer is generally much thicker than the other layers. Using the calculation shown in the expression below (3-5), the skin depth of an aluminum trace with 1 GHz is about 2.58 µm, which is close to half of the top metal layer thickness in the technology for this project. Therefore, resistance will start rising exponentially when the frequency goes higher.

$$\delta = \sqrt{\frac{2\rho}{\omega\mu}} \tag{3-5}$$

where $\rho$ is resistivity of the conductor, and $\mu$ is its absolute magnetic permeability.

Other factors must be considered in choosing proper oscillation frequency, such as eddy current reducing effective inductance in high frequency or the speed limitation of the digital circuit components due to propagation delay. However, the most significant reason for determining the frequency of below 1 GHz is sensing accuracy, which is the core design specification. The design discussion of the generated magnetic field should include the effect of the frequency. The current distribution in the traces varies with the frequency due to the skin effect and, hence, causes change to the magnetic field. Figure 3-9 represents 2D plots of the magnetic field magnitude with several frequency steps from DC to 5 GHz. With the frequency climbing, the field of the center area gradually increases, while the edges are falling. At a frequency above 1 GHz, the field deviation is extended and the field uniformity is violated, which obviously drops the sensing accuracy. Therefore, for the current geometry of the inductor design, the optimal operating frequency must not exceed 1 GHz. Note that it could be possible to adjust the coil geometry to obtain uniform field quantity in a specific frequency higher than 1 GHz. However, the tradeoffs from other factors need to be carefully considered.

In contrast, the oscillation frequency should not be set too low. First, assuming that the system is errorless, the highest possible sensitivity of the biosensor is determined by the number of the sampled cycles from the oscillation signal, since the smallest change that can be detected by the digital frequency counter is 1 cycle. Design details of the frequency counter are discussed in Chapter 6. If the frequency is very low, the sampling time must be longer than for a higher frequency in order to capture enough cycles for accurate counting. Hence, the sensing period is increased and becomes a tradeoff to the design. The second reason is that the oscillation frequency is proportional to the $Q$ factor. As discussed previously, a low $Q$ factor decreases system performance and raises design difficulty.

Considering the previously discussed factors and the results of related simulations, the oscillation frequency chosen in this system is 800 MHz. As an added observation, an exact frequency of the oscillation signal is not necessary. Any frequency around 800 MHz in an appropriate range is acceptable as the baseline; that is, as long as the measurement baseline is found, the frequency shift will be the valid sensing result in the data process.

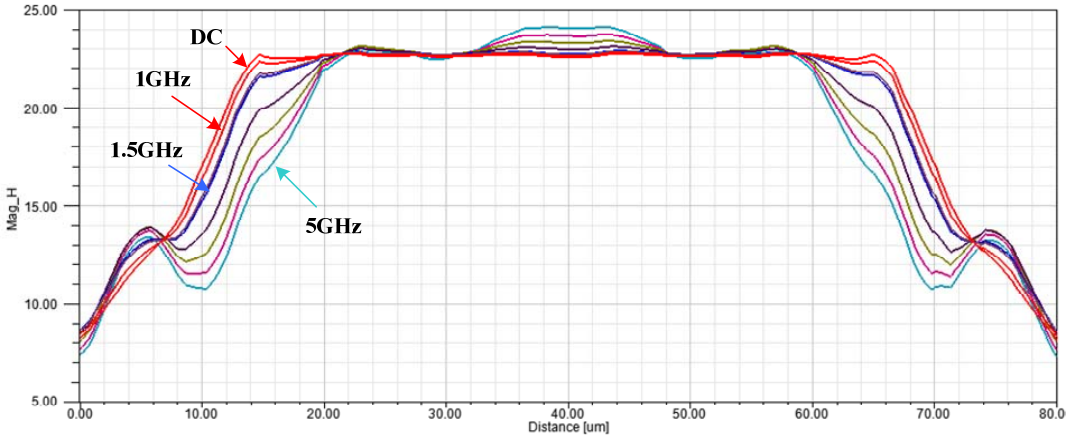


Figure 3-9: Field plots of the frequency steps from DC to 5 GHz.

## 3.4 Final Design of the Integrated One-piece Wiring Inductor

The inductor model discussed above relies on the assumption that every coil is a quasi-circular shaped closed loop. However, the actual integrated inductor is wired together as one continuous conductor by using jumper connections between different coils and layers. The gaps in the circular coils and the jumper connection wires result in breaking the symmetric structure and, hence, cause non-uniformity of the field distribution. In order to reduce the size of the non-uniformity affected area in the sensing plane, coil and layer jumper connections are confined together in a small volume. Figure 3-10 shows the field magnitude plot of the continuous-wired inductor operating at the 800 MHz frequency. The maximum field magnitude increase of 12.4% over the minimum field is shown in red and deep blue highlights. This deviation, depicted by warm colors, encompasses

approximately 15% of the sensing region. According to previous expressions (2-2) and (2-3), a single iron particle placed in the maximum field magnitude yields a maximum 26.4% difference in the inductance change compared to that of the particle placed in the minimum field magnitude. By comparison, a dynamic range of 6.5% in inductance change occurs when a particle is placed anywhere in the rest of the sensor area. Obviously, including this large variance in field distribution in the sensing area will reduce the sensing accuracy considerably. One proposed solution is excising this section from the sensing region, which is shown in Figure 3-11. Notice that the range of values in the legend for this figure is different than the range in Figure 3-10. This plot illustrates that the difference in the field magnitude without the spike section is only 3.1%, which yields no more than 7% deviation in the inductance change. In conclusion, the one-piece wiring conical-shaped inductor design generates the required uniform and relatively high intensity magnetic field.

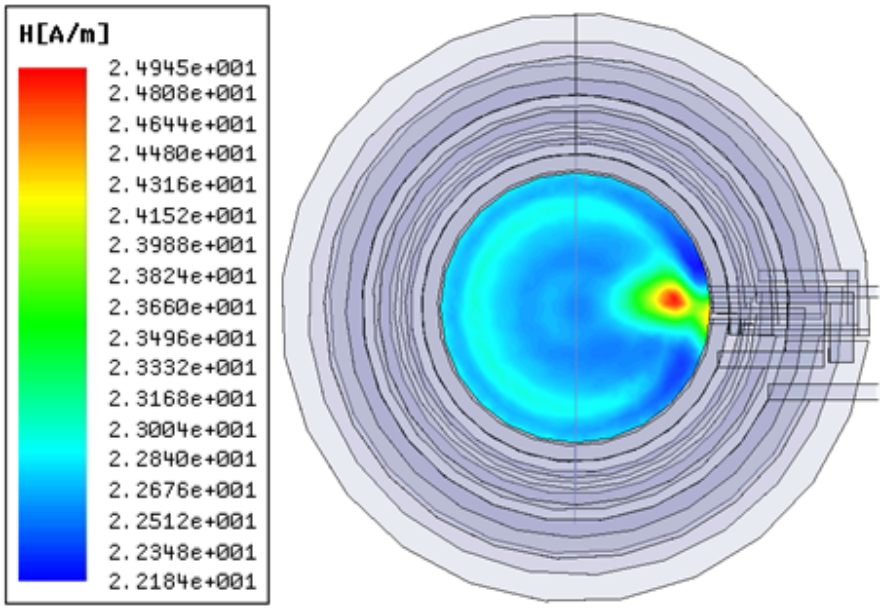


Figure 3-10: Field distribution of the one-piece wiring conical-shaped inductor.

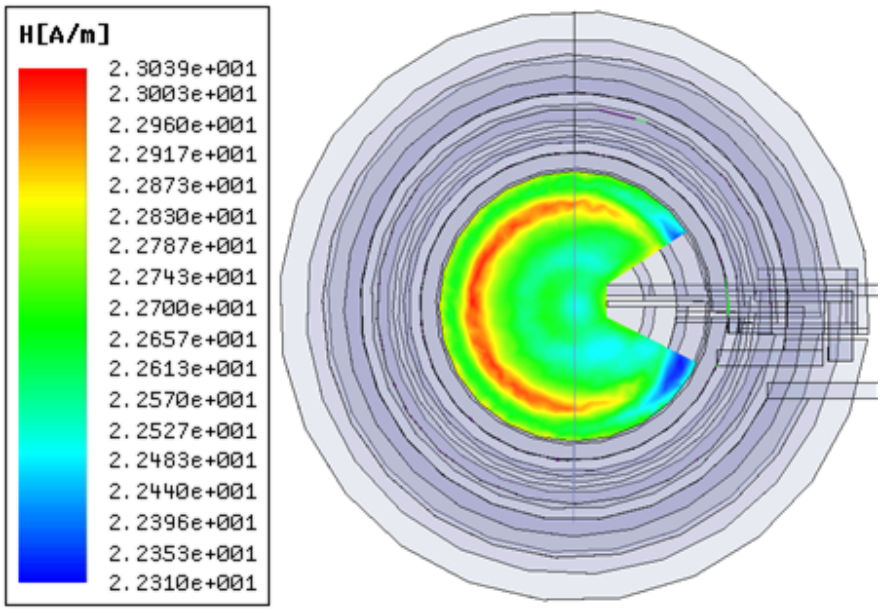


Figure 3-11: Field distribution after removal of the non-uniformity section.

## 3.5 Summary

This chapter introduced the detailed design process and considerations of the core component in this biological sensor system, the sensor head. An innovative design of a conical-shaped inductor, which uses multiple metal layers to balance current density in the coils, is proposed as the sensor head for achieving ultra-uniformity of the magnetic field quantity in the sensing region. The evaluated deviation of field magnitude is as small as 3.1%, which meets the requirement of high sensing accuracy.

# Chapter 4: Simulations of the Sensor Head

## 4.1 Introduction

This chapter presents simulations of the conical-shaped inductor for verifying the design concept of the biosensor system. The 3D model of the conical-shaped inductor was built using the magnetic simulation software of Ansoft Maxwell. Details of the setup of the simulations are presented to ensure ultra-high accuracy simulations. Note that the field plots in Chapter 3 are from the simulations of Ansoft Maxwell.

## 4.2 3D Model of the Simulation

Ansoft Maxwell is a premier electromagnetic field simulation software for engineers tasked with designing and analyzing 2D and 3D electromagnetic devices. For arbitrary controls of the inductor model, the 3D simulator is used. Figure 4-1 represents the 3D model of the 15 turns conical-shaped inductor. The geometry of the coil, such as widths and spacing of the traces, is based on Table 3-1. Other parameters, like metal thickness and layer spacing, are taken from the IBM_CMOS_7RF technology used for this project [35]. The material of the coil is aluminum. The sample container discussed in Chapter 3 is used here--its diameter is 50 μm, and its bottom, as the sensing plane, is located 2 μm above the second from the top metal layer. To model the tags in an organism, the simulation uses ball-shaped, high permeability $Fe_3O_4$ nanoparticles, $\mu_r$ is set to 10, with average diameters of 50 nm, which is based on the range of pathogens in this research.

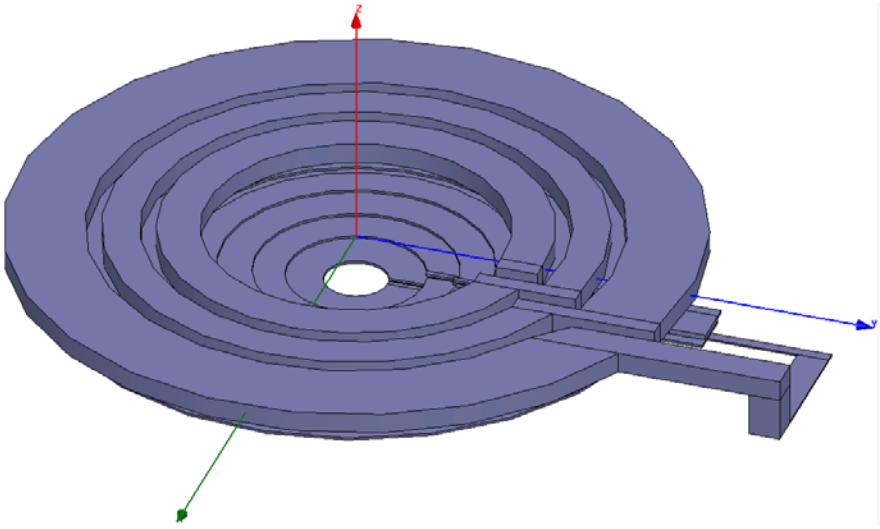

Figure 4-1: Ansoft Maxwell 3D model of the conical-shaped inductor.

## 4.3 Ansoft Maxwell Simulation Setup

The purpose of the simulations is to evaluate how much change the tags, or the iron nanoparticles, in the biological organisms cause to the sensor head. Due to the extremely tiny size of the particles compared to the size of sensing plane, the simulation environment of the electromagnetic field solver must be carefully set up for accurate results. For this reason, the mechanism of the field solver in Ansoft Maxwell must be clearly understood.

### 4.3.1 Finite Element Method (FEM) in Maxwell 3D

The term *finite element* refers to the method used to obtain numerical results from an arbitrary geometry [36]. The arbitrary, complicated geometry is broken down into simple pieces called *finite elements*. In Maxwell3D, the fundamental unit of the *finite element* is a tetrahedron (shown in Figure 4-2). When all the elements are considered together, it is known as the *finite element* mesh. For field approximation in an individual unit, 10 nodes, including 4 at the vertices and 6 at the midpoint of edges, are selected to assemble a 2nd order quadratic polynomial basis function (4-1).

$$Hx(x,y,z) = a_0 + a_1 x + a_2 y + a_3 z + a_4 xy + a_5 yz + a_6 xz + a_7 x^2 + a_8 y^2 + a_9 z^2 \qquad (4\text{-}1)$$

where $x$, $y$, $z$ are the coordinates and $a_0$~$a_9$ are the field value on 10 nodes. Once the mesh is defined, the desired field quantities for the total nodes are calculated in the simulation, which solves the Maxwell's equation (4-2):

$$\nabla \times \vec{H} = \vec{J} \qquad (4\text{-}2)$$

where $J$ is the current density.

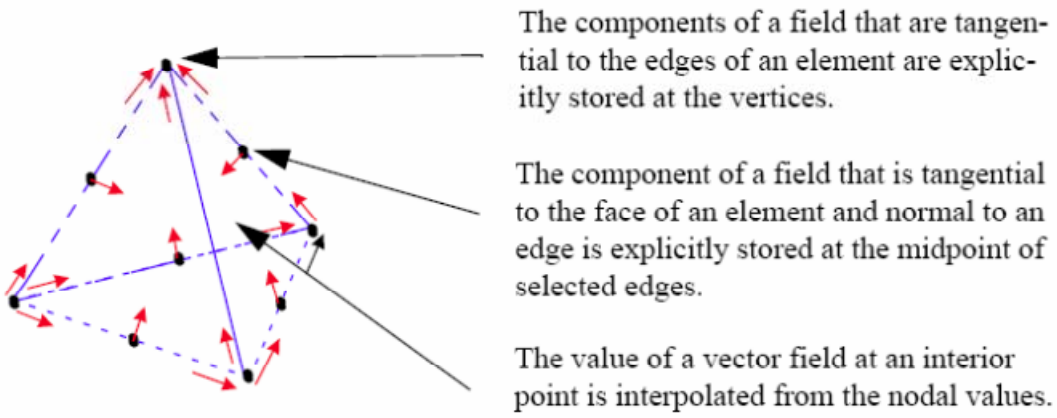


Figure 4-2: Tetrahedron as the fundamental unit of the *finite element* [36] "User's Guide - Maxwell 3D", *Software Version 12.1, Ansoft Inc*, 2009, used under fair use, 2014.

### 4.3.2 Error Evaluation of Maxwell Simulations

Calculated from Maxwell's equation, the field quantities of the nodes are errorless. Meanwhile, due to the basis function built for each unit, the approximation introduces errors in the field solution of the interior points of the tetrahedron. Thus, it is expected that the smaller volume the unit occupies, the less error is generated. Therefore, in the Maxwell simulation, high accuracy always means applying a large number of fundamental units. However, the huge amount of calculations also requires more computer power, which might become a restriction for researchers. In this case, error evaluation of simulations could help in finding the error of the desired object, improve the specific accuracy, and utilize the limited computer power effectively.

Mesh is not unique for analyzing the field. Every time the Maxwell simulation is executed, the mesh arrangement alters, which affects the error evaluation of the entire field. As stated above, the source of simulation error is from the approximation method based on the basis function with nodes as edge conditions. In the other words, the error is determined by the arrangement of the nodes. Figure 4-3 presents a 1D FEM example to illustrate how error is generated. The solid curve is the actual field. After building up the mesh, 6 nodes are applied to the field solver. When their field quantities are calculated, the field between two nodes is approximated by the linear basis function, which is depicted as dotted lines in the figure. Thus, the connected dash lines construct the FEM field solution. Obviously, the difference between the solid and dotted curves is the error. The principle is that more nodes return less error. Figure 4-4 shows another mesh arrangement with the same number of nodes applied to the exact same field. Since the coordinates of the nodes are shifted, their new field values modify the basis functions, and as such the error. This uncertainty of the error, as well as the solution, create an issue with simulation accuracy: if the field variation from the magnetic particle is not significant compared to the error, the inductance change cannot be detected from the simulation results. In order to deal with this problem, an error evaluation method of the field and inductance variations is discussed below.

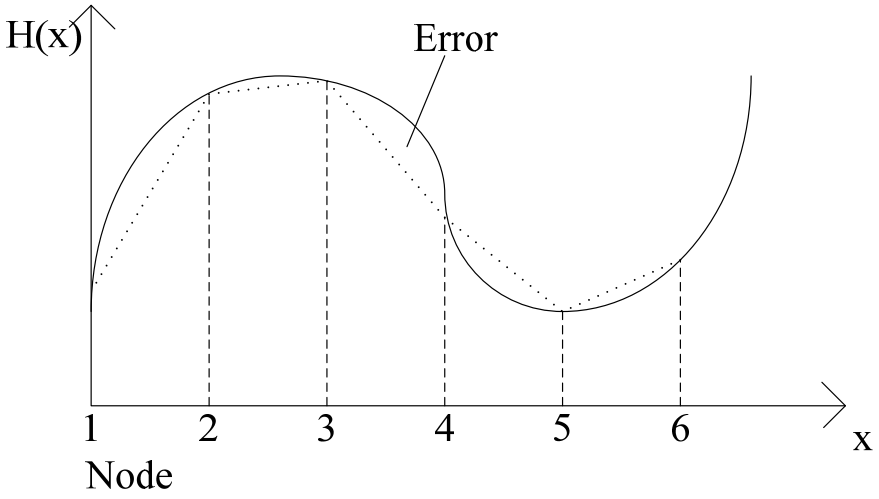


Figure 4-3: 1D FEM field solution with 6 nodes.

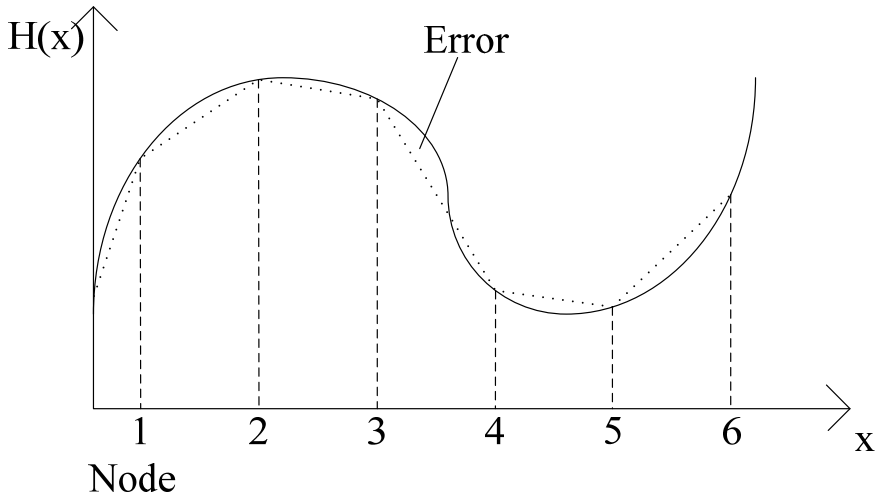


Figure 4-4: Another 1D FEM field solution with 6 nodes.

In the previous Maxwell simulations, the same simulation is executed twice for detecting the field variation by inserting one iron nanoparticle, one with the object of the particle and one without. However, since modifying the design model requires re-building the mesh, the results failed to be useful due to the error issue as discussed above. To solve this problem, the particle object is kept in the model and the material of air is assigned to it for the simulation without the particle. In addition, with the restriction of computer power, applying a huge amount of *finite elements* to the mesh of the entire model to reduce error is not feasible. However, the mesh density of the particle object can be increased by filling in more elements, which improves the specific accuracy. To illustrate the error analysis of the new simulation, Figure 4-5, the 1D field plot without the particle, and Figure 4-6, the one with the particle, are compared. Both simulations share the same mesh arrangement of 10 nodes. The nodes 2-6 are applied to the particle object, while the others are applied to the rest of the model. In the error evaluation of Figure 4-5, the actual field (solid curve) is denoted as $H_1$, the actual field in the particle as $H_{p1}$, the actual field in the rest model as $H_{r1}$, the calculated field in the particle (red dot lines) as $HS_{p1}$, the calculated field in the rest of the model (blue dot lines) as $HS_{r1}$, the

error in the particle as $HE_{p1}$, and the error in the rest model as $HE_{r1}$. Hence, the field equation can be expressed as follows:

$$H_1 = \begin{cases} H_{p1} & particle \\ H_{r1} & rest \end{cases} \tag{4-3}$$

$$= \begin{cases} HS_{p1} + HE_{p1} & particle \\ HS_{r1} + HE_{r1} & rest \end{cases} \tag{4-4}$$

With same setting in the field in Figure 4-6, similarly:

$$H_2 = \begin{cases} H_{p2} & particle \\ H_{r2} & rest \end{cases} \tag{4-5}$$

$$= \begin{cases} HS_{p2} + HE_{p2} & particle \\ HS_{r2} + HE_{r2} & rest \end{cases} \tag{4-6}$$

The actual field variation, $\Delta H$, is calculated as:

$$\Delta H = H_2 - H_1 = \Delta HS + \Delta HE \tag{4-7}$$

$$While\ \Delta HS = \begin{cases} HS_{p2} - HS_{p1} & particle \\ HS_{r2} - HS_{r1} & rest \end{cases}, \Delta HE = \begin{cases} HE_{p2} - HE_{p1} & particle \\ HE_{r2} - HE_{r1} & rest \end{cases} \tag{4-8}$$

where $\Delta HS$ denotes the calculated field variation from simulation results, and $\Delta HE$ is the error. $\Delta HE$ contains four terms, $HE_{p1}$, $HE_{p2}$, $HE_{r1}$, and $HE_{r2}$. From both figures it is clear that, if the mesh density of the particle object is much higher than the rest of the model, the error terms $HE_{p1}$ and $HE_{p2}$ could be as small as negligible. Moreover, since the particle size is extremely small (50 nm diameter) compared to the inductor size (over 100 μm), the field variation due to magnetization affects very limited space around the particle, as its effect propagation attenuates dramatically with distance. Therefore, in the rest model, $H_{r1} \approx H_{r2}$ and, hence, $HE_{r1} \approx HE_{r2}$. With the above error evaluation, $\Delta HE$ is small enough to make $\Delta HS \approx \Delta H$. Hence, the field variation from the new simulation can detect the inductance change by the magnetic particle. The definition of inductance referring to 1D field is expressed as follows:

$$L = \frac{\int_x \mu H dx}{I} \tag{4-9}$$

Then the inductance variation is:

$$\Delta L = L_2 - L_1 = \frac{\int_r \mu_0 H_{r2} dx + \int_p \mu_1 H_{p2} dx}{I} - \frac{\int_r \mu_0 H_{r1} dx + \int_p \mu_0 H_{p1} dx}{I} \tag{4-10}$$

$$= \frac{\int_r \mu_0 (H_{r2} - H_{r1}) dx + \int_p (\mu_1 H_{p2} - \mu_0 H_{p1}) dx}{I} \tag{4-11}$$

$$= \frac{\int_r \mu_0 (HS_{r2} - HS_{r1}) dx + \int_p (\mu_1 HS_{p2} - \mu_0 HS_{p1}) dx}{I} + \hookleftarrow \tag{4-12}$$

$$\mapsto \frac{\int_r \mu_0 (HE_{r2} - HE_{r1}) dx + \int_p (\mu_1 HE_{p2} - \mu_0 HE_{p1}) dx}{I} \tag{4-13}$$

$$= \Delta LS + \Delta LE \tag{4-14}$$

where $\mu_0$ is the permeability of air, $\mu_1$ is the permeability of magnetic material, $\Delta LS$ is the inductance change from the Maxwell simulations, and $\Delta LE$ is the error term. By applying the error evaluation of the field as analyzed above, the similar conclusion could be obtained that $\Delta LS \approx \Delta L$, since $\Delta LE$ is relatively negligible. In conclusion, to reach the desired simulation accuracy with limited computer power, the mesh density of the iron nanoparticles should be much higher than the rest of the model.

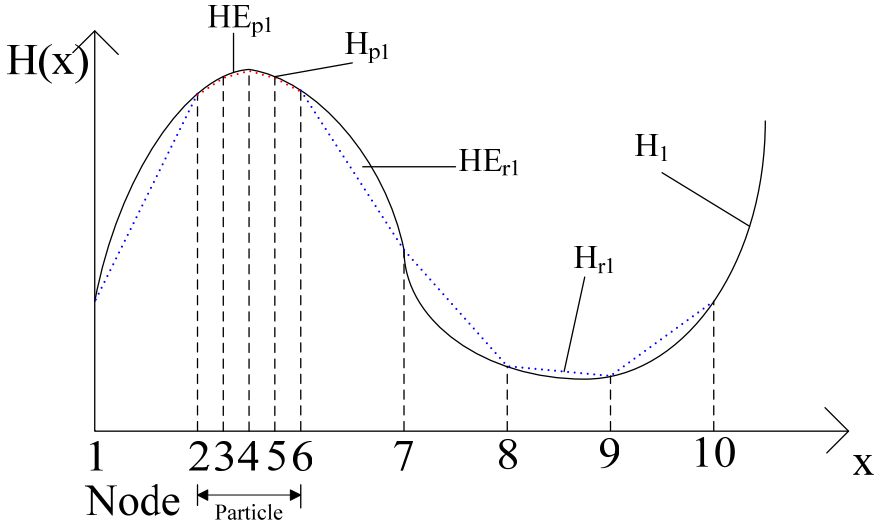


Figure 4-5: 1D FEM field solution without the iron nanoparticle.

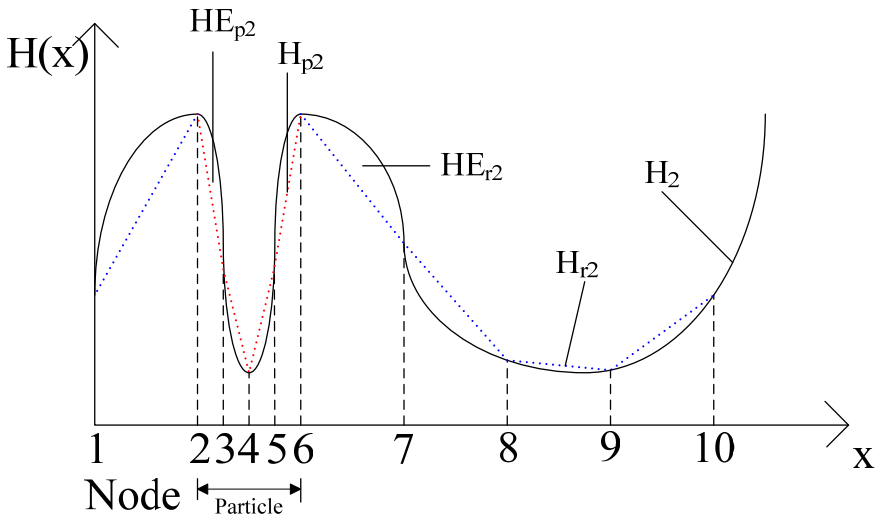


Figure 4-6: 1D FEM field solution with the single particle.

## 4.4 Ansoft Maxwell Simulation Results

To verify the design concept of the biosensor system, four simulations with different parameters were conducted.

### 4.4.1 Verification of the Magnetic Effect Uniformity

In order to prove the location-independent uniformity of the magnetic effects of the system, a simulation was performed with one single iron nanoparticle placed at 6 locations that covered the highest and lowest field strengths in the sensing plane. The simulation plot shown in Figure 4-7 indicates a 7% worst-case inductance deviation over all 6 positions of the nanoparticle, with the same percentage of the resultant frequency-shift in each case. This simulation result matches the analysis of the magnetic field uniformity in the Section 3.4.

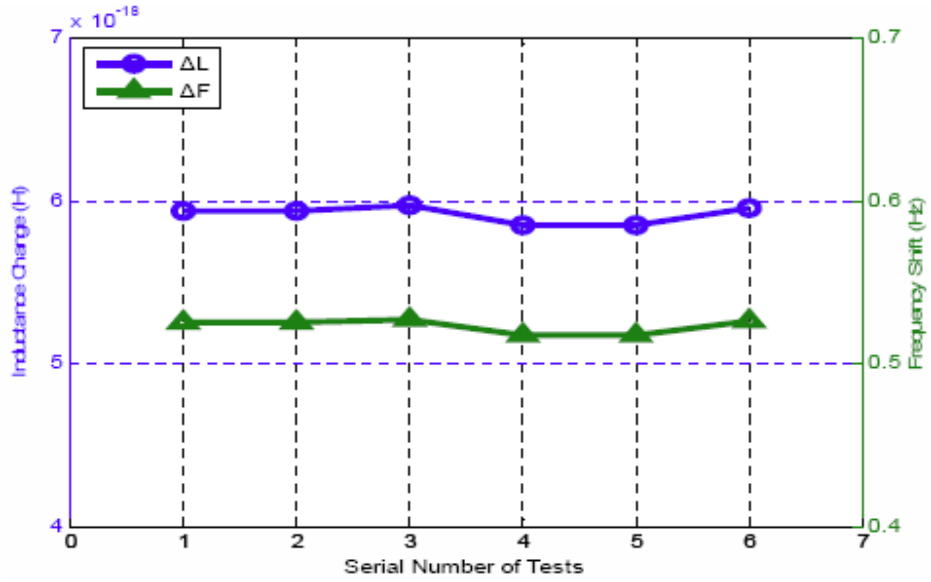


Figure 4-7: Magnetic effects of single particle placed in six positions.

### 4.4.2 Linearity of Magnetic Effects and Particle Number

In the case of the uniformity of the magnetic effects from every single iron nanoparticle in the sensing plane, the sensor is able to detect a linear change from the different number of particles. Figures 4-8 and 4-9 illustrate that, when multiple particles (0~100) are randomly distributed, the sensing system will display linear changes in inductance and frequency for each additional particle added to the sensing region. Hence, the simulation results provide high confidence that the sensing accuracy is such that single particles can be differentially sensed.

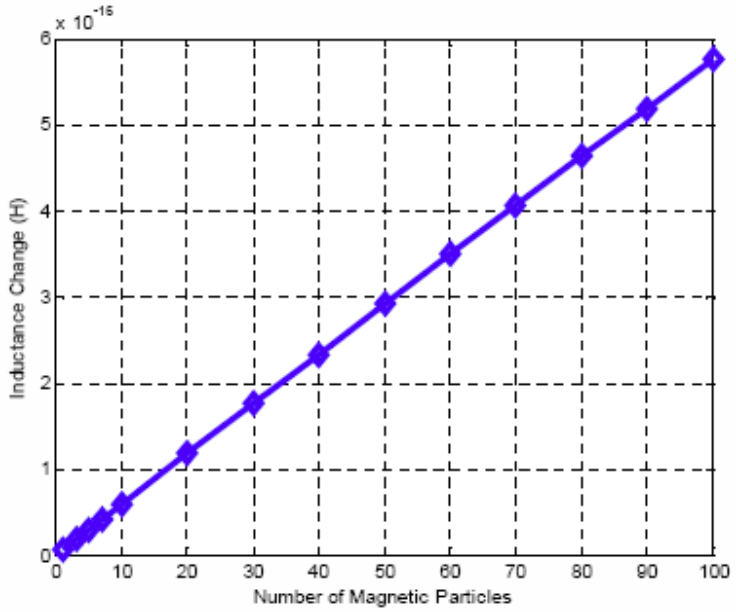


Figure 4-8: Inductance change of multiple randomly placed particles.

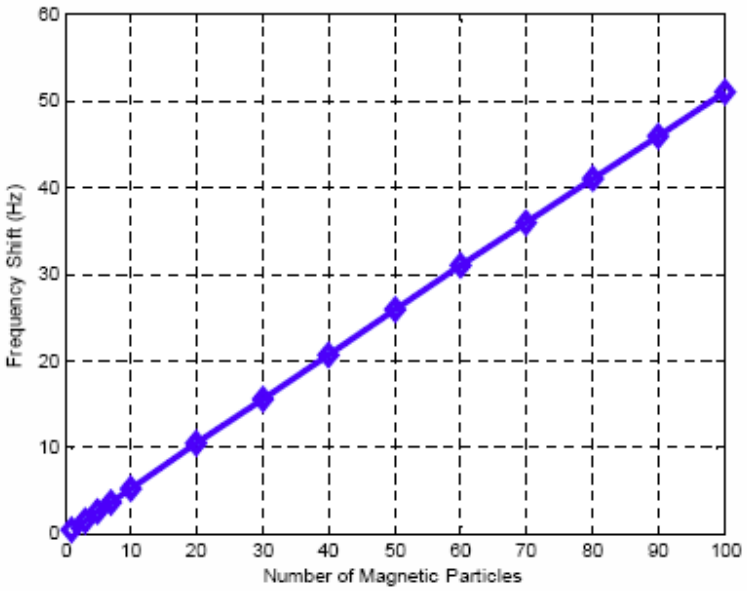


Figure 4-9: Frequency shift of multiple, randomly placed particles.

### 4.4.3 Simulation of Particles in a Single Pathogen

In reality, the sensed unit by this biosensor is a biological organism, but not one single iron nanoparticle. Multiple particles are in random positions inside the biological, which is a 3D volume. The previous simulations are based on the assumption that all particles are located in the same sensing plane, which does not model the real case accurately.

To simulate the distribution of iron particles within a single pathogen, iron nanoparticles are randomly distributed in a cylinder with a 3 μm length and a 1 μm diameter [34]. This cylinder is then placed inside the sensor such that the longitudinal center line of the cylinder coincides with the sensing plane, as shown in Figure 4-10. This means that the sensing region with the most uniform field strength cuts through the cylinder longitudinally. Thus, the particles located above this plane generate less inductance change, and the particles below the plane generate more inductance change. The plot in Figure 4-11 illustrates that, in the range of ±0.5 μm from the sensing plane, the inductance change caused by a single particle is linearly proportional to the vertical distance from the plane. Therefore, a large number of randomly distributed particles will neutralize the non-uniform magnetic effect of a single particle caused by vertical location offsets and essentially produce a result as if all particles were exactly on the sensing plane. Simulation results shown in Figure 4-12 indicate that, with the increasing number of over 100 randomly placed iron particles in the cylinder, the dynamic range of inductance change is reduced to below 0.5%. In reality, with multiple pathogens in the sample container, the particle amount will be much more than 100, which will generate a negligible deviation by the vertical offsets.

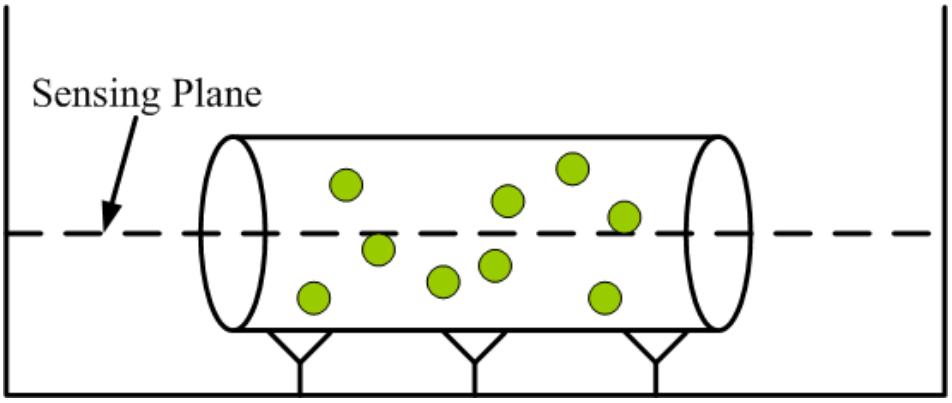


Figure 4-10: Cylinder as the pathogen model in the sensing plane.

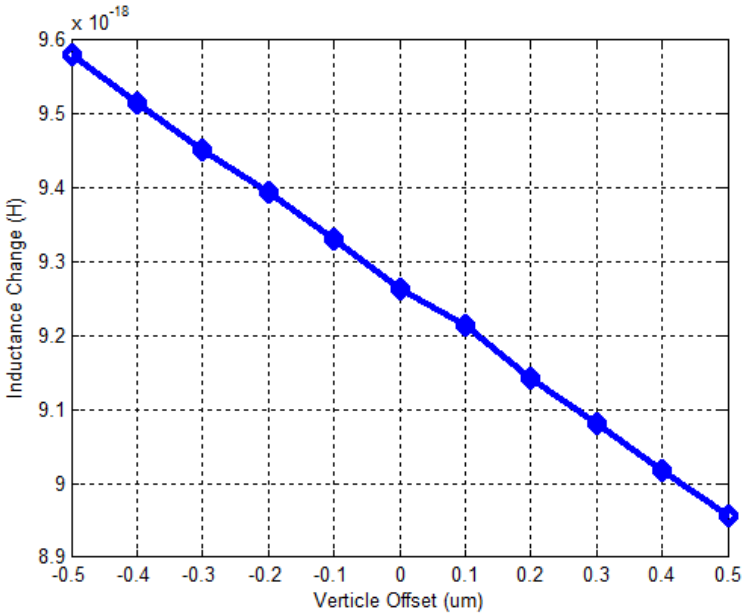


Figure 4-11: Inductance change of single particle with vertical offsets.

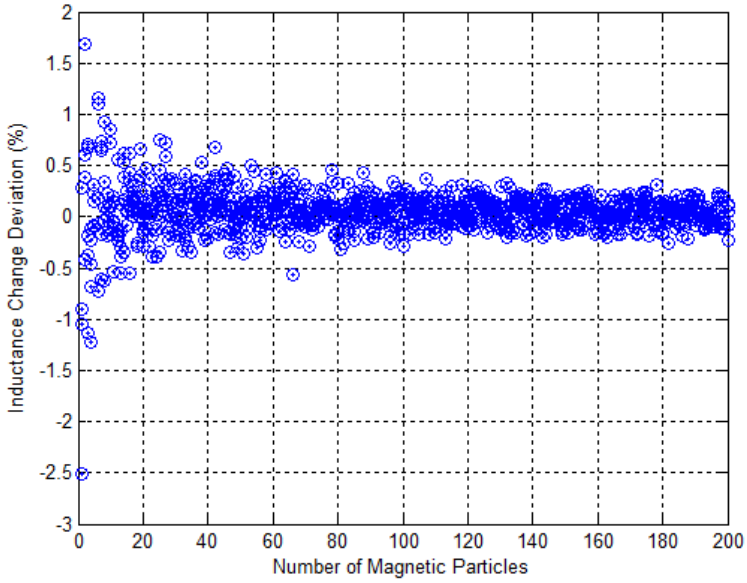


Figure 4-12: Inductance change deviation of randomly distributed particles in the biological model.

### 4.4.4 Simulation of Multiple Pathogens

Similar simulations used pathogens as sensed units. To evaluate the location dependent deviation of magnetic effects, the cylinder described above, but with 20 particles inside of it, is placed at 10 locations covering the highest and lowest field strengths on the sensing plane. The simulation plot shown in Figure 4-13 indicates a 7% worst-case deviation of the inductance change over all 10 positions, with the same percentage of the resultant frequency-shift in each case. This result is same as the one in the simulation in Section 4.4.1, which again proves the insignificant effect from the particle's vertical offset. Furthermore, by assuming that every pathogen consumes the same amount of particles and multiple cylinders with constant size are randomly distributed, the sensed changes in inductance and frequency are linearly proportional for each additional biological added to the sensing region (Figure 4-14). Therefore, the exact number of cylinders, which model the targeted pathogens, can be differentially detected. Note that, in reality, the size of every pathogen is not identical, and the amount of iron nanoparticles

is always different. However, the deviation in both factors is in a dynamic range that should not be large due to the single species of the targeted pathogen. Therefore, the average level could be determined from a certain number of biological experiments, which should be examined in future studies.

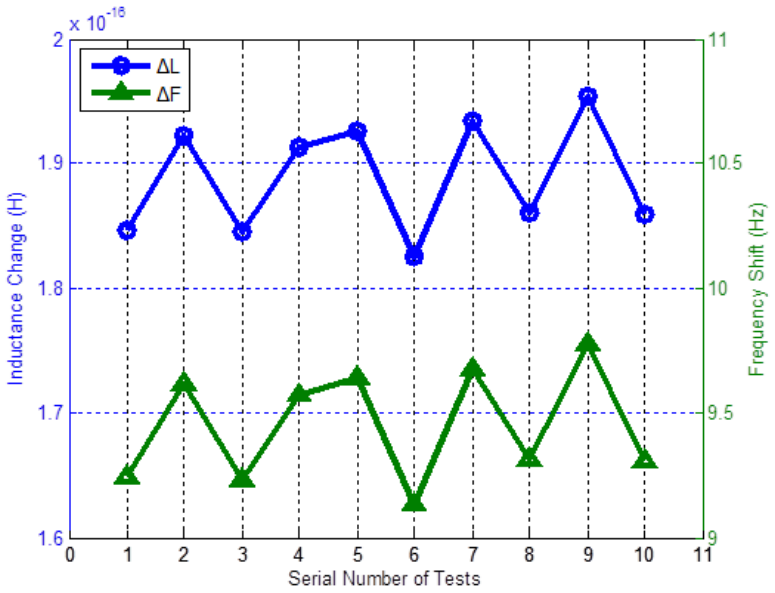


Figure 4-13: Magnetic effects of a single biological model placed in 10 positions.

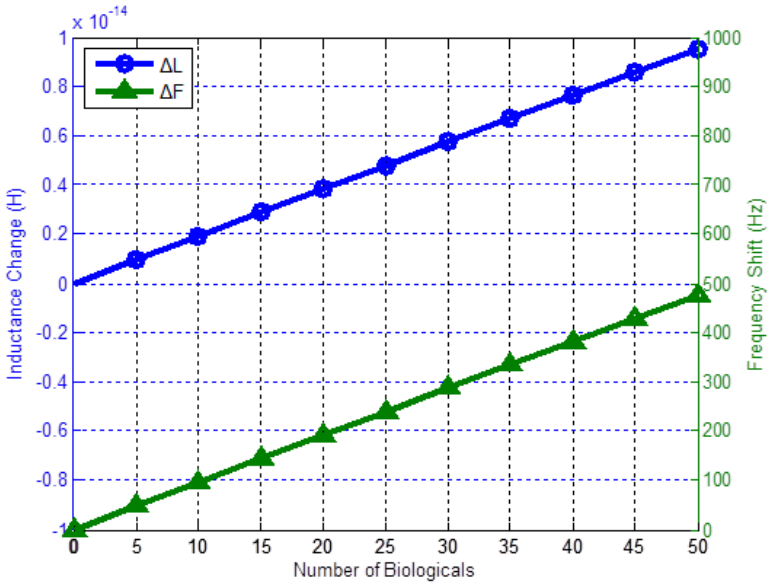


Figure 4-14: Magnetic effects of multiple, randomly placed biological models.

## 4.5 Summary

This chapter describes how to set up the software, Ansoft Maxwell, for the simulation accuracy. Four simulations of the designed sensor head provide a proof of the sensing concept. The simulations cover the cases including single and multiple iron nanoparticles, single and multiple biological pathogens. Different sources of deviations are also discussed and evaluated. Overall, the simulation results show a high level of the system sensing accuracy, which is a significant improvement over earlier designs..

# Chapter 5: Sensing Signal Transformer: The LC Oscillator

## 5.1 Introduction

After the core component, the senor head, of the biological sensor system is ready, the design process moves to regular circuit level design. As described in Chapter 2, the LC oscillator is used to transform the sensed variation of the magnetic effect, inductance change, to the shift of the oscillated signal frequency. This chapter discusses the design of a robust and stable LC oscillator, based on the 180 nm technology IBM_CMOS_7RF.

## 5.2 Circuit Schematic: Cross-coupled Structure

In many oscillator designs, the cross-coupled structure has the advantages of being simple and stable. Due to its ease of implementation, differential operation, and relatively good phase noise, cross-coupled LC oscillators are widely used in high frequency circuit design [37][38][39]. Figure 5-1 shows the schematic of the designed LC oscillator. The left part, including the LC tank and transistors *M1~4*, is a classic cross-coupled design. In general, to make a system oscillate, two necessary conditions, called Barkhausen criteria, must be satisfied, as expressed below.

$$\begin{cases} |H(j\omega_0)| \geq 1 \\ \angle H(j\omega_0) = 180° \end{cases} \tag{5-1}$$

The system open loop gain, $|H(j\omega_0)|$, at the oscillation frequency $\omega_0$ has to be larger than 1. The phase shift, assuming negative feedback, must be 180 degrees, or 360

degrees if positive feedback. The cross-coupled structure has two stages in a cascade, where each stage is formed by a push-pull inverter. Thus, a positive feedback is guaranteed as two cascaded inverters provide a phase shift of 360 degrees, and each stage contributes zero frequency-dependent phase shift at resonance, as shown in Figure 5-2. The loop gain is analyzed by the combination of the cascaded inverters and the LC tank. (Details of designing transistors in the inverters is discussed in later sections of this chapter.) Although this oscillator is a differential design, only the individual end is used. If differential outputs are used, a circuit of differential-to-single end converter is needed for following digital circuits, which increases the design complexity and circuit area. The right part of the schematic, composed of transistors *M5~10*, is obviously three chained inverters. They are simply designed as signal amplifiers for converting the sinusoid waveform, the output of the left part, to the square waveform as a digital signal. Since the oscillated signal at point *B* in the schematic will be sampled by a certain time for counting the frequency, its phase does not have to be the same as *A*.

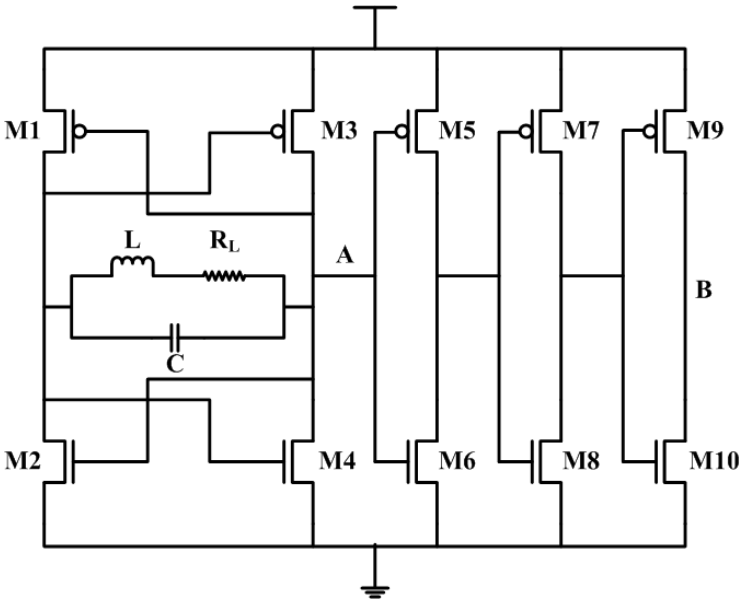


Figure 5-1: Schematic of the cross-coupled LC oscillator.

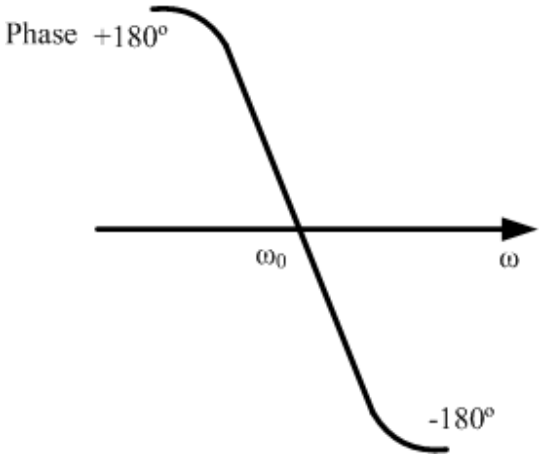

Figure 5-2: Phase of the cross-coupled topology.

## 5.3 Parameter Extraction of the Inductor

Once the circuit schematic is designed, the next step is to identify the proper values for the circuit components. The parameters of the inductor, including inductance $L$ and parasitic resistance $R_L$ in the LC tank model, are certainly determined in advance. Therefore, to guarantee the accuracy and credibility of the simulations of the LC oscillator design, accurate and reliable parameter extraction becomes significant. In the following sub-sections, two magnetic simulation software programs, Ansoft Maxwell and Sonnet, are used for the design of parameter extraction due to their respective limitations. After a comparison, appropriate values of $L$ and $R_L$ will be determined. Note that in both software simulations, the final extracted values of $L$ and $R_L$ are calculated from the end-to-end impedance, which means the parasitic effects, like eddy current and parasitic capacitance, are automatically integrated.

### 5.3.1. Ansoft Maxwell Extraction

The same Ansoft Maxwell inductor model, as shown in Figure 4-1, is used for parameter extraction. Since the sensor system is designed with a frequency below 1 GHz, the frequency range for the simulation is set from DC to 1 GHz. Figure 5-3 shows the plots of the extracted $L$ and $R_L$, as well as the calculated $Q$ factor. From the frequency of DC to

1GHz, the inductance $L$ slightly drops from 12.1 nH to 11.9 nH, while the parasitic resistance $R_L$ rises from 20.1 Ω to 23.8 Ω, which yields an increment of the $Q$ factor up to 3.1. The resistance variation comes from the skin effect of the thick top metal layer, which is expected. The expressions of the extraction for these parameters are stated as follows.

$$R = \mathrm{Re}(Z(current1, current1)) \tag{5-2}$$

$$L = \mathrm{Im}(Z(current1, current1))/\omega \tag{5-3}$$

$$Q = \mathrm{Im}(Z(current1, current1))/\mathrm{Re}(Z(current1, current1)) \tag{5-4}$$

where $Z$ stands for the impedance of the coil, and *current1* is the current flowing into the inductor. Ansoft Maxwell software does not define ports for analysis. As shown in the inductor model in Figure 4-1, both ends of the inductor are connected as a closed loop for the excitation of the single current source. Therefore, it is equivalent to single port analysis, except that a small amount of extra inductance and resistance of the connection are counted.

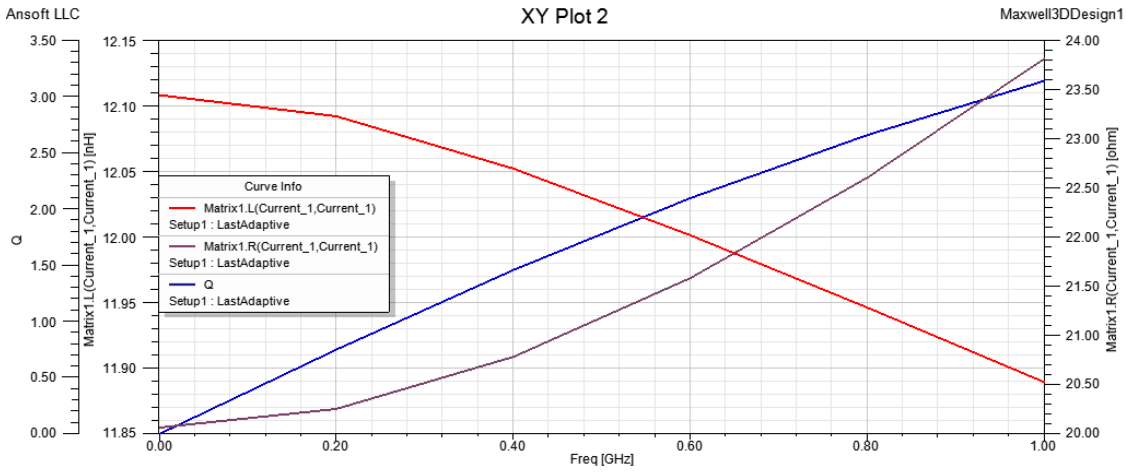


Figure 5-3: Plots of $L$, $R_L$, and $Q$, with the frequency range of DC to 1 GHz.

### 5.3.2. Sonnet Extraction

Sonnet is professional electromagnetic (EM) software that is optimal for high frequency analysis [40]. The inductor model used in Sonnet is imported from the Computer-aided

Design (CAD) software of Cadence Virtuoso (shown in Figure 5-4). Note that the model is the same as the one used in Ansoft Maxwell. Figure 5-5 plots the extraction results of $L$, $R_L$, and $Q$. With the frequency from DC to 1 GHz, inductance changes from 12.5 nH to 12.7 nH, while the parasitic resistance $R_L$ rises from 17 Ω to 21.5 Ω, which yields an increment of the $Q$ factor up to 3.6. Note that the Sonnet simulation uses port analysis. Therefore, the extraction can be expressed as follows.

$$R = \mathrm{Re}(Z(port1, port1)) \tag{5-5}$$

$$L = \mathrm{Im}(Z(port1, port1))/\omega \tag{5-6}$$

$$Q = \mathrm{Im}(Z(port1, port1))/\mathrm{Re}(Z(port1, port1)) \tag{5-7}$$

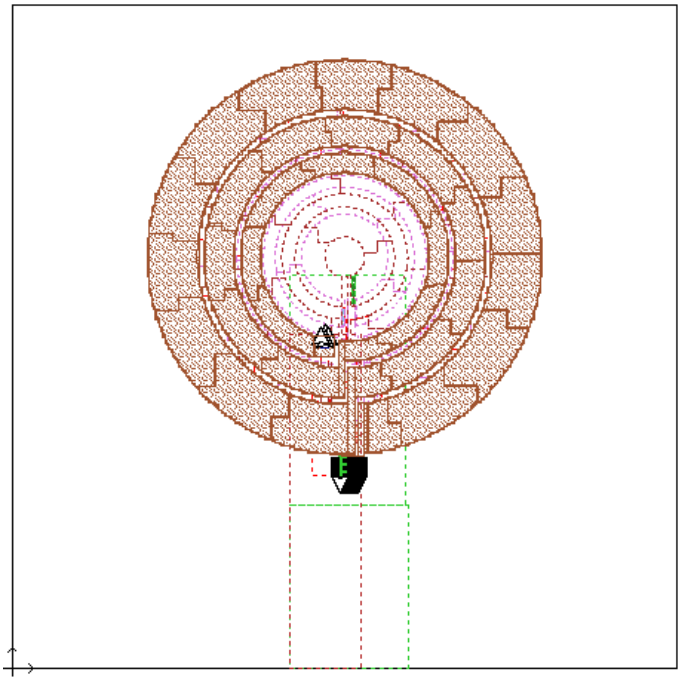

Figure 5-4: The inductor model in the EM software Sonnet.

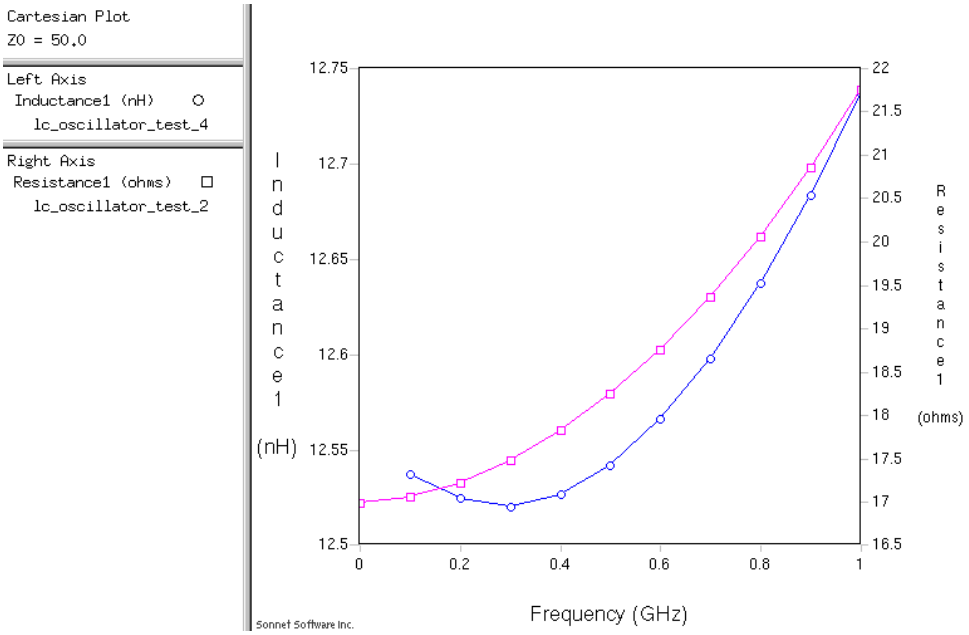


(a) $L$ vs Frequency and $R_L$ vs Frequency

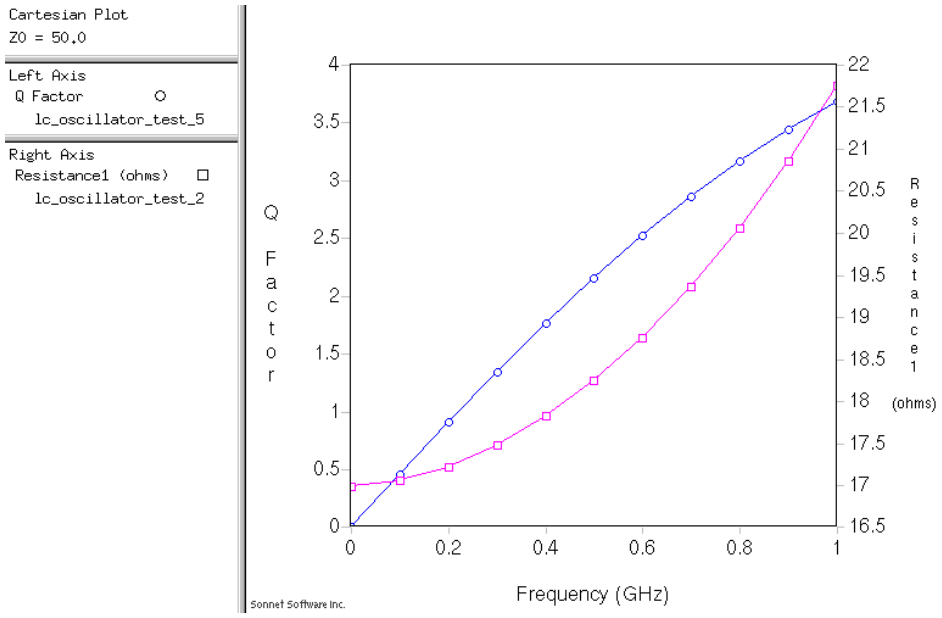


(b) $Q$ vs Frequency

Figure 5-5: Plots with the frequency range of DC to 1 GHz in Sonnet.

### 5.3.3. Comparison

By comparing the extraction results from Ansoft Maxwell and Sonnet, inductance $L$ is quite similar from both, with a small difference of <5% which could be explained from their respective limitations in the simulation solvers. Unlike regular on-chip inductors, which are generally square-shaped, the design in this project has circular edges. The meshing shape in Sonnet is a cube, which means it cannot fit the circular edge as well as the tetrahedron meshing in Ansoft Maxwell. This restraint in matching the models yields error. Although this error could be reduced by assigning very small mesh size, the model complexity and the computer power restrict the minimum mesh size to 0.5 μm. Due to the flexible setting of the meshing, Ansoft Maxwell yields higher accuracy than Sonnet by using the same computer power. However, a deficiency in the Ansoft Maxwell simulator is that, at high frequency, the magnetic field solver does not include the electric field solution, which means the effect of parasitic capacitance is not considered. Parasitic capacitance could be modeled as a capacitor paralleling the inductor if it is not integrated. This capacitor becomes more and more dominating over the inductor with increasing frequency and neutralizes the overall inductance at the self-resonant frequency. Generally, this parasitic capacitance is very small and becomes a non-negligible effect when the frequency approaches several GHz. Figure 5-6 shows the extra simulation plots of $L$ and $Q$ factor in Sonnet when the frequency range is expanded to 10 GHz. Although the frequency step from 1 to 10 GHz is as large as 1 GHz, the trend of the curves is sufficient to observe that the parasitic capacitance becomes significant only when the frequency exceeds 6 GHz. Therefore, at the relative low frequency of less than 1 GHz, the error of the overall inductance caused by this parasitic effect could be ignored. Hence, the Ansoft Maxwell extracted inductance $L$, 11.9 nH, is used in the model.

The extracted parasitic resistances $R_L$ from both software programs has a difference of about 3 Ω, which is the extra resistance from the end-to-end connection of the model in Ansoft Maxwell, as discussed above. Deducting this difference results in that both extractions give a similar result of around 20 to 21 Ω at 1 GHz. However, considering the circuit layout on the chip, extra conduction is needed for the connections

at the ends of the inductor, the capacitor in the LC tank, and the gate terminals of the transistors. This extra resistance is considered design tolerance. Experience indicates that 2 to 3 Ω for these traces with proper widths is a reasonable value. Therefore, 24 Ω of $R_L$ is used for the model. Note that it is the value at 1 GHz frequency, though the oscillated frequency will be less. This situation is also a design tolerance that guarantees the working performance of the designed LC oscillator. Hence, since the chosen oscillation frequency is 800 MHz, $Q$ factor is found to be 2.5.

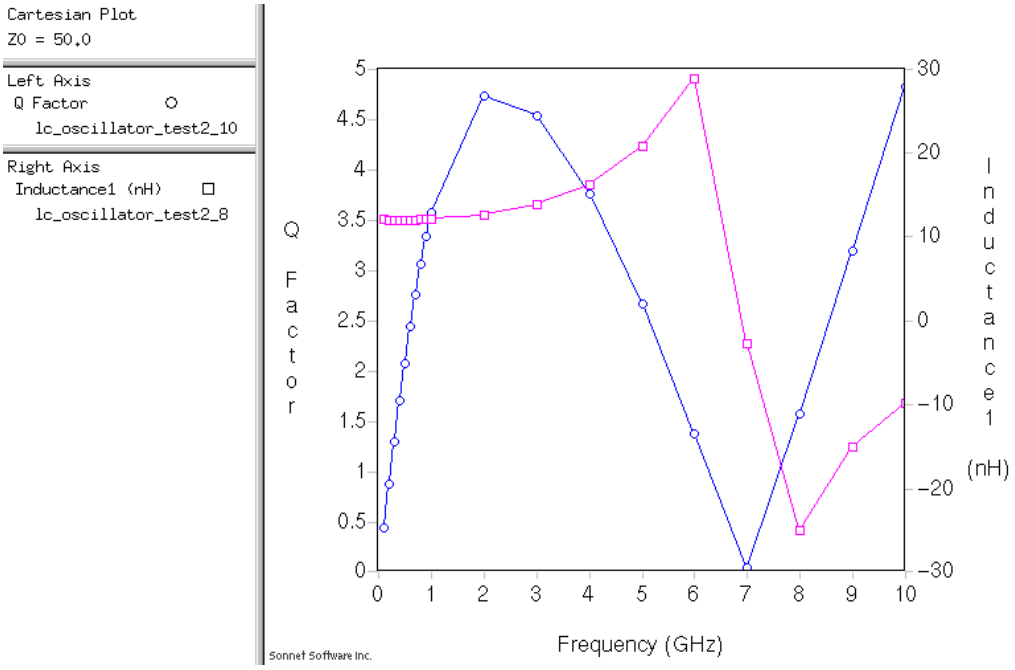


Figure 5-6: The image frame for the third experiment.

## 5.4 Design Parameters of the Transistors

Once the circuit schematic is chosen, the next step is the choice for proper design parameters of transistors *M1~10*. The three chained inverters in the right part of the oscillator schematic (shown in Figure 5-1) do not have complex requirements, so they are relatively easy to handle. In comparison, the four transistors *M1~4* determine the performance of the LC oscillator and need to be carefully designed.

The major purpose of the cross-coupled transistors is to compensate for the lost energy of the LC tank by parasitic resistance $R_L$, which performs as a "negative resistance." The oscillation concept is explained as follows [41]. Figure 5-7(a) shows an RLC circuit stimulated by a current impulse at a certain amount of energy. The energy that is being transferred inside the LC tank causes the oscillation. However, this oscillation decays by cycles since, in every cycle, some of the energy that reciprocates between $L_P$ and $C_P$ is lost in the form of heat in the resistor $R_P$. Figure 5-7 (b) shows what occurs if a negative resistor $-R_P$ is added in a parallel position with $R_P$--$R_P$ is neutralized since $R_P$//($-R_P$) is infinity resistance. Consequently, the oscillation will last forever because the energy to heat $R_P$ is totally provided by $-R_P$ and not the LC tank. In other words, $-R_P$ acts as an energy source. Since no passive circuit component acts like a negative resistor, an active circuit is needed for this purpose.

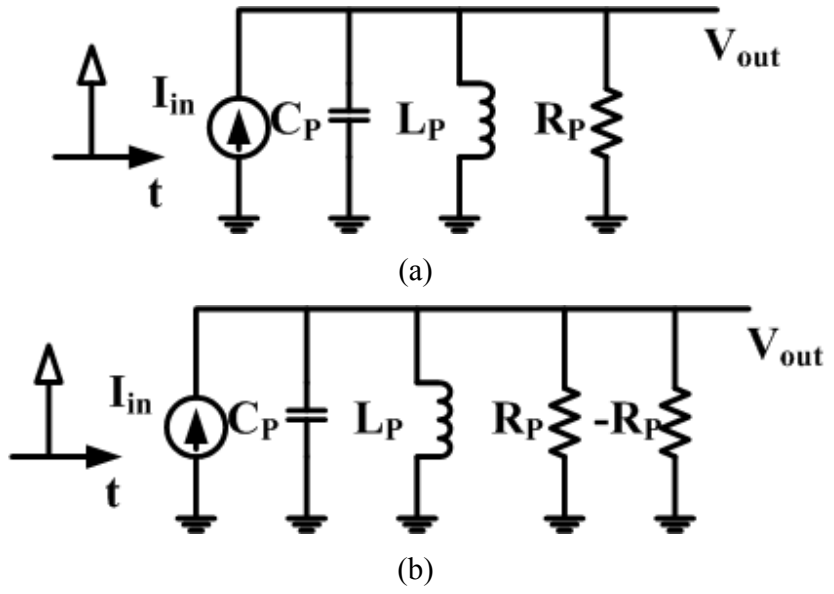


Figure 5-7: (a) RLC tank with decaying oscillation, (b) addition of negative resistance to cancel loss in $R_P$. [41] Behzad, Razavi. "Design of analog CMOS integrated circuits." *International Edition* (2001), used under fair use, 2014.

To create a circuit that provides negative resistance, the transistors of cross-coupled structure are redrawn in Figure 5-8 (a). Figure 5-8 (b) shows its small-signal model. The equivalent resistance $R_{eq}$ can be derived as follows.

$$\begin{cases} I_x = -g_{mp}V_2 - \dfrac{V_1}{r_{op}} - g_{mn}V_2 - \dfrac{V_1}{r_{on}} \\ I_x = g_{mp}V_1 + \dfrac{V_2}{r_{op}} + g_{mn}V_1 + \dfrac{V_2}{r_{on}} \\ V_x = V_2 - V_1 \end{cases} \tag{5-8}$$

$$R_{eq} = \frac{V_x}{I_x} = \frac{-2}{g_{mp} + g_{mn} - \dfrac{1}{r_{on} // r_{op}}} \tag{5-9}$$

$$\approx \frac{-2}{g_{mp} + g_{mn}}, \sin ce \;\; g_{mp} + g_{mn} \geq \frac{1}{r_{on} // r_{op}} \tag{5-10}$$

where the transconductances $g_m$ of both NMOS transistors are the same since the cross-coupled structure is symmetric, and so do the both PMOS transistors. $g_{mn}$ and $g_{mp}$ denotes the transconductance of the NMOS and PMOS transistors. $r_{on}$ and $r_{op}$ are the resistors of channel-length modulation that model the I-V behavior of the NMOS and PMOS transistors. If $R_{eq}$ is replaced with $-R_P$ in Figure 5-7 (b), the equivalent resistance of $R_{eq}//R_P$ has to be less than zero to halt the consumption of energy from the LC tank. Therefore, the following condition is required.

$$R_p + R_{eq} = R_p - \frac{2}{g_{mp} + g_{mn}} \geq 0 \tag{5-11}$$

$$g_{mp} + g_{mn} \geq \frac{2}{R_P} \tag{5-12}$$

To determine $R_P$, the LC tank model in the schematic could be converted to an equivalent parallel RLC circuit, as illustrated in Figure 5-9. The extracted value of parasitic resistance $R_L$ is 24 Ω, and the $Q$ factor near 800 MHz is around 2.5 (discussed in Section 5.3.3). Hence, the converted $R_P$ is calculated as follows.

$$R_P = R_L(Q^2 + 1) = 174\,\Omega \tag{5-13}$$

Therefore, the minimum required value of $g_{mn}+g_{mp}$ is 2/174 = 11.5e$^{-3}$. Using the well known expression below (5-14), the parameter of the NMOS transistors can be roughly approximated.

$$g_{mn} = \mu_n C_{ox} \frac{W_n}{L}(V_{GSn} - V_{THn})(1 + \lambda_n V_{DSn}) \tag{5-14}$$

$$g_{mp} = \mu_p C_{ox} \frac{W_n}{L}(V_{GSp} - V_{THp})(1 + \lambda_p V_{DSp}) \tag{5-15}$$

where $\mu_n$ and $\mu_p$ are the channel mobility of the NMOS and PMOS transistors, $C_{ox}$ is the gate oxide capacitance per unit area, $W_n$ and $W_p$ are the widths of the transistors, $L$ is the channel length, $\lambda_n$ and $\lambda_p$ are the channel length modulation coefficients, $V_{GSn}$ and $V_{GSp}$ are the gate-source voltages, $V_{DSn}$ and $V_{DSp}$ are the drain-source voltages, $V_{THn}$ and $V_{THp}$ are the threshold voltages. Since this design is based on 180 nm technology, $L$ of 180 nm is given. $V_{GS}$ and $V_{DS}$ are assumed to be around the middle operation point, half of *Vdd*, 1.8/2 = 0.9 V. Except for $W_n$, which is the design parameter, the other values can be obtained from the published test results from MOSIS [42]. The calculation shows that the widths of NMOS and PMOS transistors *M1~M4* in the schematic needs to be greater than 10 μm.

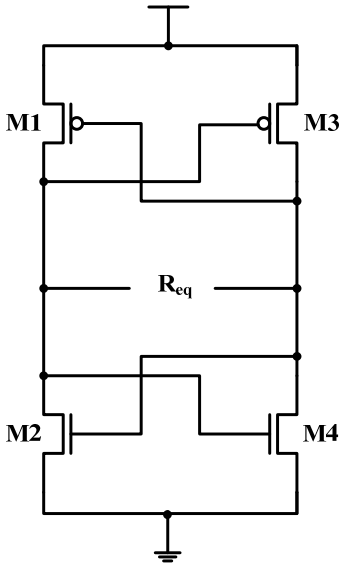


(a)

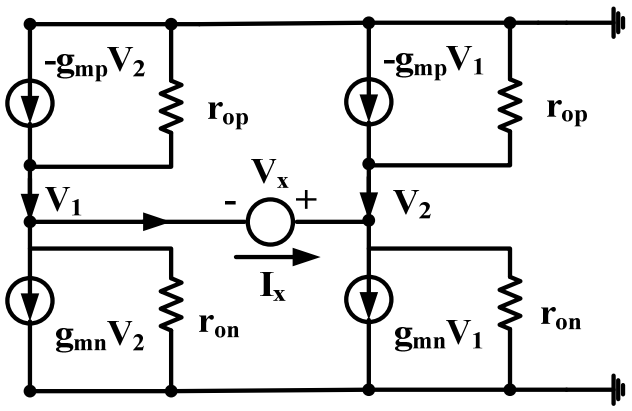


(b)

Figure 5-8: (a) Redrawing of cross-coupled transistors, (b) the equivalent small-signal model to calculate negative resistance $R_{eq}$.

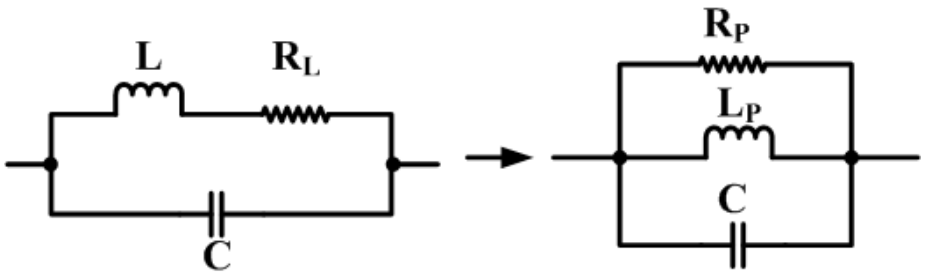


Figure 5-9: Convert the LC tank model to a parallel version.

Once the above design requirement is satisfied, the next consideration is the first condition of Barkhausen criteria for the robust oscillation. The autonomous LC oscillator does not receive energy stimulation from the extra circuits, but relies on self-stimulation by amplifying the tiny noise signal inside the oscillator circuit at the oscillation frequency. Thus, the open loop voltage gain of the oscillator must be greater than 1. The open loop circuit shown in Figure 5-10 has the feedback being cut off. Note that, at the oscillation frequency, the LC tank is equivalent to the 174 Ω single resistor *Rp*. In order to find the voltage gain *Av*, again, assume that the input gate voltage maintains midpoint voltage for the saturation of the transistors; the small-signal model constituted for this analysis is

shown in Figure 5-11. Then the derivation of *Av*, based on the node current analysis, is expressed as follows.

$$\begin{cases} -g_{mp}V_{in} - \dfrac{V_x}{r_{op}} = g_{mn}V_{in} + \dfrac{V_x}{r_{on}} + \dfrac{V_x - V_{out}}{R_p} \\ -g_{mp}V_x - \dfrac{V_{out}}{r_{op}} = g_{mn}V_x + \dfrac{V_{out}}{r_{on}} - \dfrac{V_x - V_{out}}{R_p} \end{cases} \tag{5-16}$$

by substituting $V_x$, the gain is:

$$Av = \frac{V_{out}}{V_{in}} = \frac{(g_{mn} + g_{mp} - \dfrac{1}{R_p})(g_{mn} + g_{mp})}{(g_{mn} + g_{mp} - \dfrac{1}{R_p})\dfrac{1}{R_p} + (\dfrac{1}{r_{on} // r_{op}} + \dfrac{1}{R_p})^2} \tag{5-17}$$

where $r_{on}$ and $r_{op}$ are derived from the equations listed below.

$$I_{DSn} = \frac{1}{2}\mu_n C_{ox}\frac{W}{L}(V_{GSn} - V_{THn})^2(1 + \lambda_n V_{DSn}) \tag{5-18}$$

$$I_{DSp} = -\frac{1}{2}\mu_p C_{ox}\frac{W}{L}(V_{GSp} - V_{THp})^2(1 + \lambda_p V_{DSp}) \tag{5-19}$$

$$r_{on} \approx \frac{1}{\lambda_n I_{DSn}} \tag{5-20}$$

$$r_{op} \approx \frac{1}{\lambda_p I_{DSp}} \tag{5-21}$$

where $I_{DS}$ is the drain-source current flowing through the transistor. $V_{THp}$ is taken from MOSIS testing results [42], and $\lambda_n$ and $\lambda_p$ are about 0.3 as described in the technology design manual [35]. Based on the above expressions, a sweep calculation of sweeping the gate width of the NMOS transistor $W_n$ from 1 to 20 μm, is plotted in Figure 5-12. The PMOS width $W_p$ follows $W_n$ proportionally with the ratio of 1. It can be observed that, to achieve a gain over the unity, $W_n$ is recommended to be no less than 9.2 μm, and so is $W_p$. A larger width returns a better voltage gain, which is good for the oscillator design. However, in contrast, the transistors with a very large width produce considerable parasitic capacitance, which will reduce the oscillation frequency. For example, if both $W_n$ and $W_p$ are over 100 μm, the highest possible oscillation frequency is only 600 MHz

without the customized capacitor in the LC tank. With reduced frequency, the *Q* factor and, hence, the equivalent parallel resistance *Rp* decrease as well. Figure 5-13 shows plots of the sweep calculation with the variation of *Rp*. The gain *Av* is approximately proportional to *Rp*. An *Rp* that is too low will result in poor gain below the unity. Therefore, $W_n$ and $W_p$ should not be designed too high to trade off the target oscillation frequency. Moreover, a large $I_{DS}$ current from excessive transistor widths is a power waste. As an additional comment, the plot in Figure 5-13 also illustrates the importance of a small parasitic resistance $R_L$ from the inductor design, since the trends of $R_L$ and *Rp* are inverse.

Using the above preliminary analysis and calculations, the design room for transistor parameters is found relatively large. In this design room, the final optimized design of transistors *M1~4* is determined by simulations in the software Cadence for ensuring the best performance of the LC oscillator.

In general, an operation bias on the midpoint voltage, an offset from half of *Vdd*, could occur. When this oscillation signal propagate through the three chained inverters and assuming that their operating points are exactly half of *Vdd*, then the duty cycle of the square wave signal at the output of the inverters will have an offset from 50% (illustrated in Figure 5-14). In digital circuits, clock based logic, especially flip-flops, needs sufficient duration of the logic high for the hold time and sufficient duration of the logic low for the setup time. Thus, 50% of the signal duty cycle is best for this oscillation signal. Regulating the duty cycle is accomplished by adjusting the operating points of the chained inverters controlled by their $W_p/W_n$ ratio.

After a number of simulations, the final design of all transistors *M1~10* in the schematic is developed. Their geometry parameters are listed in Table 5-1.

| PMOS | Width (μm) | Length (μm) | NMOS | Width (μm) | Length (μm) |
|---|---|---|---|---|---|
| M1 | 50 | 0.18 | M2 | 45 | 0.18 |
| M3 | 50 | 0.18 | M4 | 45 | 0.18 |
| M5 | 40 | 0.18 | M6 | 35 | 0.18 |
| M7 | 40 | 0.18 | M8 | 35 | 0.18 |
| M9 | 40 | 0.18 | M10 | 35 | 0.18 |

Table 5-1: Geometry parameters of every transistor in the LC oscillator.

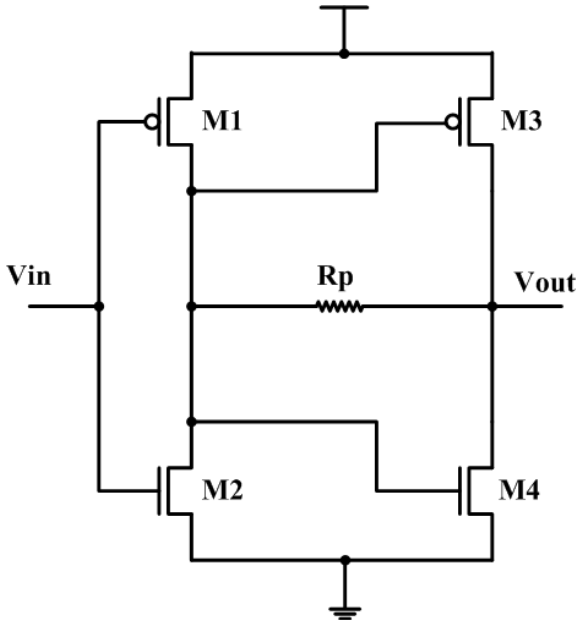


Figure 5-10: Open loop circuit of the cross-coupled structure.

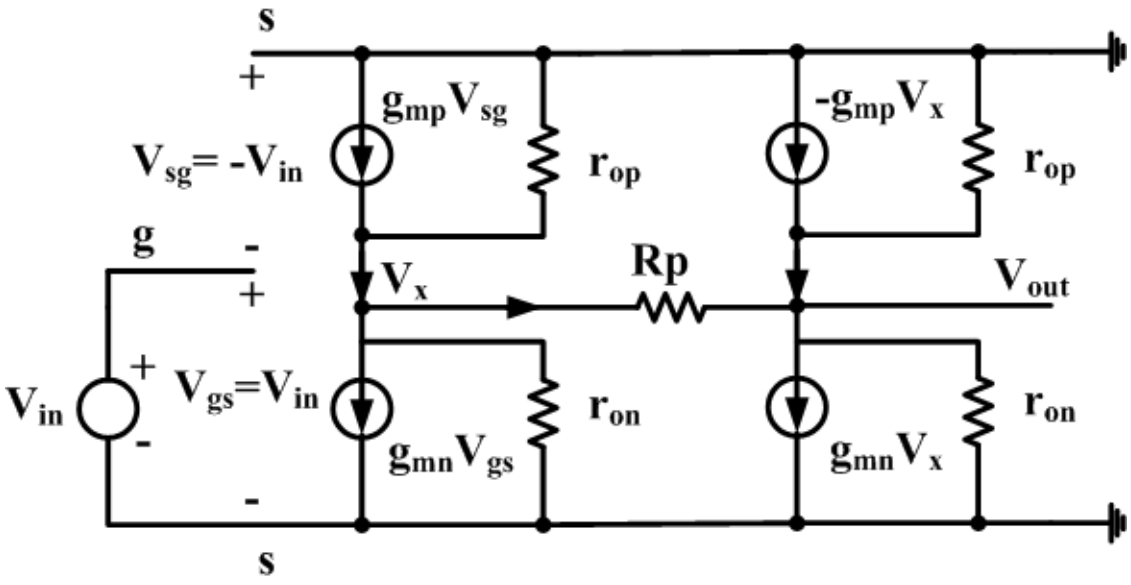


Figure 5-11: Small-signal model of the open loop circuit.

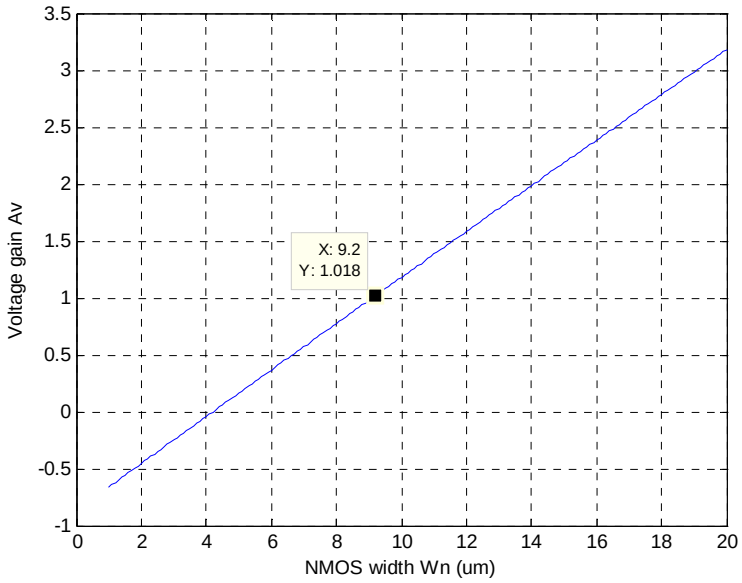


Figure 5-12: Sweep simulation of voltage gain versus NMOS gate width.

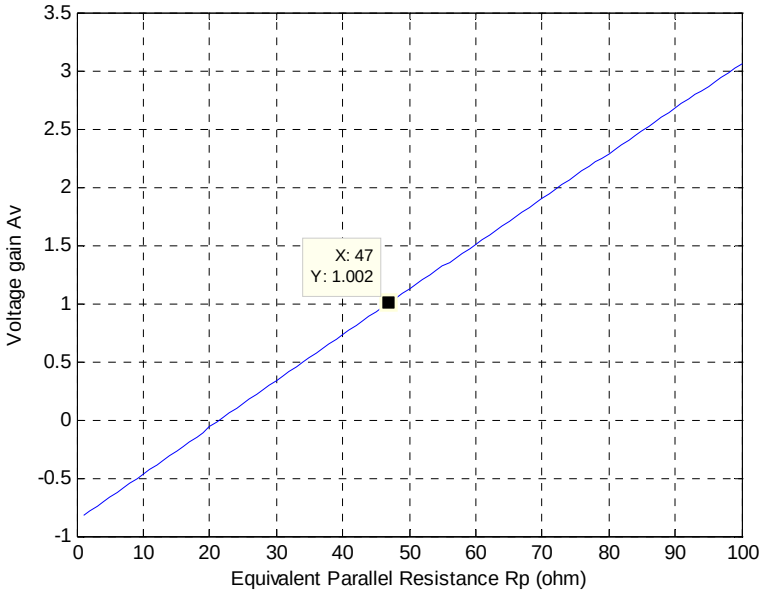


Figure 5-13: Sweep simulation of voltage gain versus Equivalent Parallel Resistance.

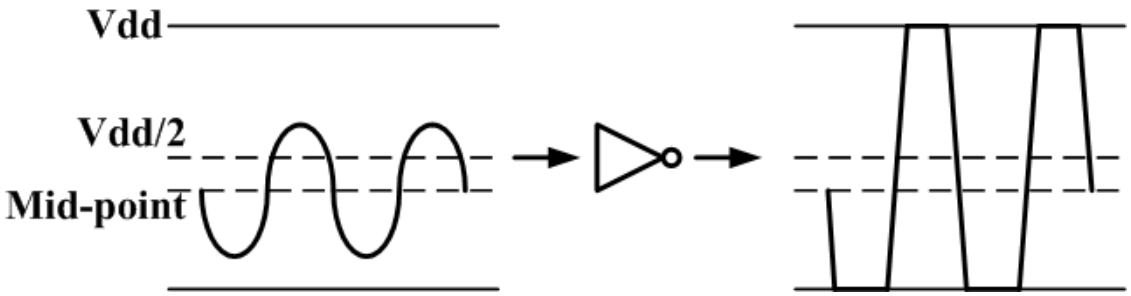


Figure 5-14: Midpoint biased sinusoid wave propagates through inverters.

## 5.5 Cadence Simulation Results

To determine the feasibility of the LC oscillator design, a transient simulation based on the simulator Spectre in Cadence ADE is performed. The phase noise and jitter measurement can then be plotted and analyzed.

### 5.5.1. Transient Simulation

All components of the LC oscillator circuit are defined, except capacitor $C$ in the LC tank. Its value is adjustable for controlling oscillation frequency, based on the following expression.

$$\omega_0 = \sqrt{\frac{L - C_{total} R_L^{\ 2}}{L^2 C_{total}}} \qquad where\ C_{total} = C + C_{mosfet} \tag{5-22}$$

where $C_{total}$ is the total effective capacitance in the circuit, including the designed capacitor $C$ and the parasitic capacitance from the cross-coupled transistors $C_{mosfet}$. From the simulations, $C$ is assigned a value of 2 pF to generate an oscillation signal of 800.5 MHz. Simulation plots from the final design are shown in Figure 5-15. The red curve represents the waveform at point $A$ in Figure 5-1, and the blue curve is the output square wave at point $B$.

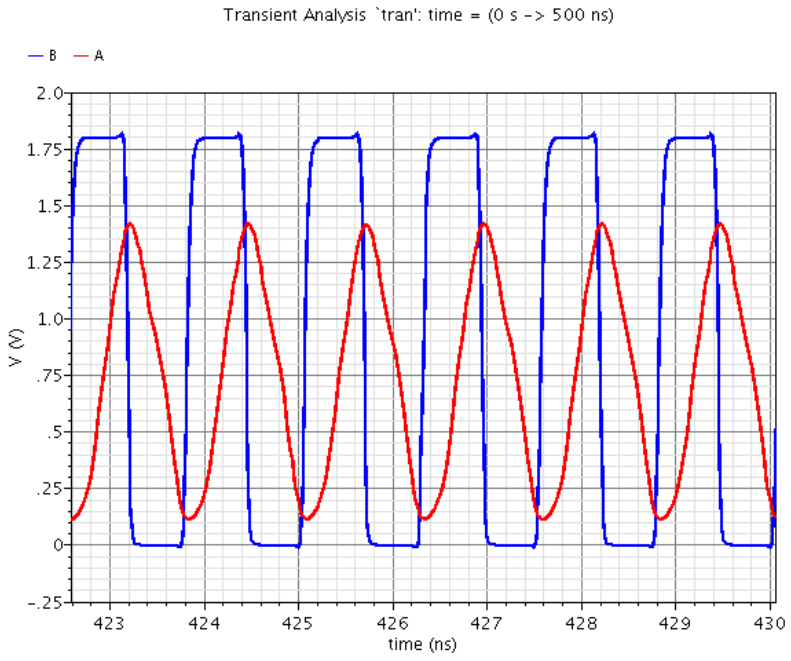


Figure 5-15: Simulation plots of the final design of the LC oscillator.

### 5.5.2. Phase Noise and Jitter Measurement

Noise in the circuits is unavoidable. It causes random phase shifts to the desired oscillation signal, which is so called phase noise. The power spectral density (PSD) of a general oscillation signal $S_c(f)$ is shown in Figure 5-16. $f_c$ is the center frequency. At point $f$ after a frequency offset, PSD drops since noise power is always less than signal power. Hence, the phase noise spectrum (PNS) $L(f)$ can be defined as the ratio of PSD at a specified frequency offset to PSD at the center frequency, as shown in expression (5-23) [43].

$$L(f - f_C) = 10\log\left[S_C(f) / S_C(f_C)\right] \qquad (in\ dBc/Hz) \tag{5-23}$$

Based on the proposed LC oscillator design, PNS, relative to the 1st harmonic of the signal at the point $B$ (Figure 5-15), is plotted in Figure 5-17. PNS at the frequency offset of 1 kHz is -17 dBc/Hz, and it drops to -145 dBc/Hz at 400 MHz, which is half the oscillation frequency. That is, noise power degrades exponentially with the frequency offset. This occurs because the noise components in the circuits mainly include thermal noise and flicker noise. Basically, all electronic devices generate these two types of noise. Thermal noise comes from the device heat caused by dissipating power. It is a type of white noise, and it distributes the same power at all frequencies. Flicker noise is also called 1/f noise or pink noise. It is dominant at a very low frequency and is overshadowed by white noise at a high frequency as its power is inversely proportional to the frequency. However, partial power of the flicker noise can be carried to high frequencies near the carrier, which is the oscillation frequency, and mixed with thermal noise, which results in a higher noise power at low frequency offset. Note that in the plot, PNS exceeds zero at low frequency offset, which is non-physical. This value is due to the invalidation of the data at low frequency offsets. Noise analysis in the simulator, Cadence SpectreRF, is based on a small signal model compared to the size of the carrier. At low frequency offsets, the real noise power is close to the carrier power; therefore, the relative noise signal is a large signal. Hence, small signal analysis breaks down and returns non-physical results. This method is consistent with using the small signal model to calculate

the noise, which would result in an unbound phase noise spectrum at low frequency offsets.

Since the oscillation signal is sent to a digital frequency counter, the process is based on the timing behavior of the signal. Performance of the phase noise in the time domain is the jitter on the rising and falling edges of the signal. The root mean square (RMS) of the period jitter of a single cycle is 12.72 fs, or 10.2 PPM for the 800 MHz signal (shown in Figure 5-17). This calculation gives a 8 kHz frequency shift if all cycles have the same RMS jitter. It is large compared to the frequency shift caused by an iron nanoparticle tagged microorganism, which means the sensitivity of the biosensor is significantly restricted. However, the jitter occurs on both sides of the timing edge, and RMS jitter is an absolute value. Hence, the long-term jitter of a period has multiple cycles and cannot simply be defined as the RMS jitter of a single cycle. Generally, the jitter of an oscillation signal is a random jitter and has a Gaussian distribution and zero mean. Therefore, in the longer period the oscillation signal is sampled for counting the frequency, the PPM of the long-term jitter is smaller and converges to zero. Therefore, the time interval of the sampling signal should be as long as a few seconds (discussed in Chapter 6).

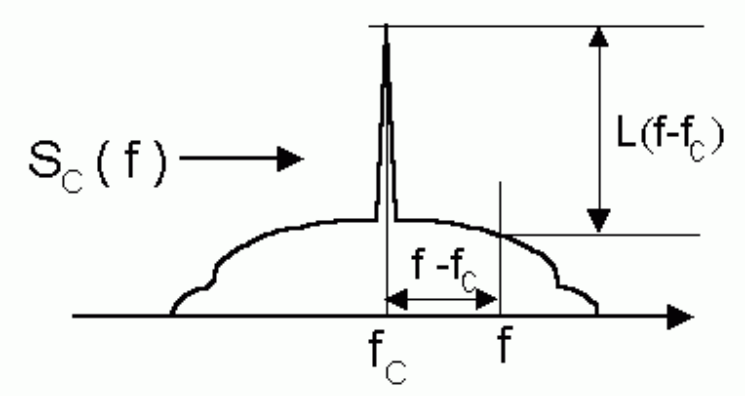


Figure 5-16: Power spectrum density of an oscillation signal [43] "Clock (CLK) Jitter and Phase Noise Conversion", Application Note 3359, *Maxim Integrated*, used under fair use, 2014.

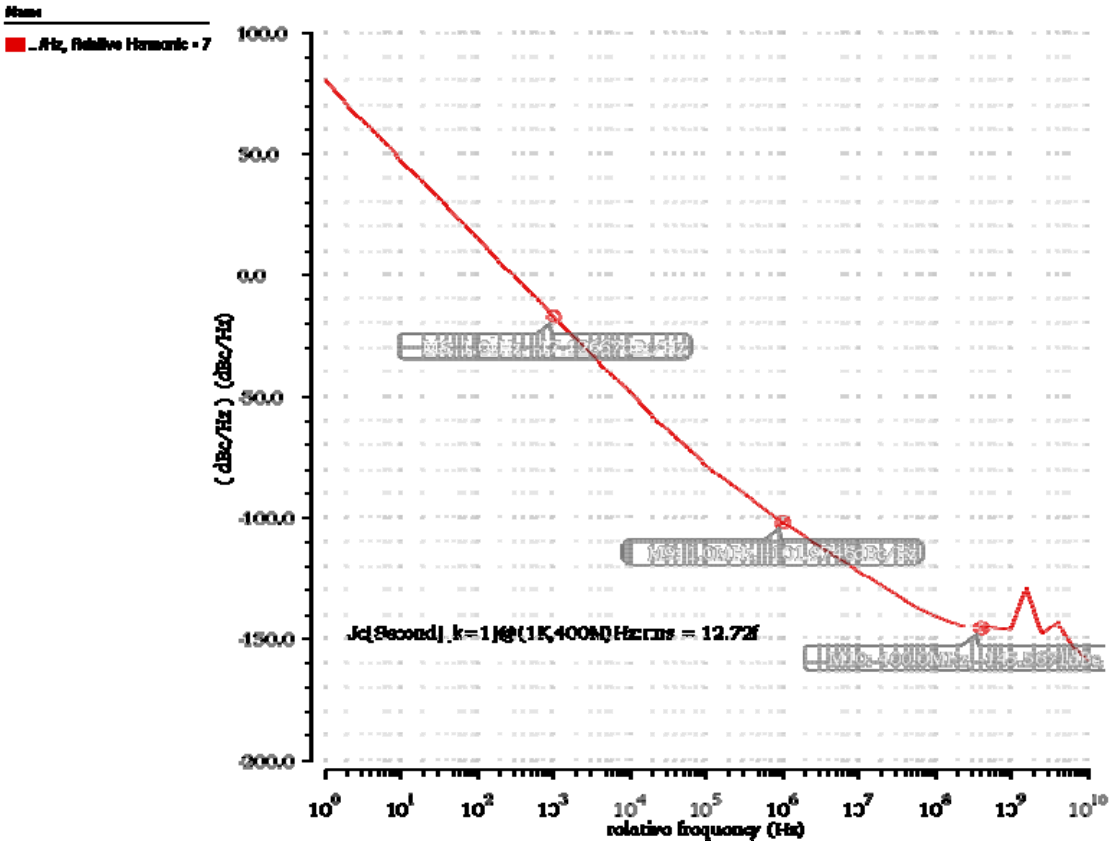


Figure 5-17: Simulation plots of the final design of the LC oscillator.

## 5.6 Summary

In this chapter, the detailed design process of the LC oscillator circuit is detailed. Based on extracted inductance and resistance from two electromagnetic simulation software programs, a cross-coupled oscillator with 10 transistors is constructed. The final simulated design of the LC oscillator gives a square wave signal with the frequency of 800.5 MHz. This signal carrying the sensed information is then sent to the rest of the digital circuits for data processing.

# Chapter 6: Digital Circuits: Frequency Counter and Timing Controller

## 6.1 Introduction

This chapter discusses the designs of the digital circuit blocks on the chip, that is, the frequency counter and the timing controller. The frequency counter calculates the frequency of the oscillation signal from the LC oscillator and stores the result. To make the circuit logic operate correctly, two control signals are generated from the timing controller block. The sensor system architecture in Figure 6-1 shows how function blocks operate with the signals. The AND gate is used to sample the oscillation signal. Although the timing controller circuit is not used in this prototype system, its design concept and diagram is considered in a later section.

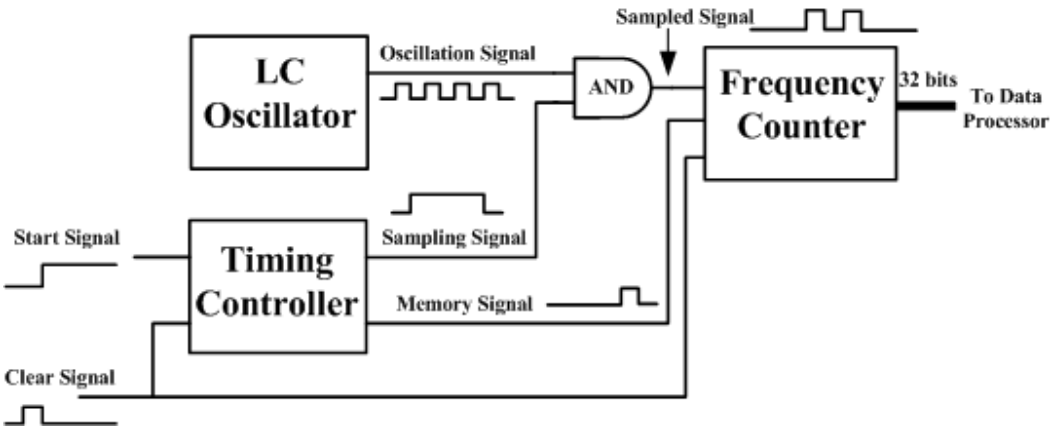


Figure 6-1: Sensor system architecture.

## 6.2 Frequency Counter

The frequency counting concept deals with the square wave oscillation signal output from the LC oscillator that is sampled for a certain time period. Then the number of square pulses in this sampled signal is counted by a digital counter circuit. Therefore, the counted number divided by the sampling time is the signal frequency. Since this division or other further calculations are processed in the data processor, as discussed in the system diagram of Figure 2-1, the frequency counter circuit also includes memory to store the counting result.

### 6.2.1. Circuit Schematic

The digital counter designs have two topologies of (1) synchronous and (2) asynchronous and most designs are based on the toggling function of JK flip-flop (JKFF). When both control inputs *J* and *K* stay at logic one, the status of the output signal *Q* is toggled at every falling edge of the clock. If multiple JKFFs are cascaded so that every JKFF toggling action is controlled by the previous one, a multi-bits counter that counts the number of the clock falling edge can be developed.

Figure 6-2 shows the circuit schematic of the digital frequency counter used in this project. If the density of biologicals is low in the sensor and causes a tiny change to the frequency, the counter must be set to high resolution, which requires a large value for the maximum counting number. For instance, to detect a change in Parts Per Million (PPM), the counter must count at least 1 million to reach a difference of 1. According to simulation results shown in Figure 4-7, due to the extremely tiny size, one iron nanoparticle could only make a frequency shift of less than 1 Hz with the oscillation frequency of 800 MHz. Although the sensing unit is one biological pathogen that should carry many more particles, design tolerance necessitates designing a counter for Parts Per Billion (PPB). Therefore, the maximum interval of the sampling signal is up to 4 seconds for counting a maximum frequency of 1 GHz, which yields a maximum counting number

of $4\times10^9$, requiring 32 binary bits. Hence, 32 JKFFs are needed. Note in the schematic that *J* and *K* inputs of all JKFFs are removed as they are permanently set to the logic one, and the output *Q* of the JKFF connects to the clock input of the next one. Hence, this design is an asynchronous counter, since the current bit is generated from only one bit ahead and the propagation delay is accumulated from every stage. Although the asynchronization of this counter does not fit with most timing logics with a fast clock, it is not an issue for this design because only the final counted number is essential data. As an illustration, Figure 6-3 represents an example of counting 6 from a 3-bit asynchronous counter. The sampled signal that consists of 6 square pulses propagates through the three cascaded JKFFs. Even though the propagation delay is introduced from JKFFs, the counting result is correct as long as all outputs fix at their final status.

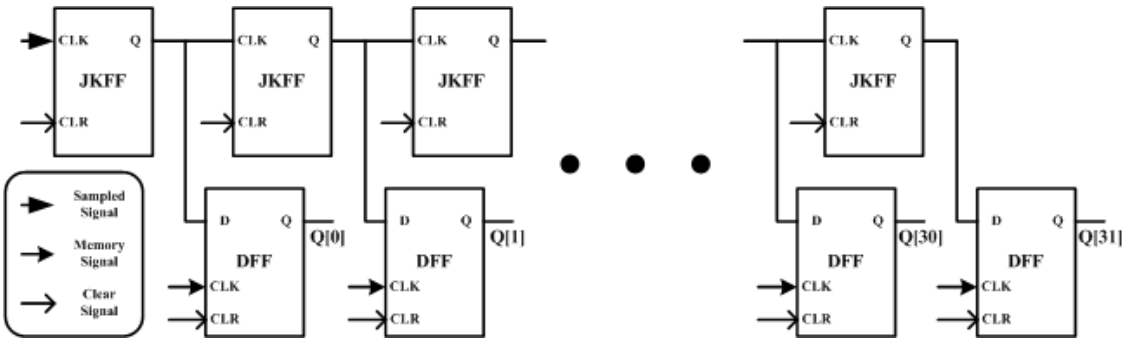


Figure 6-2: Circuit schematic of the frequency counter.

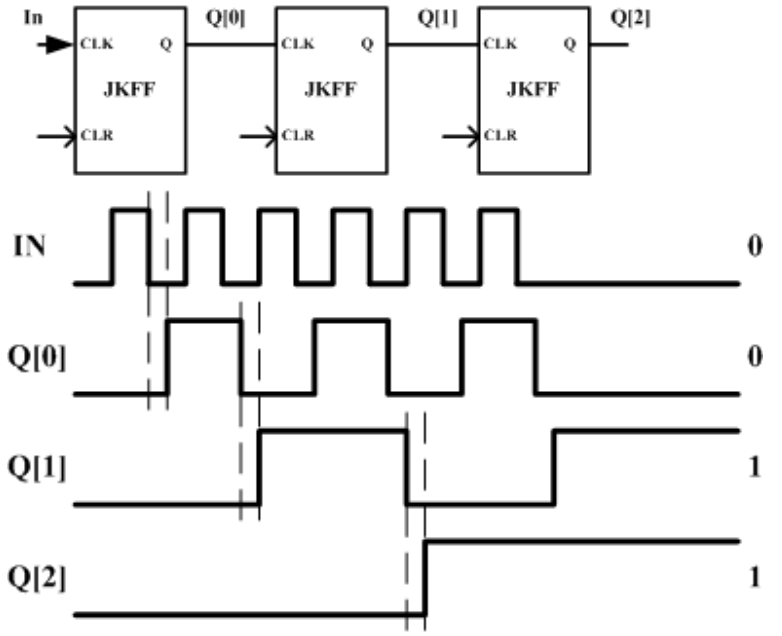


Figure 6-3: Example of 3- bit asynchronous counter.

Data from the frequency counter, that is, the counting result, is stored in the memory. Hence, every JKFF output is followed by a standard D flip-flop (DFF) trigging with rising edges of the clock. In one counting operation, one rising edge or one square pulse is needed for the clock signal of the 32-bit DFF to store the result and hold it as long as needed. Moreover, to guarantee storing the correct counting result, there must be a time interval between the last falling edge of the sampled signal and the rising edge of the memory clock. This interval needs to be long enough to cover the maximum propagation delay of the counter, including accumulation of the delays from 32 JKFFs plus one DFF. On the other hand, all JKFFs and DFFs have an input of "Clear" for resetting their outputs to logic zero before the count begins. The time interval between the clear signal and the sampled signal is not restricted, since the clear function is instantly disabled when the signal falls to logic zero. Hence, the three input signals of the frequency counter have a timing relationship as illustrated in Figure 6-4.

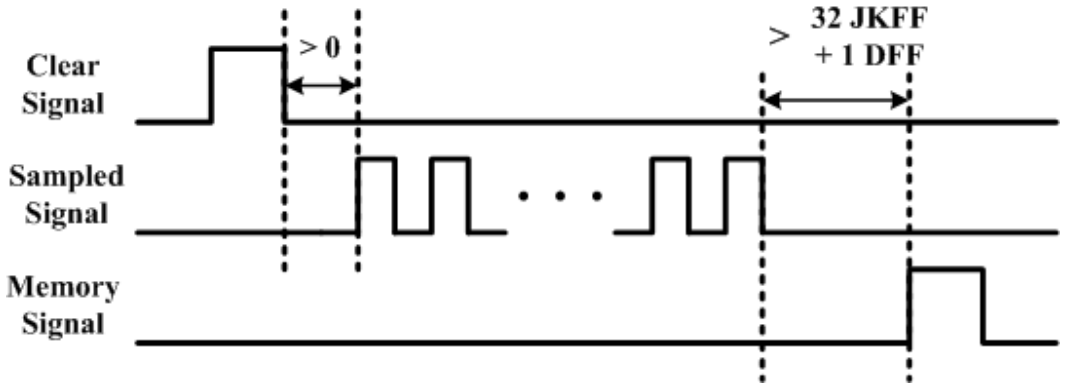


Figure 6-4: Timing relationship of the three input signals.

### 6.2.2. Cadence Layout Simulation

To accurately simulate the digital circuit with a high frequency near 1 GHz, the parasitic from routing traces, substrate, and their coupling is modeled from the circuit layout. Thus, according to the circuit schematic, the layout of the frequency counter is developed in the CAD tool Cadence Virtuoso. As shown in Figure 6-5, this layout requires an area of 720μm by 700μm, containing about 640 NAND gates, or over 2500 transistors. For a short propagation delay from each gate, transistor widths are set as $W_{PMOS}/W_{NMOS}$ = 23 μm/14 μm, while the length is constantly 0.18μm, which yields a relatively short propagation delay of 56 ps. Hence, for a standard master-slave structure of the JKFF or DFF, the propagation delay is the summation of three stages of the NAND gates, which is about 0.2 ns. The parasitic model abstraction of the layout is constructed by the Cadence build-in tool, Assura. The extracted circuit, as an accurate model of the layout, is then connected to the LC oscillator circuit for the simulation with an AND gate (Figure 6-1).

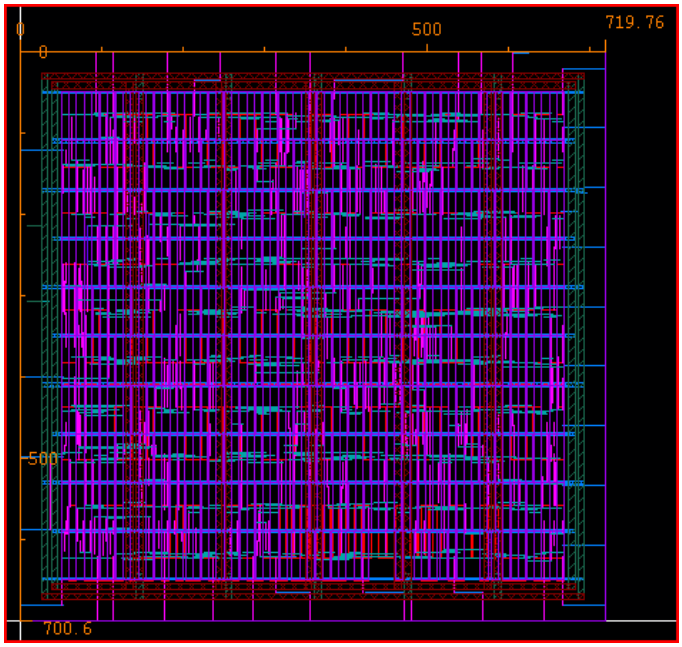


Figure 6-5: Cadence layout of the frequency counter.

Figure 6-6 plots the counting result of the first simulation. Due to the large number of components, including models of the transistors and the extracted parasitic elements, involved in the analysis, the huge amount of calculations significantly slow down the simulation process. Available computer power is able to simulate only a few hundred of nanoseconds in one day for transient analysis. Therefore, the correct counting function with a small number of digits must first be verified; a short sampling signal with the pulse width of 100 ns is used to sample the oscillation signal. From the plots of the 7 bits, $Q$[6] to $Q$[0], the counted number is 101000 in binary and 80 in decimal, which would return a calculated frequency of 800 MHz. This result approximately matches simulations of the LC oscillator in Chapter 5 with an error of 0.5 MHz since the small amount of sampled cycles limit counter resolution.

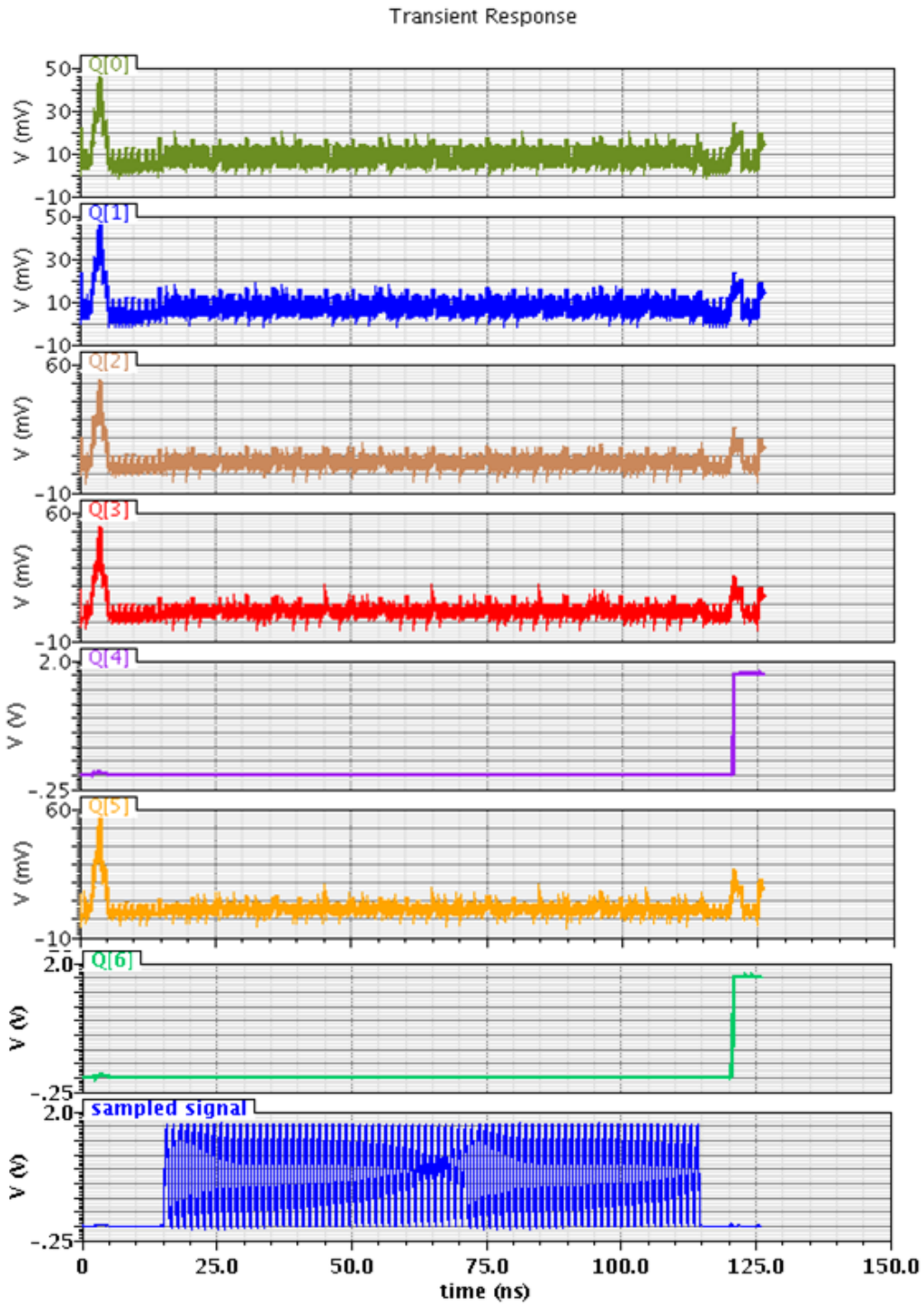


Figure 6-6: First transient simulation result of counting the frequency.

Although the computer does not support a long enough period of the transient analysis to test the counting function for the rest of the 25 bits, it is still feasible to verify the proper toggling action of the corresponding 25 JKFFs. In the second simulation, the clear signal is disabled by staying at logic zero, and the initial status of the counter output is set at a binary number 011...1 (31 bits of "1"). Then the input pulse in the sampled signal toggles all 32 outputs of the JKFFs at once and correctly turns the number to 100...0 (31 bits of "0"), as illustrated by the most significant 6 digits in Figure 6-7.

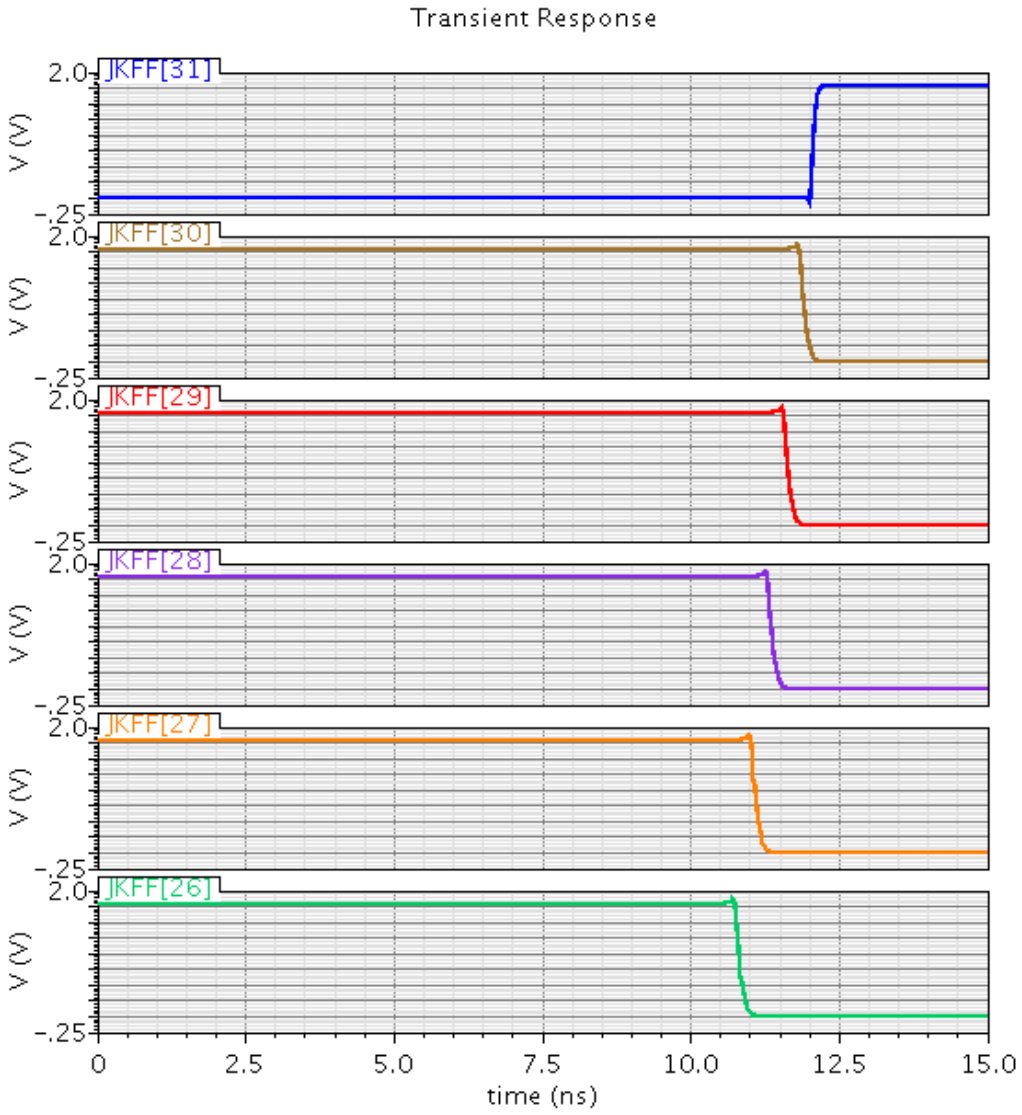


Figure 6-7: Second transient simulation result of checking JKFFs.

## 6.3 Timing Controller

As shown in Figure 6-1 and discussed in the above section, two signals, the sampling signal and the memory signal, are needed for the system to work properly. Both signals are generated by the digital circuit block, the timing controller; Figure 6-8 depicts its circuit diagram. The clear signal, used to reset all flip-flops in both the frequency counter and the timing controller, is designed as an input from the user interface, for instance, a click button. In the same way, the start signal is also sent by the user to control the time when the sensor system starts. Once the start signal stays at logic one, the clock source starts to transfer an accurate and stable clock signal of 10 MHz to a digital counter. Note that 10 MHz is a standard frequency for a commercial clock source. Unlike the frequency counter that only outputs a value, this counter must be a synchronous design for generating timing sensitive signals. The design of the synchronous counter based on JKFFs is shown in Figure 6-9. To generate a sampling signal with a maximum pulse interval of 4 seconds and a memory signal, the time line of the counter is set at up to 5 seconds. Therefore, with a 10 MHz clock, the maximum counted number is $5\times10^6$, which requires 23 binary bits. For checking design feasibility, the result is that the worst propagation delay for this counter is the accumulation of 21 AND gates plus a JKFF. The delay of one AND gate can be estimated by 2 NAND gates, which is 0.12 ns. Hence, the delay of the counter is calculated as about 2.7 ns, and it is much shorter than the clock period of 100 ns. The circuit following the synchronous counter is tracking the counted number. As illustrated in Figure 6-8, the positive pulse only occurs when the counted number equals *A*, *B*, *C*, or *D*. By combining the pulses of *A* and *B* and using their falling edges to toggle the JKFF output, a pulse is formed and its interval calculation is obtained from the following expression.

$$T_{\mathrm{int}erval} = (B - A) \times T_{CLK} + J \tag{6-1}$$

where $T_{CLK}$ is the clock period and *J* is the total signal jitter. This jitter includes the clock jitter, the random jitter from the propagation delays of the tracking blocks, OR gate, and JKFF. To minimize the jitter, a DFF trigging by the 10 MHz clock is used to reset the

propagation delay. Therefore, the jitter of the final generated sampling signal only contains the clock jitter plus the random jitter from the propagation delay of DFF. Since the delay of a DFF is only around 0.2 ns, the jitter from this part is minimal and can be ignored. Thus, the jitter of the sampling signal could be evaluated from the jitter of the clock source. Recall from the simulations that one iron nanoparticle can only make a frequency shift of less than 1 Hz with the oscillation frequency of 800.5 MHz. This means, if the clock jitter is more than 1.25 ns in 1 second, the random jitter in the sampling signal will be large enough to overshadow detection of the frequency change caused by the single particle. Therefore, if the sensing unit is one particle, the timing accuracy of the clock source must be in the level of PPB, or called rubidium time-base. Since this project is focusing on detecting biological pathogens, the specification of clock accuracy could be determined after determining the changing ratio from the organisms in a certain number of biological experiments. Moreover, tracking blocks *C* and *D* generate the memory signal and do not require strict timing accuracy as the sampling signal does. From the time relationship of these two signals discussed in Section 6.2.1, then the relationship of *A*, *B*, *C*, *D* values is $A < B < C < D$.

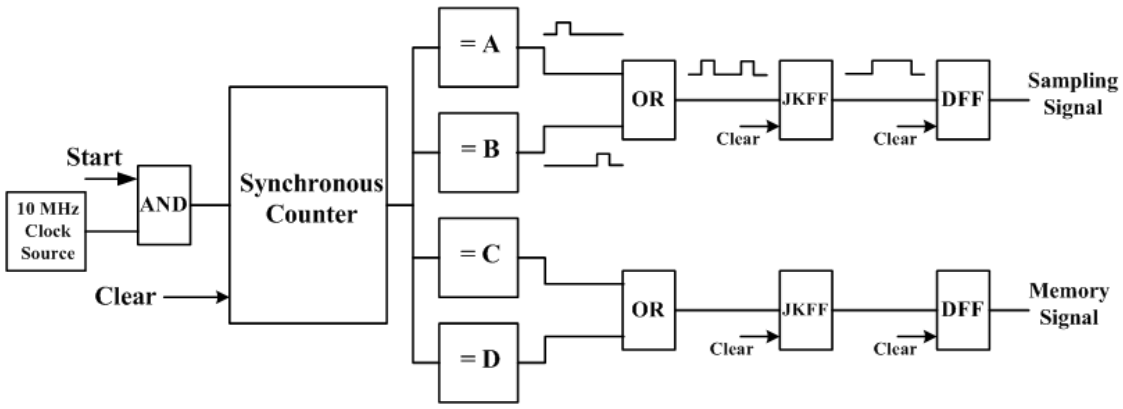


Figure 6-8: Circuit diagram of the timing controller.

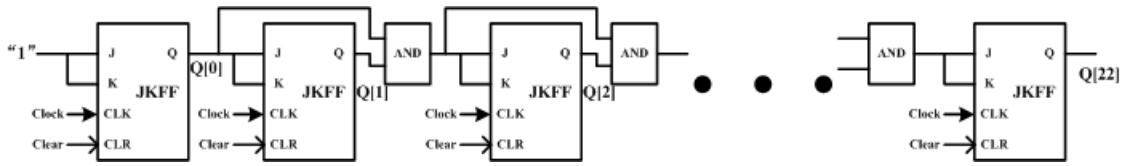

Figure 6-9: Circuit schematic of the synchronous counter.

## 6.4 Summary

In this chapter, the designs of two digital circuit blocks are presented. The 32-bit frequency counter counts the frequency of the oscillation signal with a sampling signal and a memory signal. The Cadence layout simulation verifies its feasibility. Both the sampling signal and the memory signal are generated in the timing controller block. Although its circuit design is discussed, due to the limit of design budget, this circuit block is not integrated in the prototype chip. Instead, generation of the two timing signals is from a commercial function generator for the prototype system, which will be introduced in a later chapter.

# Chapter 7: BASIC Prototype System

## 7.1 Introduction

Previous chapters discuss design details of all components in this biological sensor system. To test the system feasibility in the real world, a prototype system is needed for the physical experiments. This chapter presents the development of the prototype sensor system. In the following sections, procedures for IC chip fabrication, PC board design, and other instruments used in the test bench are presented. A test result records the failure of the chip due to damage in the manufacturing process. The analysis and solution are then discussed.

## 7.2 Chip Layout and Fabrication

Since the circuit of the timing controller is not integrated, this prototype chip consists of the sensor head, which is a conical-shaped inductor, the LC oscillator, and the frequency counter. As stated previously, the chip layout is drawn in the CAD software Cadence Virtuoso. Figure 7-1 shows the complete layout of the prototype chip. As noted previously, this chip design is based on the 180 nm technology IBM_CMOS_7RF, supported by the integrated circuits foundry service MOSIS. MOSIS Educational Program (MEP) offers fabrication services for academic research and instruction [44]. The whole chip, where the edge is the ionic contamination guard ring, is 1.5 mm × 1.5 mm, which is the maximum allowable size in MEP (called TinyChip). The massive circuit in the center area is the digital frequency counter (shown in Figure 6-5). The

conical-shaped inductor coils, together with the capacitor and the rest transistors of the LC oscillator, are located in the upper-left corner. Squares surrounding the counter circuit are the bond pads with the size of 68 μm × 68 μm and pitch of 80 μm. These 38 bond pads act as the chip input / output pins. 32 of these pads, 30 on the top, right, bottom sides and 2 on the lower-left side, are the outputs of the 32-bit frequency counter. The left 6 pads from top to bottom are the output from the oscillator for the chip test--the sampling signal, 1.8 V power supply, the ground, the memory signal, and the clear signal. Some extra details about the layout design and fabrication are introduced in the following sub-sections.

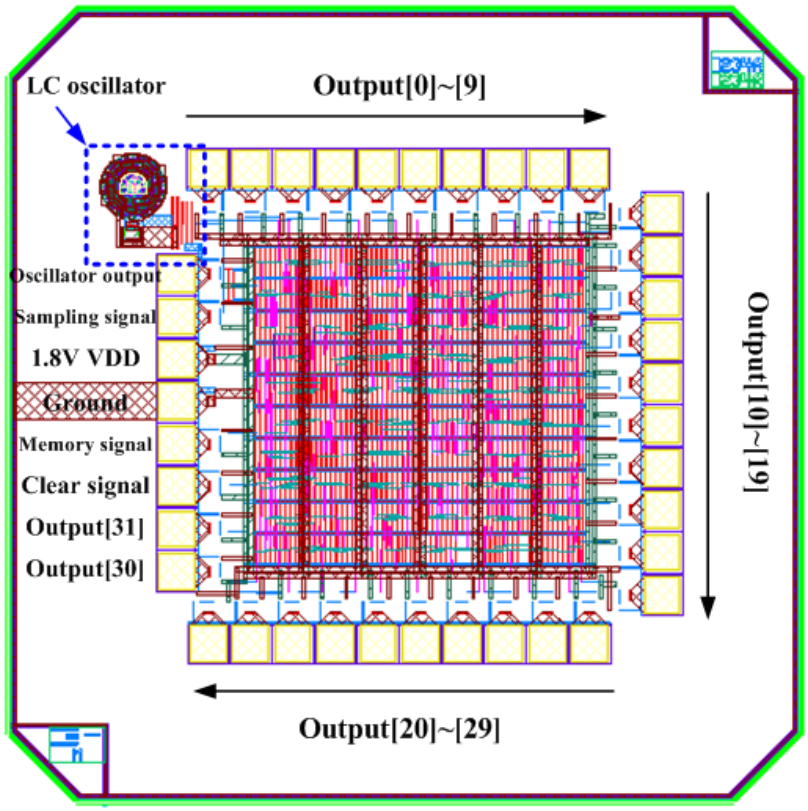


Figure 7-1: Full layout of the prototype chip.

### 7.2.1. Input/output Pads with ESD Protection

To protect the chip from burning out from sudden large voltage/current spikes caused by Electrostatic Discharge (ESD), adjacent to the pads are protection circuits. As illustrated in the circuit schematic of the input pad in Figure 7-2, a pair of diodes connect the input pin to VDD and Ground. In case voltage out of the range of Ground to VDD approaches the pad, one diode turns on to sink the extra current and limit the voltage level to the safe range. A second protection comes from the two cascaded inverters behind the diodes. The gate oxide of the transistors in this technology can tolerate a high voltage of up to 5.2V [35]. Moreover, the output voltage level of the transistors is controlled by VDD, which makes them perform like voltage translators to draw the high voltage back to VDD. The design widths of the first inverter are $W_{PMOS}/W_{NMOS}$ = 50 μm/30 μm and 200 μm/120 μm for the second one. The large size of the second inverter is able to handle large capacitive load from the fan-out structure. For instance, all JKFFs and DFFs in this chip receive input from the clear signal, which yields a relatively big gate capacitance from hundreds of transistors. To quickly charge this capacitance and maintain the propagated waveform, transistors must have large transistor widths. Figure 7-3 shows the layout of this input pad circuit. The structure of the output pad is very similar to the input pad (Figure 7-4). Note that the parameters of the output pad circuit are the same as the ones of the input pad. The large transistor is still necessary to drive the capacitance out of the chip. Nevertheless, the protection circuits in the input/output pads rely on the reference voltages of VDD and Ground that come from the power pads. However, there are no other reference voltages to protect VDD and Ground. Thus, the two power pads of VDD and Ground are not protected in the chip design. Protection for them is generally considered in the PC Board design.

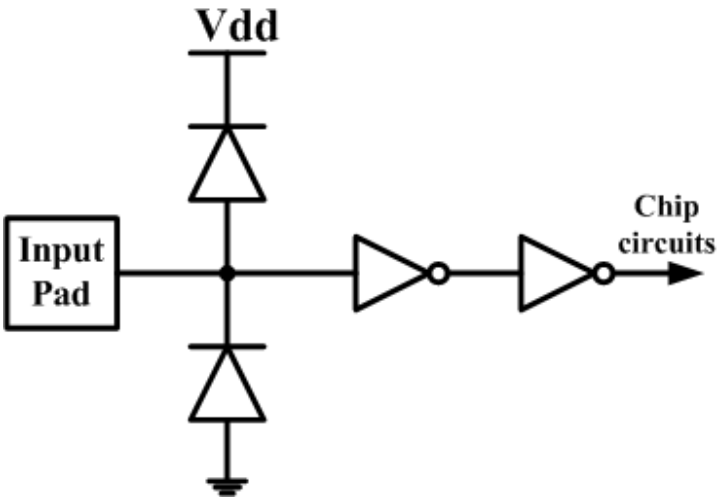


Figure 7-2: The circuit schematic of the input pad.

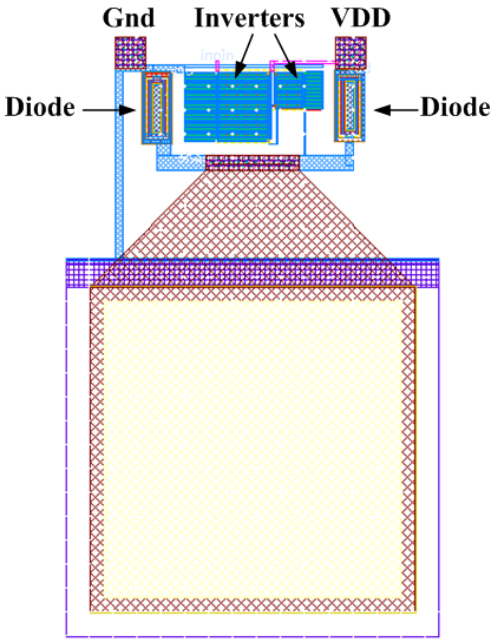


Figure 7-3: The circuit layout of the input pad.

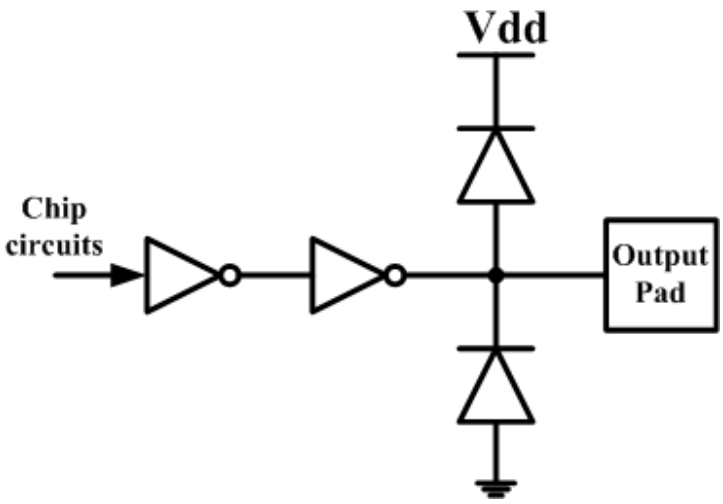


Figure 7-4: The circuit schematic of the output pad.

### 7.2.2. Algorithm of Creating the Layout for the Conical-shaped Inductor

As discussed in Chapter 3, the design of the conical-shaped inductor is composed of traces in the shape of a circular donut. However, a perfect circle cannot be fabricated using the design of the layout. In the grid-based layout of the technology IBM_CMOS_7RF, all vertexes of any shape must be located at the corner of a minimum sized grid, and their boundaries must follow the sideline or diagonal of the grid [35]. Therefore, any pair of intersecting lines in the layout cannot have an angle other than a multiple of 45 degrees. One way to draw a quasi-circle is to find a grid-based locus as close to the circle edge as possible. Hence, the drawing algorithm dictates that the target circle edge is determined by the position of its center point and its radius. Using the coordinates of a starting point, the moving direction is defined as where the next point must be located for a legal locus. Figure 7-5 numbers the eight direction options. Moving in any one of the directions guarantees an angle of 45× degrees. The eight candidate points can be located by one unit distance of the side or diagonal length of the minimum sized grid. In the algorithm, using the initial moving direction and keeping the locus smooth, the possible moving directions are limited to neighboring ones. For instance, if

the given direction number is 0, the possible directions will be 7, 0, and 1. This restriction avoids the appearance of sharp angles in the shape that may violate the design rule. To decide which one of the three candidate points is closest to the actual radius, their distances to the circle center are compared. Figure 7-6 describes the pseudo-code of this algorithm for creating a quasi circle shape by using Cadence specific programming language SKILL. Note that, if the start point and end point are the same, a full circle will be drawn; a sector will be drawn if the two points are different. If the algorithm is increased, a circular donut with a certain width is obtained by drawing two concentric circles with a gap that defines their start and end points. Figure 7-7 is an enlarged picture of the LC oscillator layout from Figure 7-1. Zooming in on the edge of the inductor coil shows the jaggy boundary of how this conical-shape inductor is designed on the grid.

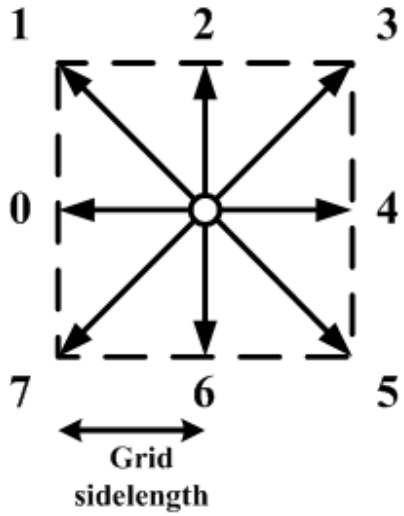


Figure 7-5: Definition of moving directions.

*01. set coordinates and initial moving direction of the start point*
*02. set coordinates and initial moving direction of the end point*
*03. motion function (start point: coordinates and direction)*
*04. locate three candidate points at and near the current direction (0, +45, -45 degree)*
*05. calculate the distances between the candidates and the circle center*
*06. compare the distances with the circle radius*
*07. the smallest difference decides the movement*
*08. replace the next point as the current point (update coordinates and direction)*

*09. end motion function*
*10. add the coordinates of the current point to the coordinate list*
*11. while (the distance between the current point and the end point is larger than the grid size)*
*12. motion function (current point)*
*13. add the coordinates of the current point to the coordinate list*
*14. end while*
*15. add the coordinates of the end point to the coordinate list*
*16. add the coordinates of the circle center to the coordinate list*
*17. use the coordinate list to draw the polygon*

Figure 7-6: SKILL pseudo-code for creating a quasi circle.

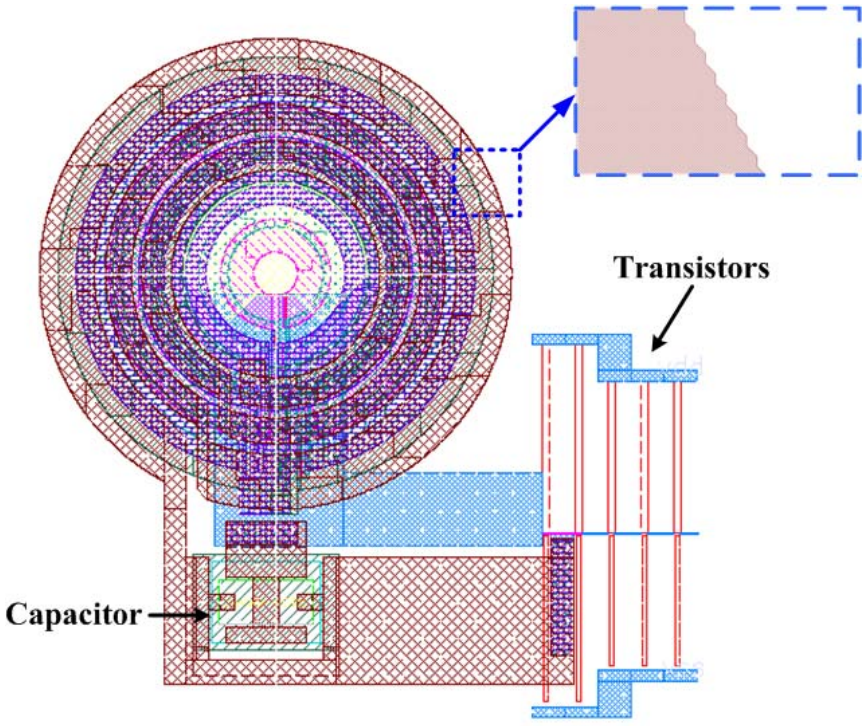


Figure 7-7: The circuit layout of the LC oscillator.

### 7.2.3. Observation of the Fabricated Chips

The final layout design of the BASIC chip is sent to MOSIS for fabrication. Figure 7-8 shows the returned chips with QFN 40 pins packaging (OCP_QFN_6X6_40A), including

the top view, the top view without the lid, and the bottom view. Figure 7-9 is a picture of the chip surface under a digital microscope and shows the traces on the top metal layer.

Recall that, in the description of Chapter 3, Section 3.4, the bottom of the sample container is a circle with the section closed to the coil junctions being excised. The sample container with this shape is designed as a passivation opening in the layout. It is the same opening used in the bond pads, except that the top layer metal is not its base. In the manufacturing process, the passivation opening is produced by specific chemistry etching and generally stops at the metal surface. Without the top layer metal, the etching continues to dig into the silicon dioxide and stops at an unknown depth. Therefore, a measurement of the inductor surface to determine the shape of the sample container is needed. With assistance of the Zygo digital microscope, the surface profile measurement of the conical-shaped inductor is taken (shown in Figure 7-10). Due to the complexity of the inductor geometry, the measurement is not precise. However, the measurement still indicates that the distance between the surface of the top metal layer and the sample container bottom is around 8.5 to 8.6 μm. Including the thickness of the biological, the depth of the sensing plane would be approximately 8 to 8.1 μm, which is very near the altitude of the surface of the second top metal layer. Recall from Figure 3-8 that the sensing plane giving the most uniformity to the magnetic field is located 2 μm above the second top metal layer. Hence, field uniformity of the sensing plane in the fabricated chips is worse. Figure 7-11 shows the 3D field plot of this plane from the Maxwell simulation. The worst field deviation is as large as 11% and yields 23% deviation of inductance change, which will degrade sensing accuracy. To relocate the sensing plane for better system performance will require post-processing.

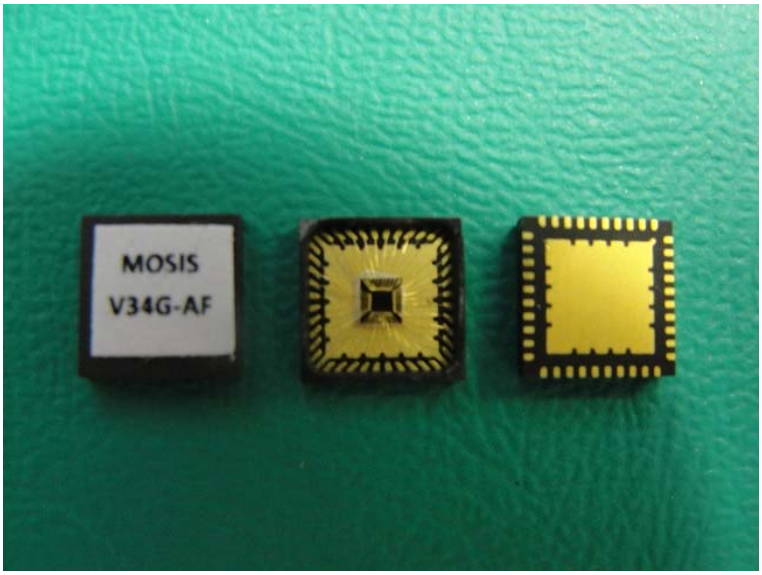


Figure 7-8: The fabricated BASIC chips with QFN packaging.

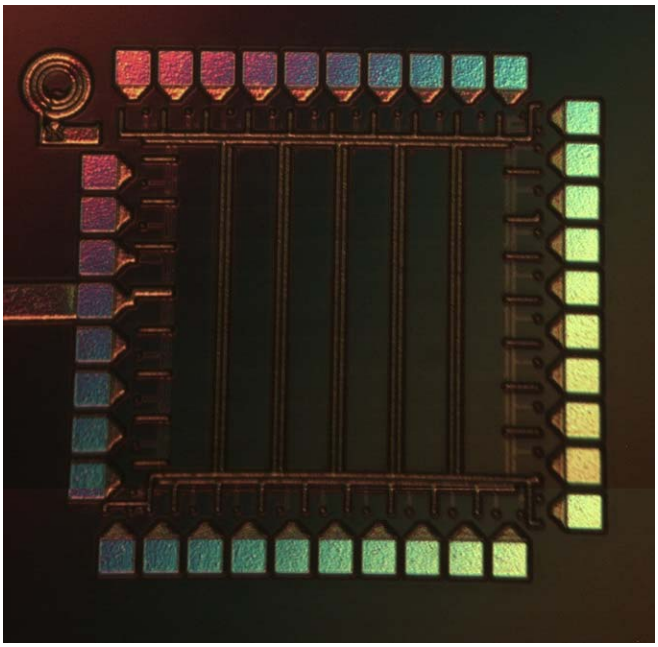

Figure 7-9: The chip surface under a digital microscope.

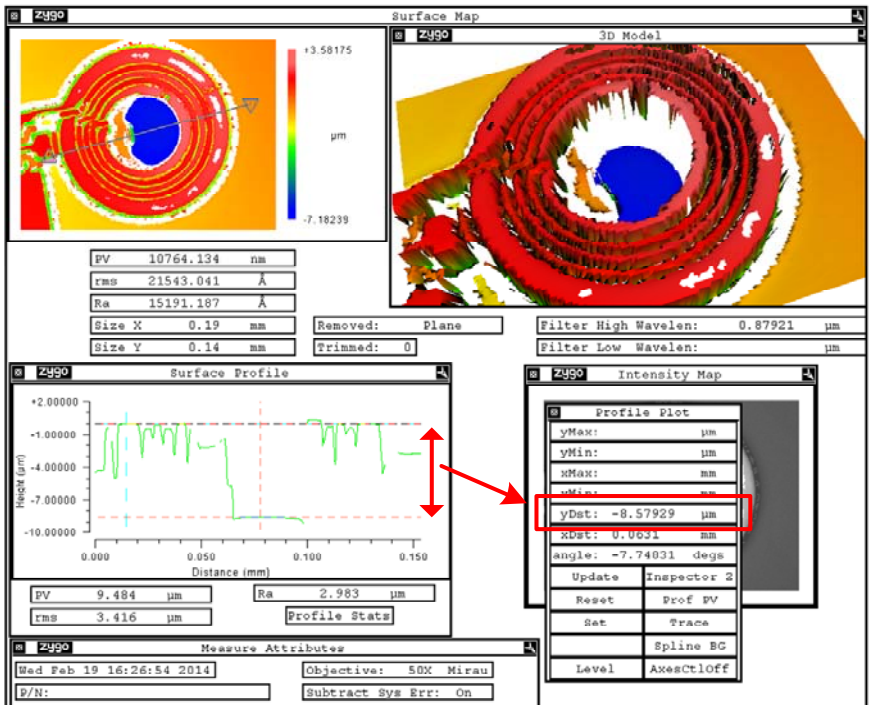


Figure 7-10: Inductor surface profile measurement.

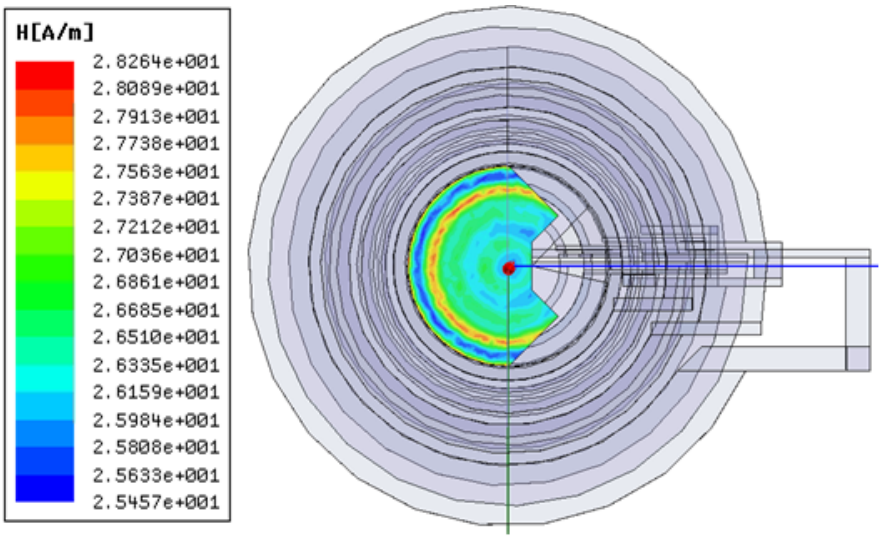


Figure 7-11: 3D field plot of the sensing plane with the vertical offset.

## 7.3 PC Board Design

For the sensor chip to operate electrically on the test bench, the PC board acts as the chip carrier and provides connections between the pins of the chip and off-chip components. As described in previous sections, the prototype chip has 36 input/output signals, and their use must be identified as the first step of the design.

The output signal from the LC oscillator has a high frequency of 800.5 MHz; consequently, it is sent to an RF spectrum analyzer or a commercial frequency counter with RF bandwidth. Generally, these precision instruments have a power damage level of +30 dBm and a sensitivity of less than 0 dBm at RF. Therefore, to avoid any potential damage to the instruments, the output power level must be precisely limited. The input port on most of these instruments has 50 Ω impedance. The power supply of the chip should have a stable voltage level of 1.8 V. The board design uses a 450 Ω resistor in series for this output trace and restricts the output level to 0.18 V at the SMA cable connector. Hence, the input power of the instruments will be 0.000648 W or -1.9 dBm, which is desirable.

The three input signals--the sampling signal, the memory control signal, and the clear signal--are one-square-pulse signals in every test period. These three signals can be generated from commercial function generators. Although data rates are very low, in order to maintain their timing from the rise and fall edges from the distortion and to prevent potential damage to the instruments by signal reflection through the cable, the proper end for the transmission line must be included. Since the 50 Ω impedance connection is also defined here, inputs to the board should be shunted to the board defined ground plane through a 50 Ω resistor before reaching the chip for the most power delivery and minimized reflection.

The 32-bit output signals of the digital frequency counter are the outputs of the DFFs that are controlled by the memory control signal. Since the memory control signal has only one pulse, these 32 signals have very low data rates and, hence, avoid the RF design issue. In the original system design, they will be sent to a data processor. However, due to time and budget constraints, 8 TIL311A chips of 4-bit hexadecimal display LEDs

display the results and, thus, reduce prototype complexity [45]. Since these LEDs require a 5 V power supply and minimum 2 V input voltage as high level, the design employs 8 4-bit voltage translator chips, TXS0104E, between the biosensor chip outputs and the LED inputs to convert the voltage level from 0 ~ 1.8 V to 0 ~ 5 V [46]. Near each power pin of the LED and voltage translator chips, a 104 (100 nF) bypass capacitor is used for reducing voltage noise.

The remaining two input/output pins on the prototype chip are the power pins, 1.8 V VDD and the ground. The chip ground is connected to the board ground plane, and VDD is provided by the power supply of the PC board. Since the board power supply is responsible for all of the board components including the LEDs, its voltage level has to be 5 V instead of 1.8 V. Therefore, another voltage translator is needed to the prototype chip. In addition, the technology, IBM_CMOS_7RF, requires that power voltage remain stable with less than 10% variation. These two requirements are supplied in the voltage regulator LP3990. Also required for its stable operation are two 1 μF capacitors that are bound to its input and output [47]. For support, a 100 pF bypass capacitor is placed near the prototype chip as well. Meanwhile, this voltage regulator is able to supply 150 mA current, which is sufficient for chip operation. In addition, current drawn by each voltage translator is around 15 μA and 180 mA for each LED--total current needed for the board is about 1.6 A. Therefore, the power supply for this board design is 5V/2A.

After the board design related to all the 36 input/output signals is developed, placement of the prototype chip is considered. Since the goal is to test the chip, a chip socket is used instead of soldering one single chip on the board so that the chip is replaceable. With 800.5 MHz oscillator output signal, the chip socket must have this frequency covered in its bandwidth. SG-MLF-7005 is a suitable QFN chip socket that provides 10 GHz bandwidth for the prototype and test applications [48]. The socket is solder-less since gold wire containing elastomer is used as the connector between the chip and the board, which makes it easy to install and uninstall.

Figure 7-12 shows the schematic of the PC board design. Note that an aluminum box covering the board is an option for stopping noise to the circuits from outside

radiation. Its utilization will depend on the preliminary noise performance of the prototype system. If the aluminum box is required, a window has to be built into the box so that LED results can be recorded. This set up would break radiation isolation. Therefore, an aluminum plate should be soldered onto the board to block the high frequency component--the prototype chip--from the window and the nearby low frequency components.

Based on the proposed board schematic, a matched board layout can be designed with professional softwares EAGLE and GC-Prevue, as shown in Figure 7-13. All components fit into the top side of a double-sided board with a standard size of 100 mm × 80 mm, while the bottom side is comprised of the ground plane and a few traces. Note that the ground plane is connected to the footprint center of the chip socket, which is the thermal pad with drilled holes, and helps to dissipate heat from the biosensor chip. This PC board is built by the board manufacturer Advanced Circuits. Figure 7-14 shows the fabricated board with the chip socket installed and all other components soldered.

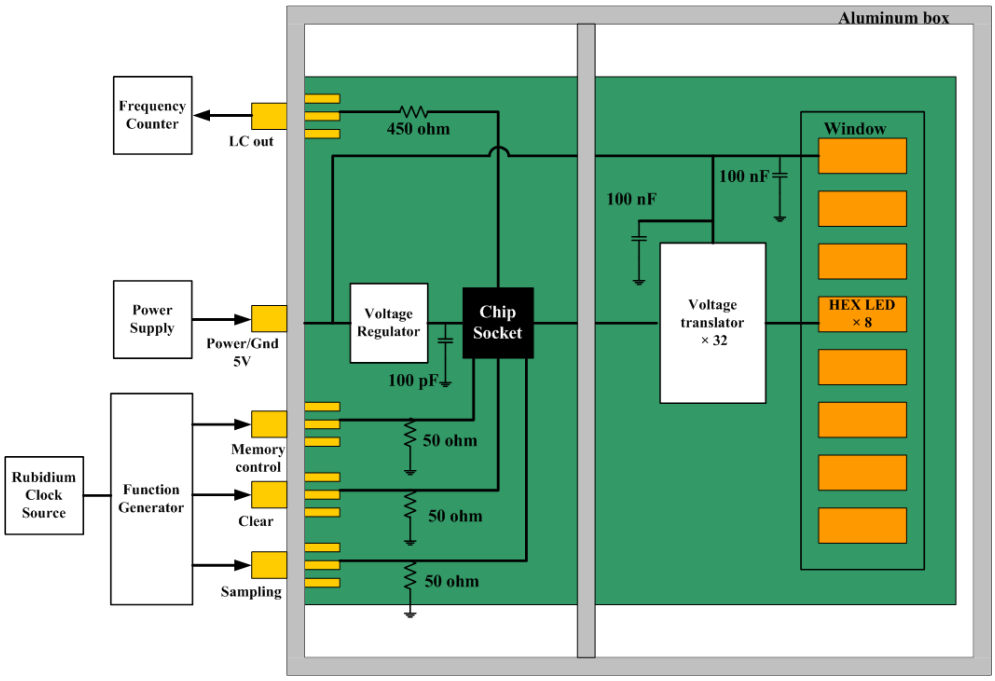


Figure 7-12: The PC board schematic.

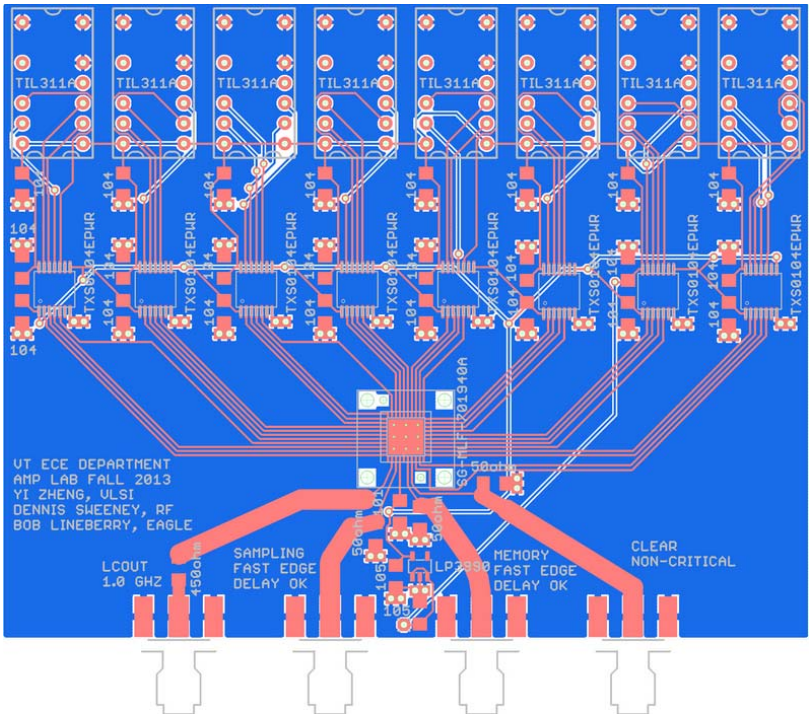


Figure 7-13: The PC board layout.

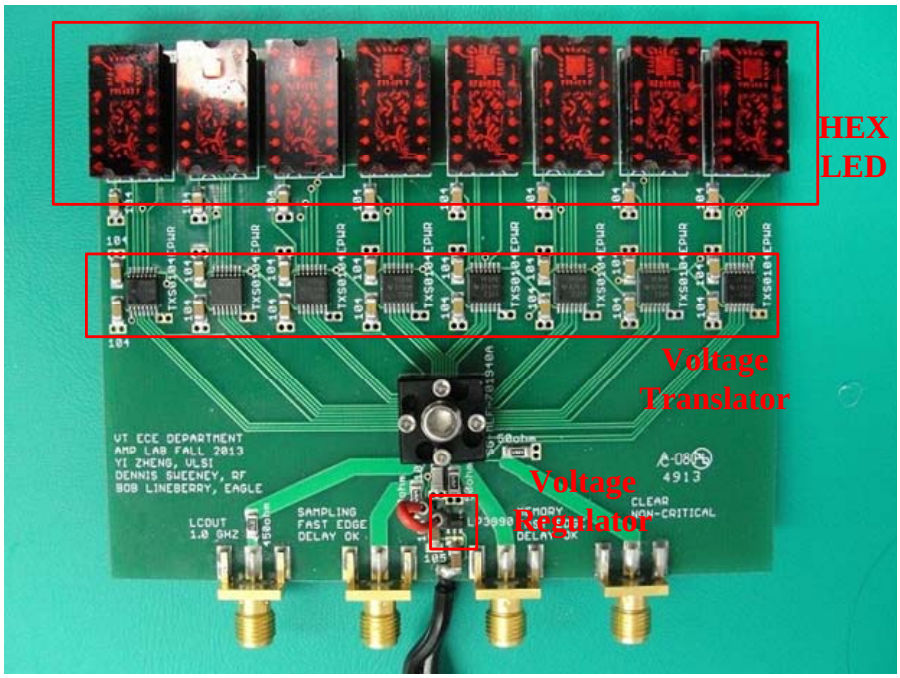


Figure 7-14: The fabricated PC board with all components.

## 7.4 System Test Bench

Once the PC board is complete, the instruments are connected to the four SMA connectors on the board.

As described in Chapter 6, the two signals of “clear” and “memory” do not have critical timing requirements. They are single pulse signals that can be generated by a commercial function generator. Note that, by setting the output impedance to match the 50 Ω characteristic impedance of the cable, the output voltage level of the signals from the function generator should be double that of the chip specification, 0 to 3.6 V.

Similarly, the sampling signal has the same signal format, except the requirement of ultra timing stability. The clock source in general function generators does not reach the stability level of the rubidium time-base. To solve the issue, a rubidium clock generator, LPFRS [49], serves as an external clock source to the function generator. Consequently, the new referenced sampling signal has a variance of < 0.1 PPB. Since the rubidium clock generator dissipates high power to warm up and maintain the temperature in the oven for the stability of the crystal oscillation, the considerable heat also raises the temperature around the device. To avoid damage from overheating, an appropriate heat sink, e.g., a metal plate, must be attached to the device to dissipate the heat to the ambient.

The LC oscillator output is connected to an RF frequency counter or a spectrum analyzer with their 50 Ω input port. Again, the same issue of timing accuracy must be considered. To properly measure the noise/jitter of the oscillation signal, the time base of the instruments has to be more precise than the measured signal. Based on the demand, another rubidium clock source can be used as the reference as well.

The instruments and the constructed board that make up the test bench of the biosensor prototype system are shown in Figure 7-15. The bench supply is used to power up the rubidium clock source, and the oscilloscope with a probe performs as a voltage meter. Since these large instruments are used, the prototype system is not portable. In any future version of the system, the function circuit of the signal generator will be integrated into the biosensor chip. A chip based clock source could be mounted on the PC board.

Note that a chip scale rubidium clock source is quite expensive. Hence, the base line for timing tolerance should be carefully considered when choosing the clock source at a reasonable cost.

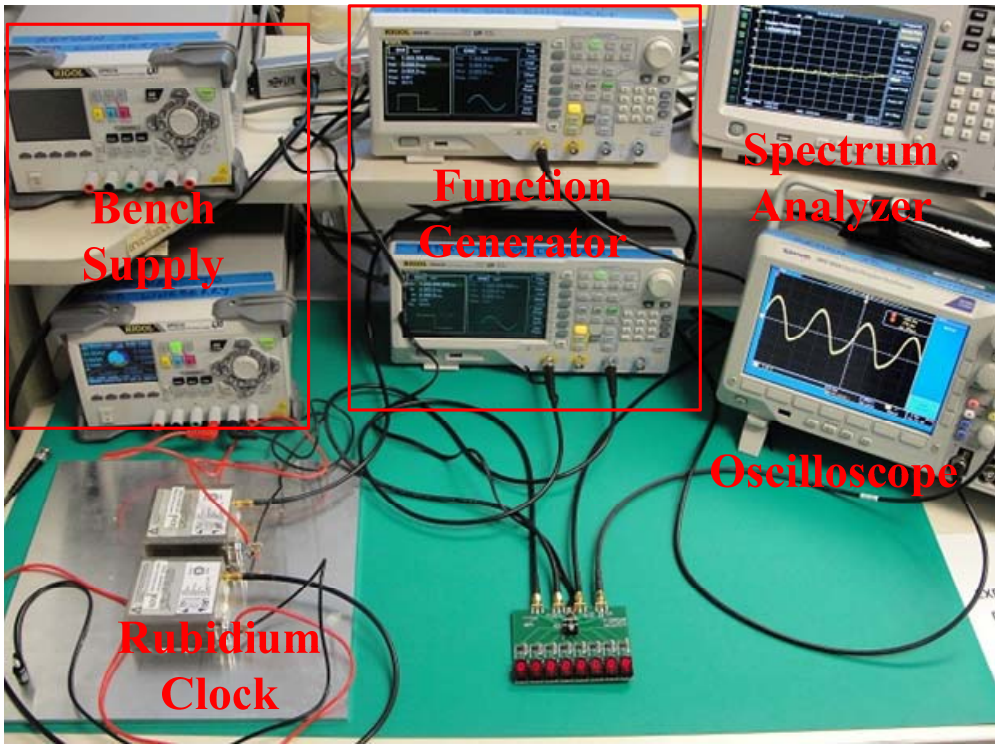


Figure 7-15: The test bench of the prototype system.

## 7.5 System Sensing Accuracy Analysis

All design details of all components in the biosensor system have been discussed. This section lists possible deviations that will affect the system sensing accuracy. Some deviations could be reduced with design improvements in future work.

### 7.5.1. Deviation Analysis

Since the digital frequency counter reports the number of counted cycles of the sampled signal, any timing variation produced by this function block does not change the result.

Thus, total timing error lies in the sampled signal, which is the error accumulation of the oscillation signal from the LC oscillator and the sampling signal from the function generator. Besides the variance of the sampling signal, which is mainly the timing stability of the clock source, quite a few deviation sources in the LC oscillator must be analyzed.

(1) Deviation of the magnetic field uniformity. This deviation is the major source of error and makes the inductor design the main challenge of this project. Simulations in Chapter 4 show that the greatest error is 7%. Figure 3-11 shows that high field deviation area, depicted by red and blue colors, is less than 10% of the sensing plane, which means the error should always be less than the worst case if the biologicals are distributed evenly. Furthermore, same as with the desired frequency shift, the timing deviation or the frequency offset caused by this error is proportional to the quantity of iron nanoparticles.

(2) Deviation from vertical offset of the biologicals. Although the discussion in Chapter 4 indicates that the vertical offset deviation is converged with a large amount of analyte, more varied randomness should be considered. For instance, the thickness of each biological is different, which introduces extra non-uniform vertical offset to the iron nanoparticles inside. This means a larger amount of analyte is required for deviation convergence. Moreover, a special case that a “stand-up” biological is bonded on the antibody could occur. When the biological length of a few microns becomes a vertical offset, the error could be about 14% ~ 20%.

(3) Sample container deviation from the fabrication. The chip surface property measurement reports a vertical offset of the sample container bottom (Section 7.2.3). Obviously, the relative worst error, 23%, is much greater than expected. Also to be considered is that an extra deviation may be due to the non-flat bottom surface.

(4) Period jitter of the oscillation signal. As discussed previously, the long-term jitter tends toward zero (Section 5.5.2). Therefore, the error from this deviation component can be further reduced by either setting a longer period for the sampling signal or calculating the average result from multiple tests. Relative adjustment should be based on the preliminary test results.

(5) Time jitter of the sampling signal. This deviation is determined by the stability of the rubidium clock source, where the maximum is 0.1 PPB. Hence, for the sampling signal with a period of 4 seconds, the greatest timing deviation is 0.4 ns. It is 0.32 cycles of the 800.5 MHz signal and causes 0.08 Hz error in the frequency counting. Note that the minimum counting unit is 1 cycle or 0.25 Hz. If the error from the oscillation signal is less than 0.68 cycles, the total error is below 1 cycle and is not counted.

(6) Deviation from separate test periods. In this prototype, the system baseline is measured first. After the biological process, the same sensor head is measured again to detect change. However, the time between the two measurements could introduce a deviation from the ambient variance, e.g., temperature. Since permittivity varies with temperature, the capacitance in all components of the LC oscillator change with the temperature coefficient, which results in a frequency drift. This coefficient is as great as a few tens of PPM in CMOS technologies and yields a considerable capacitance change, as the following expression states.

$$\Delta C = C \times TCC \times \Delta T \tag{7-1}$$

where $\Delta C$ is the capacitance change based on the original capacitance $C$, $TCC$ is the temperature coefficient, and $\Delta T$ is the temperature shift. This capacitance variance would cause a significant frequency shift and overshadow any sensing results. Therefore, the ambience of the test bench must be carefully managed to minimize $\Delta T$ from different test periods. For example, a thermoelectric temperature controller can be used to maintain the temperature around the PC board. As an alternate solution for any future system version, a second inductor with the identical design could be coupled into the LC oscillator as a reference to remove the temperature coefficient frequency drift from the sensing results.

### 7.5.2. Improvement of the Vertical Offset Deviation

The above analysis indicates that the major issue of vertical offsets from biological placement and chip fabrication could introduce large errors and influence sensing accuracy. If magnetic field uniformity is not limited in a 2D plane, but can be expanded to a 3D volume, these errors would be eliminated by using the inductor design shown in

Figure 7-16. The 4 layers conical-shaped coils are mirrored evenly, with 4 μm as an example. The idea is from the finding that field magnitude variation is approximately linear to the small vertical offset (Figure 4-11). Thus, if the uniformity of the vertical field vector in the center plane is assured by the conical-shaped coils, the superimposed field from the coils and their mirror will maintain uniformity and the field magnitude is doubled because the vertical vectors are the same and the horizontal vectors are canceled by the opposite directions. Then on the planes with the small vertical offsets, the amount of the field increment and decrement of the coils on both sides are about the same due to the linearity, with a minor difference from the unmatched horizontal vectors. Field magnitude in a sensing volume with a 4 μm thickness is then uniform. The greatest field deviation is calculated as 4.6% in the simulation, which results in a 9.5% variance in the inductance change.

Although the vertical offset deviation can be effectively compensated for by the improved mirror structure, there are tradeoffs in the design. First, this structure is composed of more metal layers than the conical-shaped coils. A large volume thickness that will accommodate the deviation requires a technology that supports many metal layers. Hence, the performance of field uniformity will highly depend on the technology specification. Second, the shape of the sample container becomes flask-shaped rather than a straight hole, since the diameter of the top metal coil is shorter than the sensing volume. This flask-shape significantly increases the difficulty and complexity of the fabrication. Future studies should include further analysis of the design optimization and relative tradeoffs.

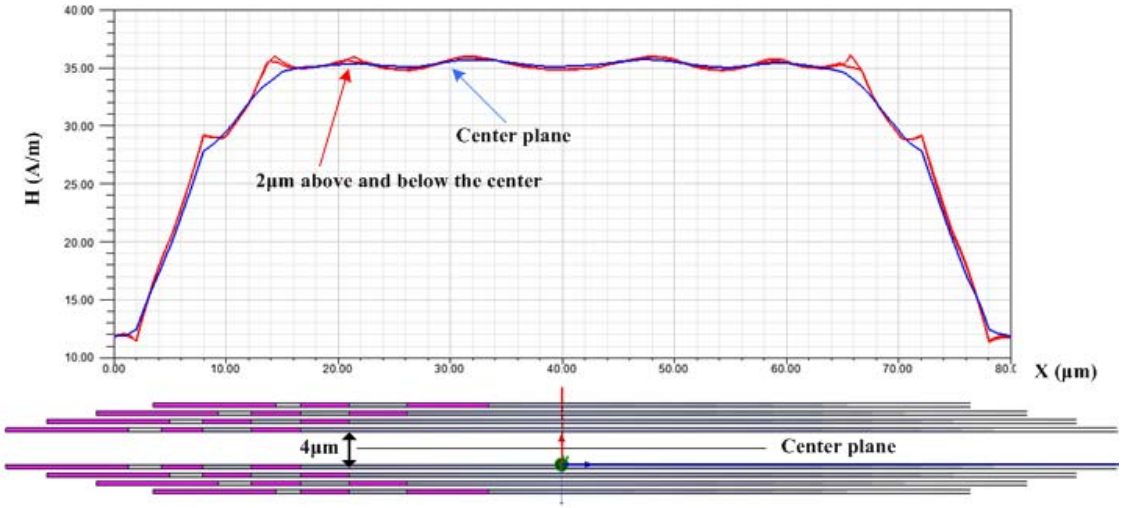


Figure 7-16: The field plot of the mirrored conical-shaped inductor.

## 7.6 Chip Failure in the Prototype Test

The biosensor chip was tested in conjunction with the prototype test bench. The testing results show a failure of the chip operation. Although the functions of the "clear" and "memory" signals work properly, the LC oscillator does not generate an oscillation signal output and, hence, no frequency counting result is reported on the LEDs. The layout based simulation in Cadence shows that the current drawn from VDD in the static state is less than 15 mA. However, the constant DC current measured by the 1.8V power supply of the prototype chip is as great as 280 mA. Meanwhile, with the 32-bit output of the chip, the voltage level for a logic low is 0.35 V above the ground, and, for a logic high, it is 1.25 V, 0.55 V below VDD. This finding indicates that the inverter connected to the output pad fails to increase or decrease the voltage level completely. In other words, the NFET and PFET transistors cannot perform a desired off-state due to the existence of extra current leakage. Consequently, when this static leakage occurs in most of the transistors on the chip, the large cumulative current of 280 mA is generated. After consulting other research and reviewing the layout design, the problem can be identified as the antenna effect that damages the gate oxide in the manufacturing process and produces conduction paths from the transistor gate to the terminals of source, drain, and

channel. Moreover, in the transistors of the LC oscillator circuit, the conduction paths act as extra feedbacks in addition to the LC tank and, hence, reduce the $Q$ factor and the open loop gain, which would kill the oscillation. Details and a solution to the antenna effect are introduced below.

### 7.6.1 Antenna Effect

The antenna effect, not actually related to the common antenna device, is an effect that can potentially cause yield and reliability problems during the production of the CMOS circuits on the chips [50][51]. In the semiconductor manufacturing process, plasma etching is used for the construction of most layers. Each time etching is applied, some free charges are added and left on the wafer. These charges are then collected by nearby metals, which is similar to an antenna. Figure 7-17 shows that IC circuits based on CMOS transistors, the gate of a transistor is always connected to the diffusion region of another transistor. The connection passes through one or multiple metal layers. In this structure, the collected charges on the metals can dissipate through the diffusion region into the substrate, since the diffusion region and the substrate form a PN junction reverse-biased diode. When the potential difference across the diode, caused by too many collected charges, exceeds the breakdown threshold, the diode opens and dissipates the charges. However, the connection of the gate and the diffusion region in this structure is not formed until the production of the 3rd metal layer. A depiction of the structure prior to the 3rd metal layer being laid down is shown in Figure 7-18. In this case, on the left, no dissipation path exists for the collected charges in the 1st and 2nd metals. Hence, the floating gate and substrate are isolated by the gate oxide act as a capacitor. The accumulated charges increase the voltage potential of the gate. Once the threshold is exceeded, the sudden high current flowing through could breakdown the gate oxide. This damage results in the gate oxide being breached during production and generates the current leakage path through the oxide. The antenna effect can be effectively avoided by the reverse-biased diode provided by the diffusion region, since its breakdown threshold voltage is generally smaller than that of the gate oxide. In old CMOS technologies using

a thick gate oxide, the antenna effect was not a critical issue. However, in present technologies, the antenna effect produced by the manufacturing becomes unavoidable and has to be considered in the design.

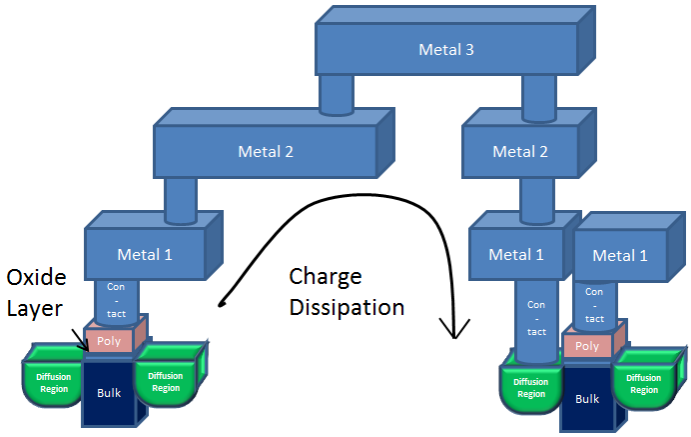


Figure 7-17: The charge dissipation path from gate to the diffusion region [52] "Gate Oxide Defects Caused by Antenna Effects", *http://siliconyield.com/gate-oxide-defects-caused-by-antenna-effects/*, used under fair use, 2014.

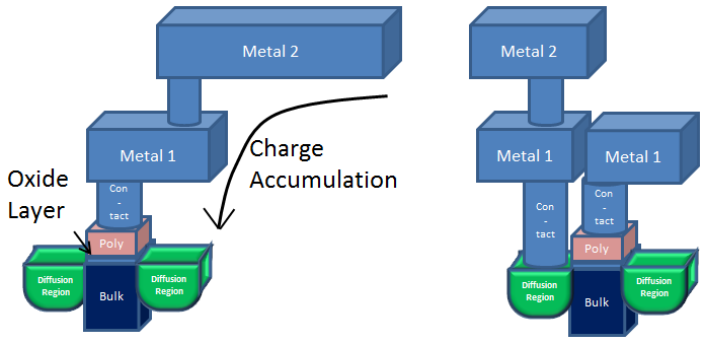


Figure 7-18: The charge accumulation without the dissipation path [52] "Gate Oxide Defects Caused by Antenna Effects", *http://siliconyield.com/gate-oxide-defects-caused-by-antenna-effects/*, used under fair use, 2014.

### 7.6.2 Solutions to the Antenna Effect

To reduce the antenna effect and protect the gate oxide in the manufacturing process, the first solution is to limit the area of the metals connected to the gate. The area of the conductor exposed to the plasma determines the capability of the charge collection. This phenomenon is defined as “antenna ratio” which is the area ratio of the conductor. Hence, using a given antenna ratio from the design rule, the largest area of the metals prior to the metal layer for the final connection is predictable (Figure 7-19). If a long prior metal wire is inevitable, a jumper can be inserted into the path to reduce the gate conduction area.

The second solution uses the same principle. Vias is used to connect the gate to the highest metal layer (Figure 7-20). Hence, the total gate conduction area prior to the highest metal layer is minimal, and no violation of the antenna rule is guaranteed. The above two solutions are based on routing topology. They will significantly increase the complexity and difficulty of placing and routing (P&R), especially for a large size circuit.

The third solution, the most commonly applied solution, is to insert a connection to a diffusion region at the first metal layer very close to the gate (Figure 7-21). This set up provides protection to the gate because of the formed reverse-biased diode. It is easy to design and does not affect the original routing topology. Note that, although the added diode introduces extra loading capacitance which makes the circuit slower and more power hungry, the capacitance of the minimum size diode is relatively small compared to other loading capacitances. It will reduce the highest possible frequency. In this project, with a frequency below 1 GHz, the solution of adding a diode is the most effective way to eliminate the fabrication yield of the antenna effect.

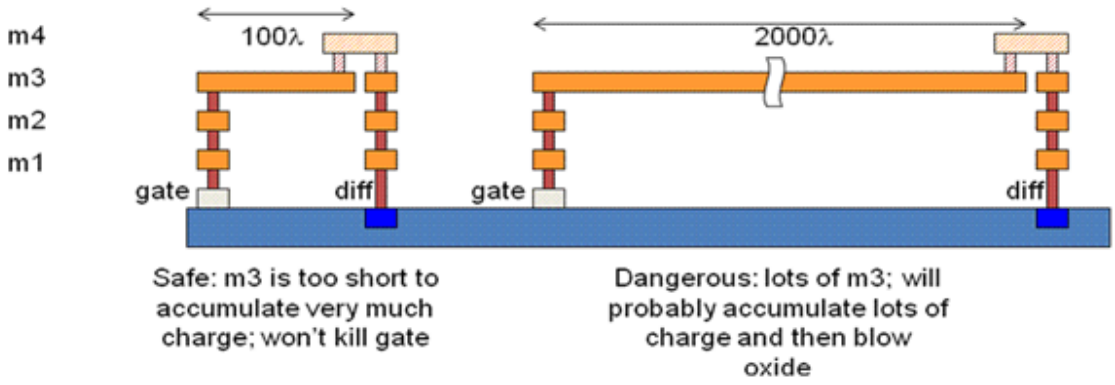


Figure 7-19: Limiting the gate conduction area prior to the final conduction layer [53] "Antenna Effects", *http://www.vlsi-expert.com/2008/07/antenna-effects.html*, used under fair use, 2014.

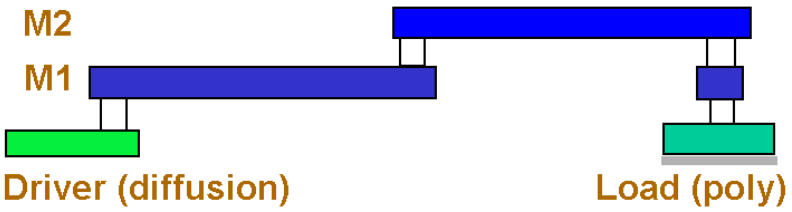


Figure 7-20: Minimizing the conduction area by connecting the gate to the top layer [54] "Antenna effect", *http://en.wikipedia.org/wiki/Antenna_effect*, used under fair use, 2014.

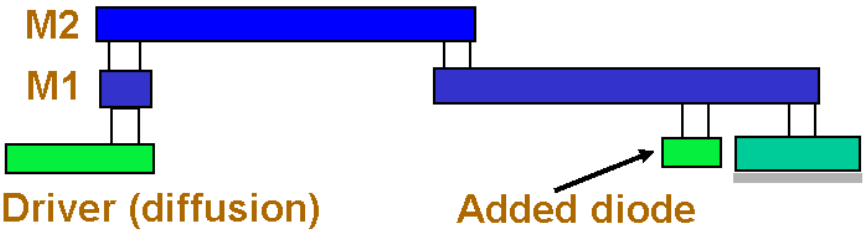


Figure 7-21: Adding a reverse-biased diode beside the gate [54] "Antenna effect", *http://en.wikipedia.org/wiki/Antenna_effect*, used under fair use, 2014.

## 7.7 Summary

In this chapter, details related to chip fabrication, PC board design, and instruments used to constitute the system test bench are introduced. Possible deviations that may affect the system's sensing accuracy are discussed, and related improvements are proposed. The research and analysis of the flawed chip guide the future work relating to adjustments in the layout designs that will eliminate potential issues from the antenna effect.

# Chapter 8: Conclusion

## 8.1 Summary

In this dissertation, an innovative CMOS magnetic biological sensor system for rapid detection for the presence of potential pathogens and bioterrorism agents, both in specimens as well as in environment, is proposed. Previous biosensor work and the motivation for this research are presented. The sensing mechanism is discussed and the system overview is given in Chapter 2. Chapter 3 introduced a novel conical-shaped inductor design as the sensor head to achieve magnetic field uniformity. Then in Chapter 4, magnetic simulations proved the sensing concept that the biological amount is linear and could be detected by magnetic/electrical change, with a maximum 7% deviation. Consequently, the design details of the LC oscillator are presented in Chapter 5. Inductance change from the presence of biological agents is transformed to a frequency shift of the oscillation signal. To capture the frequency shift as the detection output, the signal processing design includes an asynchronous digital frequency counter and a related timing controller, as described in Chapter 6. Integration of all the designs produces a chip layout based on IBM_CMOS_7RF 180 nm technology. To test the fabricated biosensor chip, a prototype test bench is constructed, and Chapter 7 introduces the process details, including the PC board design and related instruments.

## 8.2 Conclusions

Compared to conventional biological sensors, the advantages of the proposed BASIC system, which is small-sized, portable, and has high sensing accuracy, should have wide application, not just for hospital and laboratory-based biomedical instruments, but also for outdoor devices used for point-of-care diagnosis and for national defense. Meanwhile, the highly integrated circuit system on the chip reduces the manufacturing cost and facilitates integration into a multi-functional system.

The system operating frequency is set at around 800.5 MHz; this value is chosen from several considerations and simulations. At this frequency, the greatest deviation of the oscillation frequency shift is only 7% in magnetic simulations by assuming the circuit is noiseless. Consequently, the LC oscillator design applies cross-coupled topology to generate the oscillation signal for reflecting the sensed frequency shift. Then, the digital frequency counter, made up of a 32-bit asynchronous counter reports the sensing results from the sampled signal with a 4-second sampling period. Therefore, the sensing resolution is 0.25 Hz in the 800.5 MHz.

Since the circuit is never noiseless (discussed in Section 7.5), several issues cause deviations to the sensing results, such as non-uniformity due to biological properties, vertical offset from the chip fabrication, time jitters in the oscillation signal and the sampling signal, and the frequency drift due to temperature variance. These possible deviations could affect the system sensing accuracy and decrease system performance. Some of these factors can be reduced by managing test settings, while the solutions to other issues must be handled in the design of future versions of the system.

In preliminary testing, the manufactured chips are discovered to be damaged and show defects upon use. Extra current leakage in the transistors produced large power consumption, degraded the voltage swing range, and killed the oscillation in the LC oscillator. This failure is caused by no antenna effect protection of the gate oxide of the transistors. This problem should be preferentially fixed in the layout design.

## 8.3 Future Work

The major focus of future work should be on adding antenna effect protection to the transistors in the layout. This adjustment will be accomplished by plugging in a reverse-biased PN diode from the trace on the first metal layer connected to the transistor gate to a small-sized diffusion region. With this so called "tiedown" protection, the accumulated charges introduced by the manufacturing process can be dissipated before they breakdown the gate oxide.

Second, ambient temperature management is an option used to reduce the influence of the frequency drift. For example, a thermoelectric temperature controller can be used to maintain the temperature around the device. However, it increases overall size and cost of the system. Thus, the recommendation (mentioned in Section 7.5) is to integrate another identical inductor as the reference. This inductor should not be accessed by any biological process so that it properly reflects the deviations by temperature and electrical factors.

Third, the fluctuation of VDD integrates noise from all transistors on the chip. Although noise power is restricted by the bypass capacitor and the voltage regulator on the PC board, it still contributes to phase noise, or period jitter, of the oscillation signal. To further reduce this power supply noise, the cross-coupled structure of the LC oscillator could be re-designed by inserting a transistor controlled tail current source. However, as a tradeoff, the circuit block to generate control voltage increases design complexity and introduces new noise through the tail transistor. In addition, it also reduces voltage headroom for oscillation. Such tradeoffs should be carefully researched in the future.

Fourth, the system timing controller is not integrated in the chip design. Hence, large size instruments like function generators limit the mobility of the test bench. Future versions of this system should integrate this function block and apply an on-chip clock source on the PC board to avoid using extra instruments.

Fifth, due to the limited design budget, the BASIC system is based on IBM 180 nm technology, which is relatively old and contains many restrictions in the free version.

System performance is hence slightly below that expected, and further improvement is also restricted. For instance, with more metal layers supported by a newer technology, current distribution in the inductor coils could be better arranged to achieve a more uniform magnetic field, which means higher sensing accuracy. Therefore, in the future, working with newer technologies will enhance success. Moreover, the small size TinyChip limits the circuit design area. Future design in a larger chip would allow a sensor array that could detect multiple biological species and could integrate other function blocks.

Sixth, when the new version of the biosensor chip is designed and manufactured, adjustment for the PC board design would be the next step. Once both the upgraded chip and PC board are ready, the new test bench could be developed for electrical tests. After proper system performance is confirmed, biological tests could begin to enhance further physical research and improvements.

# References

[1] Turner, Anthony. “Biosensors: fundamentals and applications.” (1987).

[2] Newman, Jeffrey D., and Anthony PF Turner. “Home blood glucose biosensors: a commercial perspective.” *Biosensors and Bioelectronics* 20.12 (2005): 2435-2453.

[3] Wang, Joseph. “Glucose biosensors: 40 years of advances and challenges.” *Electroanalysis* 13.12 (2001): 983.

[4] S.M. Azimi, M.R. Bahmanyar, M. Zolgharni, W. Balachandran, “An Inductance-based Sensor for DNA Hybridization Detection”, *Nano/Micro Engineered and Molecular Systems*, Jan. 2007, pp. 524-527.

[5] Berggren, Christine, et al. “A feasibility study of a capacitive biosensor for direct detection of DNA hybridization.” *Electroanalysis* 11.3 (1999): 156-160.

[6] N.C. Cady, S. Stelick, M.V. Kunnavakkam, Y. Liu, C.A. Batt, “A microchip-based DNA purification and real-time PCR biosensor for bacterial detection”, *IEEE Sensors*, Vol. 3, Oct. 2004, pp. 1191-1194.

[7] Pearce, Timothy C., et al. “Electronic nose for monitoring the flavour of beers.” *Analyst* 118.4 (1993): 371-377.

[8] Röck, Frank, Nicolae Barsan, and Udo Weimar. “Electronic nose: current status and future trends.” *Chemical Reviews* 108.2 (2008): 705-725.

[9] Homola, Jiří, Sinclair S. Yee, and Günter Gauglitz. “Surface plasmon resonance sensors: review.” *Sensors and Actuators B: Chemical* 54.1 (1999): 3-15.

[10] Liedberg, Bo, Claes Nylander, and Ingemar Lunström. “Surface plasmon resonance for gas detection and biosensing.” *Sensors and actuators* 4 (1983): 299-304.

[11] Taylor, Allen D., et al. “Surface plasmon resonance (SPR) sensors for the detection of bacterial pathogens.” *Principles of Bacterial Detection: Biosensors, Recognition Receptors and Microsystems*. Springer New York, 2008. 83-108.

[12] Chu, Hsiaoyun, Yaowen Huang, and Yiping Zhao. “Silver nanorod arrays as a surface-enhanced Raman scattering substrate for foodborne pathogenic bacteria detection.” *Applied spectroscopy* 62.8 (2008): 922-931.

[13] Sundaram, Jaya, et al. “Surface enhanced Raman scattering (SERS) with biopolymer encapsulated silver nanosubstrates for rapid detection of foodborne pathogens.” *International journal of food microbiology* 167.1 (2013): 67-73.

[14] Joshi, Deepti, et al. “Detection of biological warfare agents using ultra violet-laser induced fluorescence LIDAR.” *Spectrochimica Acta Part A: Molecular and Biomolecular Spectroscopy* 112 (2013): 446-456.

[15] Wang, Jinghui, et al. “Rapid detection of pathogenic bacteria and screening of phage-derived peptides using microcantilevers.” *Analytical chemistry* (2014).

[16] Weeks, B. L., et al. “A microcantilever‐based pathogen detector.” *Scanning*25.6 (2003): 297-299.

[17] Lee, Junhee, et al. “CMOS image sensor-based ELISA detector using lens-free shadow imaging platform.” *Sensors and Actuators B: Chemical* 196 (2014): 511-517.

[18] LUI WAI YI, L. E. N. A. “Magnetic particle biosensors.” (2009).

[19] H. Wang, C. Sideris, A. Hajimiri, “A frequency-shift based CMOS magnetic biosensor with spatially uniform sensor transducer gain”, *IEEE Custom Integrated Circuits Conference*, Sept. 2010, pp. 1-4.

[20] F. Widdershoven, D. Van Steenwinckel, J. Überfeld, T. Merelle, H. Suy, F. Jedema, “CMOS biosensor platform”, *IEEE International Electron Devices Meeting (IEDM)*, 2010, Dec. 2010, pp. 36.1.1 - 36.1.4.

[21] O. Tigli, L. Bivona, P. Berg, M.E. Zaghloul, “Fabrication and Characterization of a Surface-Acoustic-Wave Biosensor in CMOS Technology for Cancer Biomarker Detection”, *IEEE Biomedical Circuits and Systems*, Feb. 2010, pp. 62 - 73.

[22] Fujimoto, Jun. “Home medical system and medical apparatus for use therewith.” U.S. Patent No. 5,339,821. 23 Aug. 1994.

[23] Zheng, Yi, and Joseph G. Tront. “Biological agent sensing integrated circuit (BASIC): A new CMOS magnetic biosensor system.” *Sensors, 2012 IEEE*. IEEE, 2012.

[24] M. Fan, H. Shao, J. Wang, “Some experiences of using integral equation method to calculate magnetostatic fields”, *IEEE Transactions on Magnetics*, Vol. 21, No. 6, Nov 1985, pp. 2185-2187.

[25] Messenger, Ann JM, and Raymond Barclay. “Bacteria, iron and pathogenicity.” *Biochemical Education* 11.2 (1983): 54-63.

[26] Neilands, J. B., ed. “*Microbial iron metabolism: a comprehensive treatise*.” New Delhi: Academic Press, 1974.

[27] Janeway, Charles A., et al. “Immunobiology.” (2001).

[28] Litman, Gary W., et al. “Phylogenetic diversification of immunoglobulin genes and the antibody repertoire.” *Molecular biology and evolution* 10.1 (1993): 60-72.

[29] “Antibody”, *http://en.wikipedia.org/wiki/Antibody*.

[30] Kumagai, I. and Tsumoto, K. 2010. “Antigen–Antibody Binding.” eLS.

[31] Wild, David, ed. “The immunoassay handbook”, *Gulf Professional Publishing*, 2005.

[32] J. C. Maxwell, “A Treatise on Electricity and Magnetism”, Clarendon, Oxford, 1873, Vol.I, Secs. 713, 714, and 715.

[33] “H.A. Wheeler, “The Spherical Coil as an Inductor, Shield, or Antenna”, Proceedings of the IRE, Vol. 46, No. 9, 1958, pp. 1595-1602.

[34] Zheng, Yi, and Joseph G. Tront. “Improved biological agent sensing integrated circuit (BASIC).” *Sensors Applications Symposium (SAS), 2013 IEEE*. IEEE, 2013.

[35] “CMOS7RF (CMRF7SF) Design Manual”, *IBM Microelectronics Division*.

[36] “User’s Guide - Maxwell 3D”, *Software Version 12.1, Ansoft Inc*, 2009.

[37] Dauphinee, Leonard, Miles Copeland, and Peter Schvan. “A balanced 1.5 GHz voltage controlled oscillator with an integrated LC resonator.” *Solid-State Circuits Conference, 1997. Digest of Technical Papers. 43rd ISSCC., 1997 IEEE International*. IEEE, 1997.

[38] “Craninckx, Jan, and Michiel SJ Steyaert."A 1.8-GHz low-phase-noise CMOS VCO using optimized hollow spiral inductors.” *Solid-State Circuits, IEEE Journal of* 32.5 (1997): 736-744.

[39] Ahrens, Tamara I., Ali Hajimiri, and Thomas H. Lee. “A 1.6 GHz 0.5 mW CMOS LC low phase noise VCO using bond wire inductance.” *1st Int. Workshop Design of Mixed-Mode Integrated Circuits and Applications*. 1997.

[40] “Sonnet User’s Guide”, *Software Version 12, Sonnet Software Inc*, 2009.

[41] Behzad, Razavi. “Design of analog CMOS integrated circuits.” *International Edition* (2001).

[42] Test Results for IBM 0.18 nanometer runs, *https://www.mosis.com/cgi-bin/cgiwrap/umosis/swp/params/ibm-018/v08f_7hv_6lm_am-params.txt, MOSIS Inc*.

[43] “Clock (CLK) Jitter and Phase Noise Conversion”, Application Note 3359, *Maxim Integrated*.

[44] MOSIS Educational Program (MEP), *http://mosis.com/you-are/academic-institutions, MOSIS Inc*.

[45] "TIL311A datasheet", *Texas Instruments*.

[46] "TXS0104E datasheet", *Texas Instruments*.

[47] "LP3990 datasheet", *Texas Instruments*.

[48] "GHz QFN Socket User Manual", *Ironwood Electronics*.

[49] "Low Cost LPFRS Spec", *SpectraTime*.

[50] Shin, Hyungcheol, Cl C. King, and Chenming Hu. "Thin oxide damage by plasma etching and ashing processes." *Proc. IEEE Int. Rel. Phys. Symp*. 1992.

[51] Fang, Sychyi, and James P. McVittie. "Thin-oxide damage from gate charging during plasma processing." *Electron Device Letters, IEEE* 13.5 (1992): 288-290.

[52] "Gate Oxide Defects Caused by Antenna Effects", *http://siliconyield.com/gate-oxide-defects-caused-by-antenna-effects/*.

[53] "Antenna Effects", *http://www.vlsi-expert.com/2008/07/antenna-effects.html*.

[54] "Antenna effect", *http://en.wikipedia.org/wiki/Antenna_effect*.